Chapter-3

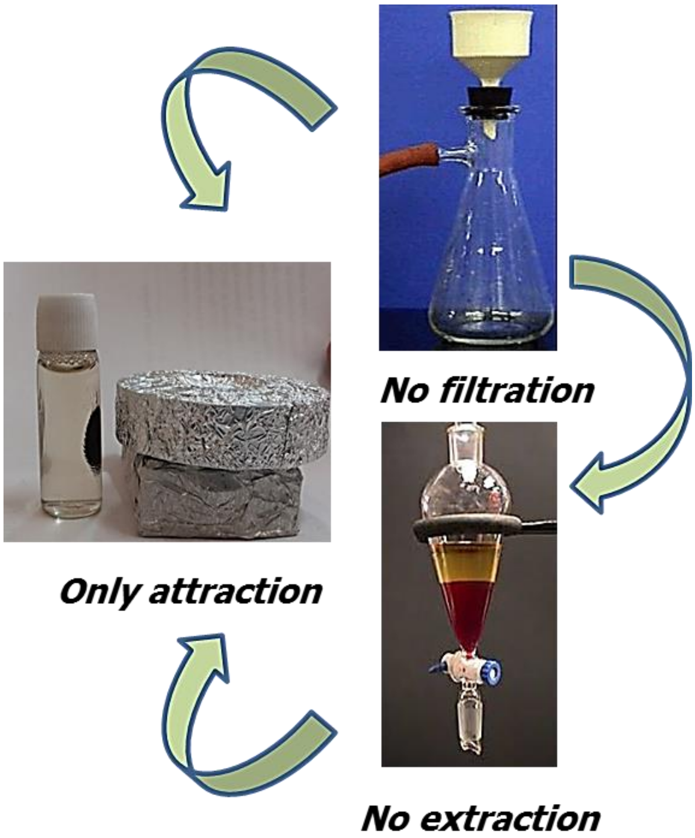

Magnetically separable core/shell Iron oxide@Nickel nanoparticles: Synthesis, characterisation and catalytic application

3.1.1 Introduction

The concept of ''Green Chemistry'' has come out as one of the guiding principles of environmentally benign synthesis.[1–3] Nanomaterials catalyzed transformations in an aqueous reaction medium are one of the ideal solutions for the development of green and sustainable protocols. Nanocatalysis is a rapidly growing field which involves the use of metal nanoparticles as catalysts for a variety of organic reactions.[4] The preparation and use of magnetic nanoparticles (MNPs) offers advantages in clean and sustainable chemistry as they are non-toxic, readily accessible, and retrievable.[5] Additionally, the activity and selectivity of magnetic nano-catalysts can be manipulated by their surface modification.

The development and design of core-shell nanomaterials has emerged in recent years because of their multifaceted applications especially as catalysts for organic reactions.[6,7] Magnetically separable nanocatalyst is an important class of the core-shell nanocatalyst family which are robust, air stable, avoid traditional filtration processes and are recyclable.[8] Various methods have been developed to synthesize specific application based MNPs.[9–13] Some of them are aimed at developing materials from waste such as iron tailings. Tailings refer to waste material of beneficiation processes. Among several iron based solid waste, iron ore tailings (IOTs) is one of the fast accumulating wastes throughout the world due to rapid expansion of iron and steel based industries and is becoming one of the serious environmental threats for the future generation. Presently IOTs are mainly used with very little intervention of high technology and moreover value addition is low. As a result there is an increasing interest in search of possible alternative uses of waste IOTs such as adsorption and catalysis or as precursors to value added products before their final discharge.[14-19] Here we assess the potential of synthesizing magnetic iron oxide from IOTs and use as template for synthesis of magnetically separable nickel nanoparticle (NiNPs).

The reduction of nitroarenes is an important process as the products, aromatic amines, are versatile intermediates and precursors in the preparation of dyes, pharmaceuticals, pigments, agrochemicals and polymers.[20] The process is complicated as the reduction of a nitro group proceeds in stages and it often stops at an intermediate stage producing hydroxylamine and hydrazine as side products.[21] A variety of procedures and reducing agents are available for this purpose.[22] In literature a few procedures involving noble metal NPs such as Pd, Pt, Ag, Au, as well as Fe, Fe_3O_4@Ni and Ni@Ag NPs have been demonstrated for the reduction of nitro group.[22-24,7] The main limitations of earlier reported work were the necessity of high H_2 pressures, prolong reaction time, lower turnover number, organic solvents, less recyclability and high temperatures. Further, the selection of metal and its support, the hydrogen source and operational simplicity, which are the important parameters for effective conversions, are restricted. However, an alternative efficient, simple, chemoselective, green and cost-effective procedure is highly appreciated.

In the earlier chapters, we have investigated the use of NiNPs as catalysts for transesterification as well as reduction.[25] In this chapter, we report the first protocol for the synthesis of starch capped iron oxide@Ni (IO@Ni) core-shell magnetically separable nanocatalyst for hydrogenation of aromatic nitro compounds. Initially *p*-nitroaniline (PNA) was used as the model system to simplify the analysis and to accelerate the screening speed. All reactions were carried out at room temperature (rt) in aqueous medium (Green solvent). Consequently the optimized conditions were used for the synthesis of various aromatic amines.

3.1.2 Experimental

3.1.2.1 Materials

p-nitroaniline (PNA), other aromatic nitro compounds, $NaBH_4$, $Ni(CH_3COO)_2.4H_2O$, liquid ammonia, and starch were purchased from Merck Mumbai, India. All the solutions were prepared using double-distilled and demineralized water. Iron ore tailings, collected from iron industries (Silverline Exporters Private Limited, Gujarat, India), and were screened for their iron contents and one sample with relatively high iron content (~36.04%) was used as one of the starting materials.

3.1.2.2 Synthesis of Iron oxide

Mixture of iron oxide was synthesized from the waste iron ore tailings (IOTs) via acid leaching and precipitation through a sequential precipitation method, as previously reported.[26] For almost complete recovery of iron from IOTs it was first neutralization by adding $Ca(OH)_2$ followed by the settling of aluminium hydroxide and calcium sulfate; subsequently neutralization by adding NaOH and precipitation of $Fe(OH)_2$. The $Fe(OH)_2$ was gradually oxidized to iron oxide. The thermal treatment of iron oxide was performed in an oven, after drying at 100 °C, at 450 °C temperature. Further details on the synthesis of iron oxide is discussed elsewhere.[26-28] These results indicate that IOTs could be used as a source material for the production of iron oxide, with comparable quality to those produced using analytical-grade reagents.

3.1.2.3 Synthesis of Iron oxide@Nickel Nanoparticles (IO@NiNPs)

IO@Ni core@shell NPs were synthesized by reduction of Ni^+ ions in the presence of iron oxide (**Scheme 3.1**). To deposit NiNPs, 100 mg of iron oxide was dispersed in 10mL of deionized water and sonicated for 30 min. Nickel Nanoparticles were synthesized on magnetic core through a wet chemical reduction process by earlier reported method with minor modifications.[25b] $Ni(CH_3COO)_2.4H_2O$ and soluble starch were used as metal salt precursor and stabilizing agent respectively. $NaBH_4$ (10%, W/V) was used as reducing agent and liquid ammonia as complexing agent. Briefly 10 ml of 0.02M nickel acetate solution was added to 10 ml of starch solution (1%, W/V) and stirred on a magnetic stirrer at RT. The pH of the solution was adjusted to 10 with liquid ammonia (600μL) and reduction was carried out with 200 μL of $NaBH_4$ solution. On further stirring for 10 min. the IO were gradually coated by NiNPs when the colour of the solution changed from red to reddish black. The resultant IO@NiNPs were collected by external magnet and washed by deionized water several times to remove unreacted materials. Finally NPs were washed with acetone, and dried at 60 °C under a vacuum.

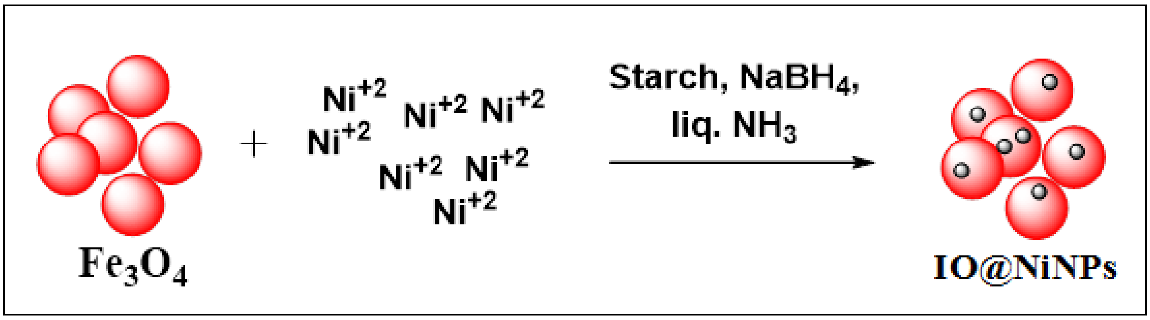

Scheme 3.1 Synthesis of Iron oxide@Ni core@shell NPs (~2% % loading of NiNPs)

3.1.2.4 Catalytic reduction of *p*-Nitroaniline and other aromatic nitro compounds

In a typical reaction PNA 50mg (0.362 mmol) was used as a starting material, $NaBH_4$ 54.6mg (1.44 mmol) as a source of hydrogen, water (2 mL) as a solvent and IO@Ni-MNPs 12mg (0.45 wt% NiNPs of PNA) as a nanocatalyst. All the components were mixed together in 10 mL round bottom flask and the reaction was carried out at room temperature (rt, 25-30 °C) under stirring for 12 min. Reaction monitoring was done by thin-layer chromatography (TLC) and gas chromatography. After completion of the reaction, catalyst was separated magnetically. The product was isolated by extraction in dichloromethane and evaporation of solvent followed by column chromatography (10:90, ethyl acetate in hexane v/v) over basic alumina furnished *p*-Phenylenediamine (PPDA). The spectroscopic data of this compound are in good agreement with those reported. The reaction was also carried out with IO, NiNPs and without catalyst for comparison.

Reduction of other nitro aromatics was carried out in a similar manner. The products purified by short-path basic alumina chromatography (0-40% ethyl acetate in hexane v/v) were analyzed by ^{1}HNMR (Supporting information).

All experiments have been repeated three times and the reproducibility confirmed. The recyclability of the NPs was also surveyed. The NPs were recovered by magnet and washed with water followed by methanol and again water. They were dried at 60 ºC under vacuum and used for the next cycle.

3.1.2.5 Characterizations methods

The chemical analyses for major constituents in IOT, acid insoluble residue and aqueous suspension of IO@NiNPs were carried out by conventional wet chemical analysis while AAS (AA 6300: Shimadzu, Japan) or ICP-OES (Perkin Elmer, 4300) was used to analyze the constituents present in traces. The powered X-ray diffraction (XRD) patterns were recorded with a PanAlytical (model; Empyrean) ‘X’PERT-PRO XRPD of Cu Kα radiation (λ= 0.15406 nm) on advance X-ray power diffractometer. Samples were prepared by pressing dried powder and patterns were collected with scanning rate of 2°/min and 2θ ranging from 0 to 80°. Surface area and porosity of the nanocatalyst were measured by a volumetric adsorption system (Micromeritics Instrument corporation, USA, model ASAP 2010) using N_2 adsorption/desorption isotherms at 77 K upto 1 bar. Prior to the measurements, the samples were activated (degassed) by heating at the rate of 1 K/min upto 383 K under vaccum. The temperature as well as vacuum was maintained for 7 hours prior to the measurements. Surface area was calculated by Brunauer-Emmet-Teller (BET) method while the porosity by Barrett-Joyner-Halenda (BJH) method. High-Resolution Transmission Electron Microscopy (HR-TEM) was carried out using Jeol (Jem-2100) electron microscope operated at an acceleration voltage of 200 kV. For this purpose, dry powered sample was dispersed in methanol and ultrasonication treatment was given for 30 min. After that sample was deposited onto a carbon-coated grid at room temperature and it was allowed for air-drying (about 6 hours). Selected area electron diffraction patterns (SAED) and Energy-dispersive X-ray spectroscopy (EDX/EDS) were also investigated from the electron micrographs. FT-IR spectra were recorded as KBr pellet on Perkin Elmer RX1 model in the range of 4000-400 cm^{-1}. Magnetic measurements were done by a vibrating sample magnetometer (EG&G Model 155 VSM) at room temperature in the range +20,000 to −20,000 G. The surface composition was investigated using X-ray Photoelectron Spectroscopy (XPS) on VSW X-ray photoelectron spectrometer (UK) using Mg and Al twin anode X-ray gun with multichannel detector and hemispherical analyser having resolution of 1.0 eV. The binding energies obtained in the XPS analysis were calibrated against the C1s peak at 284.6 eV.

IO@NiNPs catalyzed hydrogenation reaction was monitored on PerkinElmer Lambda 35 UV–vis spectrophotometer by corresponding $\lambda_{\text{-max}}$. Hydrogenation reaction monitoring was also done by thin-layer chromatography (TLC, Using ninhydrin as staining reagent) and gas chromatography (GC). All products of the reduction of nitroarenes are commercially available and were identified by comparing their physical and spectral data (m.p., TLC (silica gel 60 F254, Merck, Mumbai, India), GC (Perkin Elmer clarus 500 GC) and ^{1}H NMR (BRUKER 400 MHz) with those of authentic samples or reported data.

3.1.3 Results and Discussions

3.1.3.1 Synthesis and characterizations of Iron oxide (IO)

The IOTs, selected for the present study, primarily constitute of Fe, Si and Al (Fe_2O_3, 53.68; SiO_2, 17.58; Al_2O_3, 14.46; P_2O_5, 1.61; CaO, 1.44, MgO, 0.13; LOI, 10.01 wt %) with magnetite, hematite and goethite as the main iron bearing phases. XRD pattern shows that Maghemite, Magnetite (θ=44.97) and kaolinite (θ=21.18) are present in the IOTs. Si and Al are present in the form of kaolinite which is evident from X-ray diffraction (XRD) patterns (**Figure 3.1**).

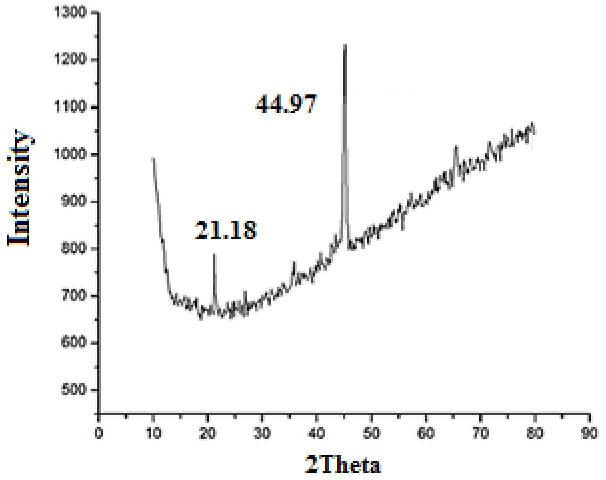

Figure 3.1 XRD pattern of IOTs

Figure 3.2A shows XRD of as synthesized IO. The lines in the **Figure 3.2A** correspond to crystalline phases. It is from the pattern that sample is composed of mixed phases. The detail analysis has been carried out based on Crystallography Open Database (COD). All the crystallite lines identified with respective phase(s) are shown in the **Figure-3.2**. Details of compositions along with its peak positions are shown in **Table 3.1 to 3.4.**

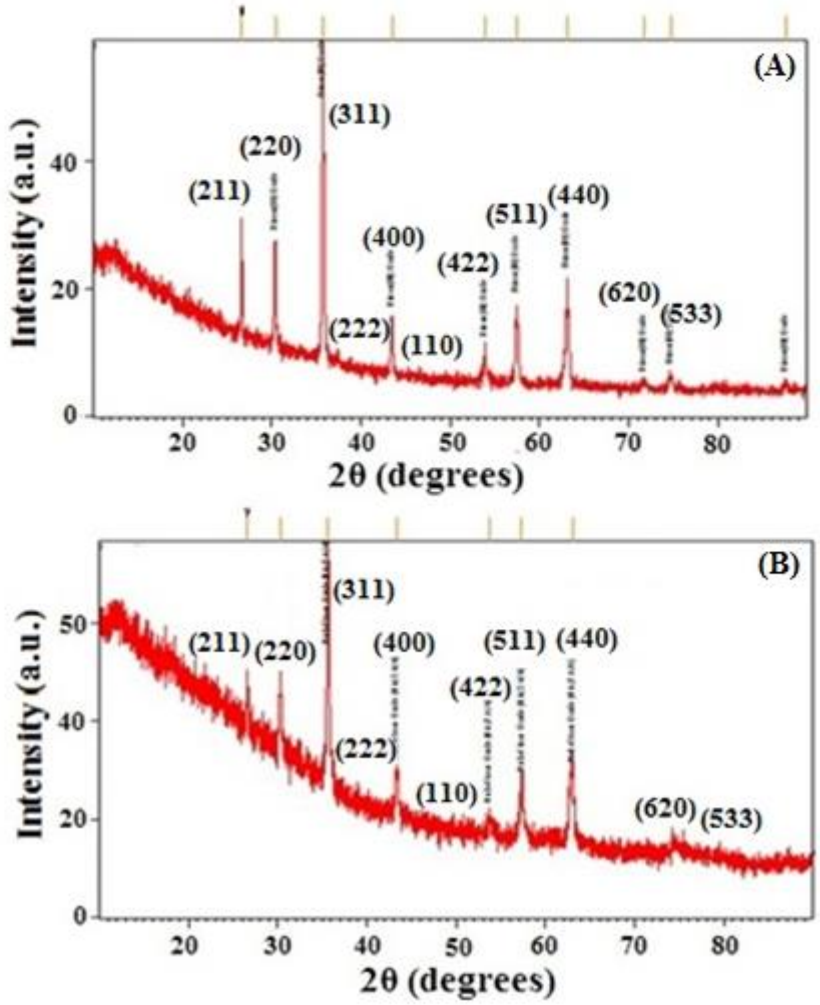

Figure 3.2 XRD pattern of (A) Iron oxide and (B) IO@NiNPs

Table 3.1 to 3.4 Shows XRD peak analyses of iron oxides

Table 3.1 Formula: Fe$_{2.667}$O$_4$ (Maghemite (γ-Fe$_2$O$_3$, Phase – I)

2θ (degrees)	(hkl)
30.30	201
35.63	312
43.34	401
53.87	419
57.34	333
63.00	404

Table 3.2 Formula: Fe_3O_4 (Magnetite (Fe_3O_4, Phase – II))

2θ (degrees)	(hkl)
18.42	111
30.30	202
35.70	131
37.44	222
43.40	040
53.88	242
57.54	151
63.13	404

Table 3.3 Formula: Fe_2O_3 (Hematite (α-Fe_2O_3, Phase – III))

2θ (degrees)	(hkl)
24.26	0,1,2
33.31	0,-1,4
35.82	-1,-1,0
49.76	0,2,4
54.39	1,1,6
62.80	2,1,4
64.34	3,0,0

Table 3.4 Formula: FeOOH (Goethite, Phase – IV)

2θ (degrees)	(hkl)
27.02	110
36.14	011
36.33	200

It is also observed that pattern is dominated by maghemite (γ-Fe_2O_3) and magnetite (Fe_3O_4) phases. It is to be noted here that the peak positions of both the phases are very nearby to each other, hence exact identification is very difficult. However, based on the intensity distribution, it can be concluded that the sample consists of majority of maghemite or magnetite phase along with hematite as secondary phase and goethite as impurity phase. XRD pattern is similar to reported data.[29-30] SEM-EDX of IO also showed the presence of Fe metal (**Figure 3.3**).

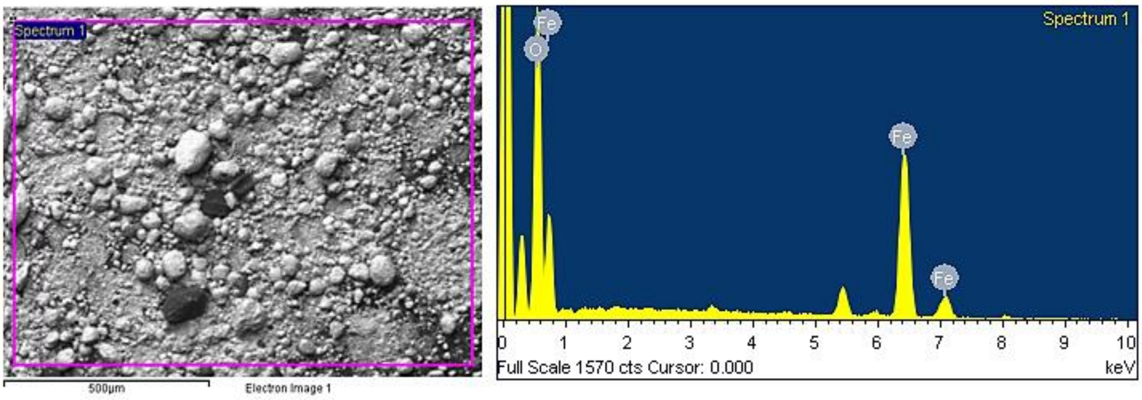

Figure 3.3 SEM-EDX analysis of Iron oxide

3.1.3.2 Synthesis and characterizations of IO@NiNPs

Template synthesis method was used for synthesis of magnetic separable core/shell nanoparticles. This method is mainly used to generate specific nanostructures of bimetallic nanoalloys which are otherwise very difficult to prepare. This approach utilizes pre-formed iron oxide of the first metal and subsequently directing the deposition of the Ni metal onto a surface site. In the present study nanosized nickel was deposited on iron oxide under sonication and using starch as capping agent. This method is commonly used to prepare core–shell or multi-shell morphologies. Starch capping was proved by FT-IR (**Figure 3.4**). The FT-IR spectra of pure starch (**Figure 3.4A**) and IO@NiNPs (**Figure 3.4B**) both display the typical profile of polysaccharides in the range 920–1100 cm^{-1} (characteristic peaks attributed to C-C/C-O bond stretching). The peaks at 1020–1100 cm^{-1} are characteristic of the anhydroglucose ring. The peaks at 1402–1420 cm^{-1} are due to C-H bending. It is seen that the peak at 1642 cm^{-1} shifts to 1623 cm^{-1} in the IO@NiNPs. The shifts observed in the spectra can be attributed to the interaction of NPs with starch. The band at 2901–2928 cm^{-1} is characteristic of C–H stretching. A broad band due to hydrogen bonded hydroxyl group (O–H) appeared at 3400–3420 cm^{-1} and is attributed to the complex vibrational stretching, associated with free, inter and intra molecular bound hydroxyl groups

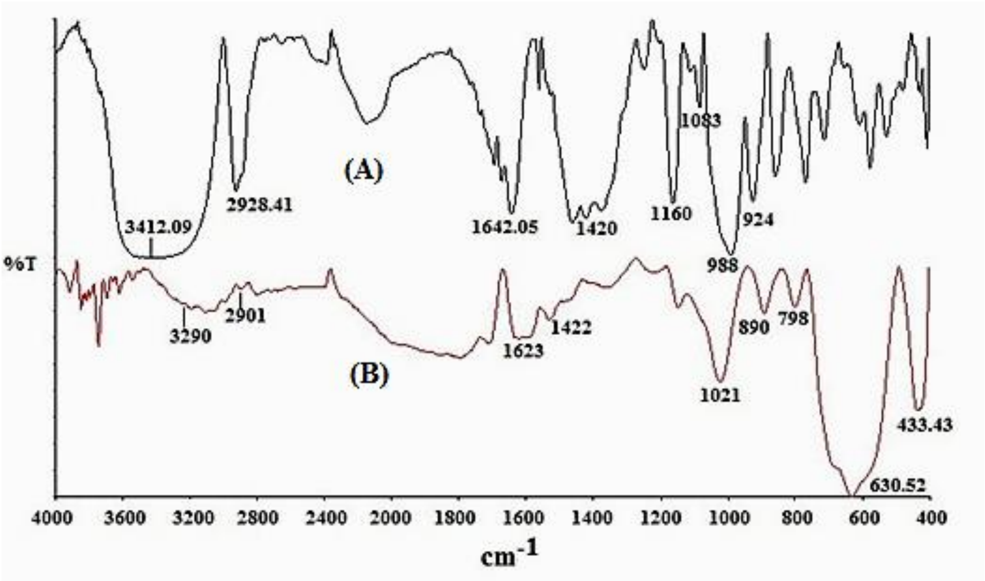

Figure 3.4 FT-IR spectra of (A) Starch and (B) Starch capped IO@NiNPs

Figure 3.2B shows the XRD pattern of IO@NiNPs. The signals of Ni were not detected in the XRD spectrum of IO@NiNPs although the position and relative intensity of diffraction peaks are reasonably close to the reported pattern.[24b,31] XRD pattern shows that the MNPs are well-crystalline and exhibit diffraction peaks corresponding to (111), (220), (311), (400), (511) and (440) planes of cubic crystal system. XRD pattern indicate mixed phases of iron oxides with Nickel.

The weight percentage of Ni was determined to be 1.98 % by AAS analysis and Energy Dispersive X-ray Analysis (EDX) also confirm the ratio 1.89:98.11 (Ni/Iron oxide) (**Figure 3.5A**). EDX analysis indicates that the well-cleaned final product is mostly composed of O, Fe and Ni, with no other signal (**Figure 3.5A**).

The magnetic measurements have been carried out at room temperature, and the data are shown in **Figure 3.5B**, on the as-prepared iron oxide and IO@NiNPs. From the recorded M−H loop, it is clear that both the as-prepared samples are ferromagnetic at RT. The magnetization of the as-prepared iron oxide was 1.6269 emu, and it decreased to a value of 1.5259 emu after coating of NiNPs. The coercivity values of the IO and IO@NiNPs were 73.65 and 61.76 G, respectively. The low magnetization value exhibited by the IO@NiNPs compared to the iron oxide one could be due to the presence of impurities/defects in the IO@NiNPs. Since the size of nanoparticles synthesized by us lies in the range of 20−50 nm, they are still ferromagnetic.

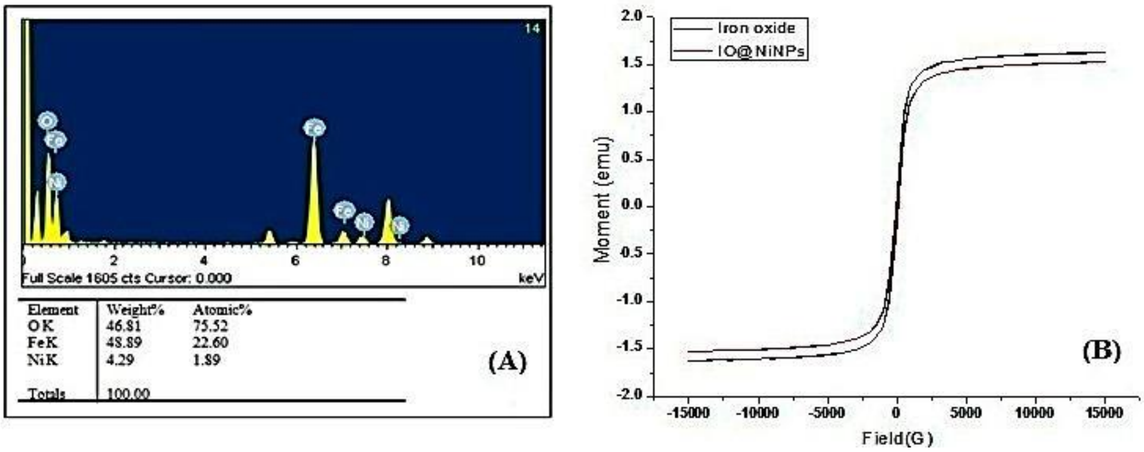

Element	Weight%	Atomic%
O K	46.81	75.52
FeK	48.89	22.60
NiK	4.29	1.89
Totals	100.00	

Figure 3.5 (A) EDX patterns and (B) Magnetic hysteresis curve of as-prepared IO and IO@NiNPs

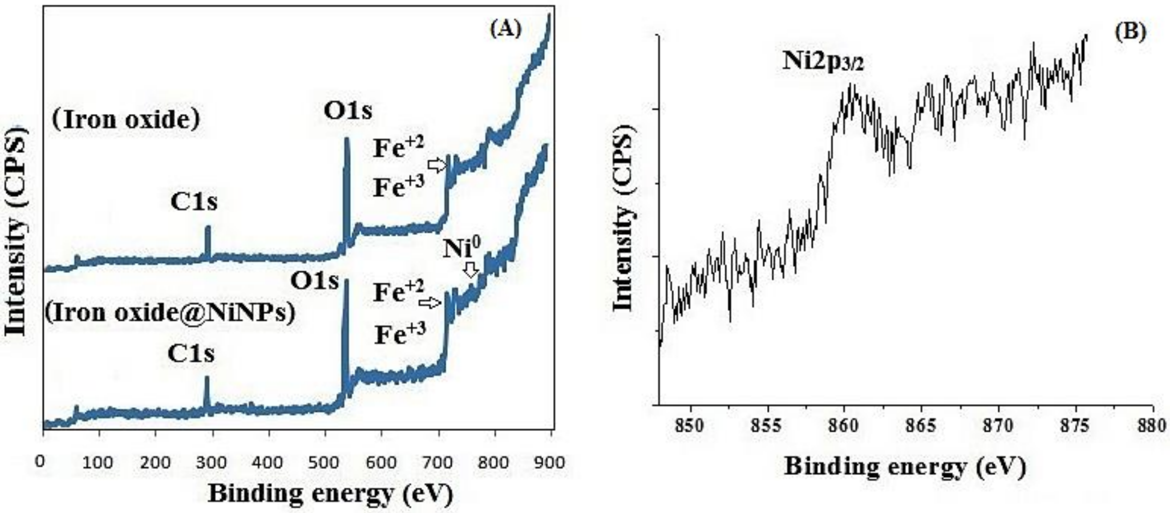

Figure 3.6 (A) X-ray photoelectron spectra of IOs and IO@NiNPs **(B)** Expanded XPS region of IO@NiNPs

In order to give further evidence of formation of NiNPs shell over the iron oxide core and to determine the oxidation state of Ni, XPS resolution Ni 2p spectroscopy results of iron oxide and IO@NiNPs were compared (**Figure 3.6A**). The signals of Ni were very faint in the XPS spectrum of IO@NiNPs (**Figure 3.6B**) because of low loading of Nickel metal. Nevertheless, for a better understanding of the oxidation state of Ni metal, the binding energy obtained from the catalyst was compared with the Ni metal $2p_{3/2}$ peak position. The peak value obtained at 852.9 eV is within the range of literature value (852.7 eV ± 0.4 eV).[32] In agreement with the above analyses, it can be concluded that oxidation state of nickel in the catalyst is zero.

The Brunauer-Emmet-Teller (BET) surface area of a magnetic IO@NiNPs sample was determined to be 17.65 m^2/g. These results suggest that MNPs have high surface area (**Figure 3.7 and 3.8**). The pore size of the MNPs was determined to be 25.46 nm by the Barrett-Joyner-Halenda (BJH) analysis of the isotherms. The total pore volumes were 0.051cm^3/g (supporting information). The High-Resolution Transmission Electron Microscopy (HR-TEM) images of IO@NiNPs are shows somewhat spherical morphology with some cubic partials an average size range of 20–50 nm (**Figure 3.9A**). **Figure 3.9B** and **C** are HR-TEM images of typical IO@NiNPs at different magnifications. The high resolution images in **Figure 3.9D** and **E** shows well developed lattice fringes and the fringes extend throughout the particle confirming the monocrystalline nature of the individual particles. The distance between adjacent lattice fringes measured as 0.221nm in **Figure3.9D** corresponds to the 311 reflection. The selected area electron diffraction (SAED) pattern shown in **Figure 3.9F** corresponds to the higher order reflections of IO@NiNPs.[33] The HR-TEM image (**Figure 3.9**) clearly shows that nickel is deposited on the iron oxide surface. In accordance with the above analyses, it can be concluded that the nanoparticles prepared in this method are mixture iron oxide with nickel metal nanoparticles.

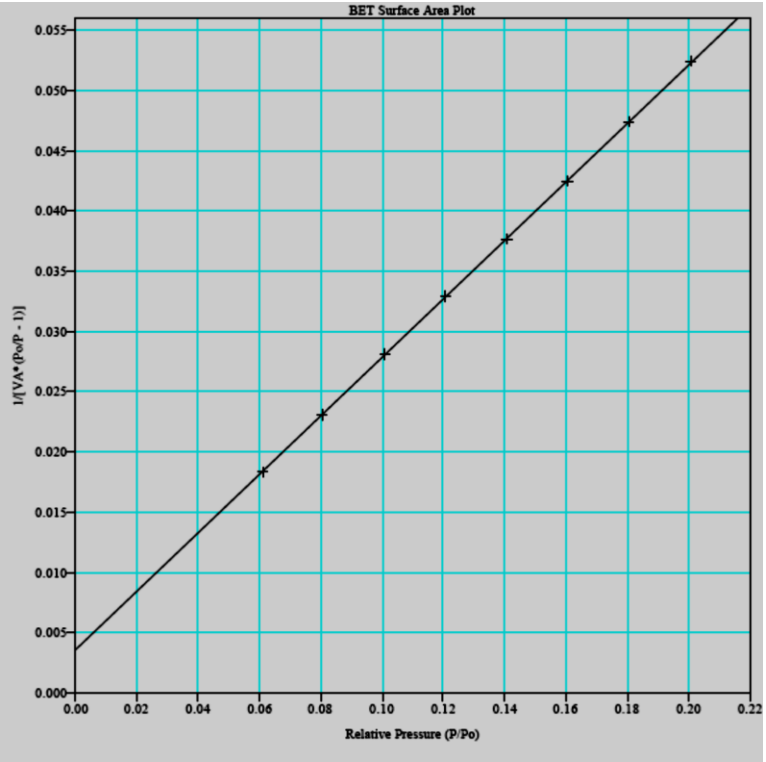

Figure 3.7 BET Surface area Plot for IO@NiNPs

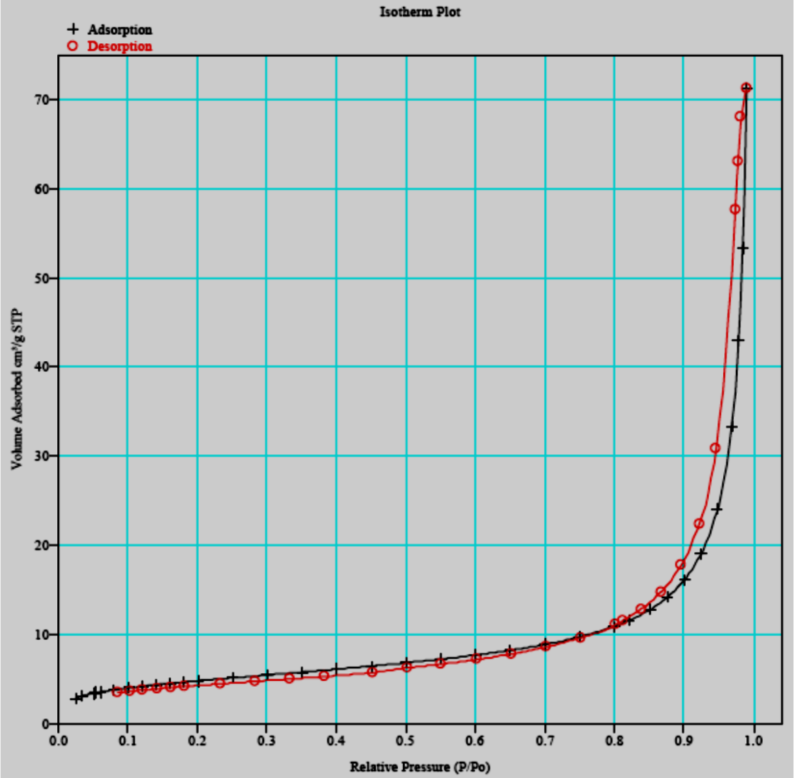

Figure 3.8 BET Isotherm Plot for IO@NiNPs

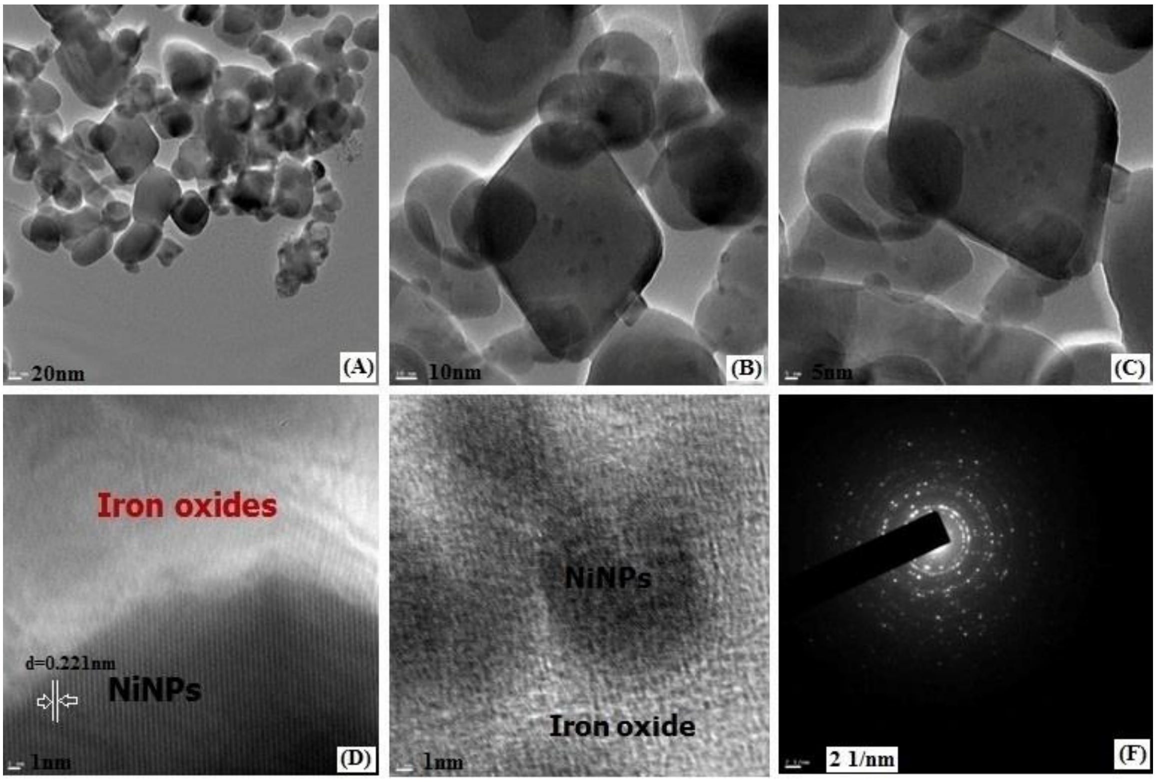

Figure 3.9 HR-TEM images of magnetic IO@NiNPs at different magnifications (A) 20nm;(B) 10nm and (C) 5nm showing particle size distribution; The resolved lattice fringes and SAED pattern of IO@NiNPs are (D), (E) and (F) respectively.

3.1.3.3 Catalytic reduction of *p*-Nitroaniline and other aromatic nitro compounds

The IO@Ni core-shell nanoparticles were used as catalyst for the hydrogenation of aromatic nitro compounds using $NaBH_4$ as the hydrogen donor and water as solvent as shown in **Scheme 3.2**. For Initial screening reduction of *p*-Nitoaniline (PNA) to yield *p*-Phenylenediamine (PPDA) was investigated under various reaction conditions (table-1). The conversion was monitored by UV-vis spectrophotometer, where the product and reactant show different absorption bands at 307nm and 381nm, respectively as shows in **Figure 3.10**.

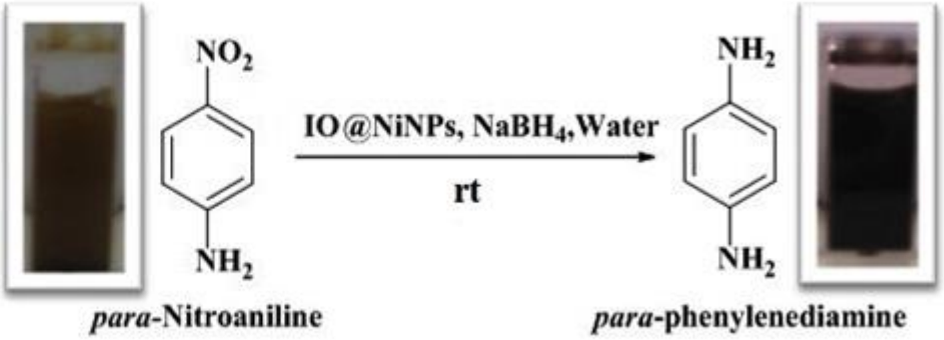

Scheme 3.2 Schematic representation of IO@NiNPs catalysed reduction of PNA to PPDA by $NaBH_4$

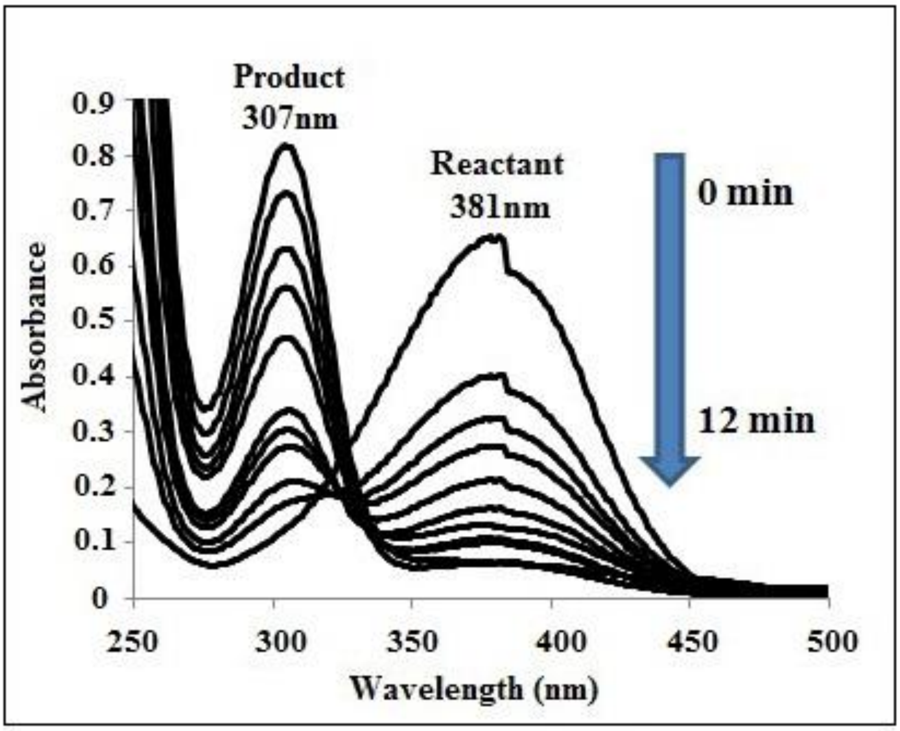

Figure 3.10 UV-vis spectra indicating the conversion of *p*-Nitroaniline to *p*-Phenylenediamine in presence of IO@NiNPs

Table 3.5 Optimization of reaction conditions for hydrogenation of *p*-Nitroaniline.

Sr. No.	Catalyst (mg) (IO@NiNPs)	$NaBH_4$ (mmol)	Temperature ($^\circ$C)	Time (h\min)	%Yield[b] (±2%)
1	none	None	25-30 to reflux	24h	-
2	12	,,	,,	,,	< 5
3	none	1.85	,,	,,	< 10
4	IO[c]	1.85	rt	,,	55
5	12	1.85	,,	12min	96
6[a]	**12**	**1.44**	**,,**	**12min**	**96**
7	,,	1.03	,,	20min	,,
8	,,	0.61	,,	30min	,,
9	,,	0.20	,,	24h	90
10	,,	0.02	,,	24h	40
11	18	1.44	,,	12	96
12	15	,,	,,	12	,,
13	9	,,	,,	23	,,
14	6	,,	,,	32	,,
15	3	,,	,,	39	,,
16	0.3	,,	,,	180	,,

Reaction conditions: *p*-Nitroaniline-0.362 mmol, solvent 2 mL (water), a-optimized reaction condition, b- Isolated yield, and c-Iron oxide only (20mg).

It is seen from the **Table 3.5** (entries 1-3) that the presence of a catalyst along with $NaBH_4$ is required for hydrogenation of PNA. In our previous study we have observed that nickel nanoparticle catalysed hydrogenation of PNA takes more than one hour.[25b] When the reaction was carried out using only IO, the reaction yields was very low (~ 50 to 55%) even after 24h at rt (**Table 3.5**, entry-4). When the reaction conditions mentioned in the **Table 3.5** (entry-6) were used, the reaction proceeded faster within 12 min and the λ_{max} shifted from 381nm to 307nm. Whereas, in the absence of NPs, the peak at 381nm corresponding to PNA did not disappear even after 24h of reflux. The optimum reaction conditions for PNA reaction are given in **Table 3.5** (entry 6), which yields 96±2 % of product at rt after 12min and selectivity was 100%.

Nanocatalysts can catalyze the reduction of nitro compounds by acting as an electronic relay system to overcome the kinetic barrier, in which the electrons donated by BH_4^- can be transferred to the acceptor nitro groups.[34] The *p*-Nitroaniline and BH_4^- were adsorbed by the electronic hole in the surface of the NiNPs via chemical adsorption. Immediately, *p*-Phenylenediamine was produced on the surface of NPs. In the second step, the PPDA was desorbed from the surface of the NPs. A detailed mechanism has been proposed by Xie *et al*.[35]

Furthermore, experiments were performed using a different mole ratio of $NaBH_4$ in standard reaction. When we decrease moles of $NaBH_4$ from 1.85 mmol to 1.44 mmol the yield and reaction time did not change (**Table 3.5**, entry 5 and 6), whereas using 1.44 mmol of $NaBH_4$ resulted into a remarkable yield (96±2%) at 25-30°C within 12min (**Table 3.5**, entry 6). However, further lowering the amount of $NaBH_4$ caused an increase in the reaction time (entry 6 to 10) and hence an adequate quantity of $NaBH_4$ was used in optimum reaction condition.

Variation in quantity of NPs (**Table 3.5**, entries 11 to 16) under optimum reaction conditions showed that even 0.3 mg was sufficient for catalyzing the reaction at rt. But the reaction time increased to 180 min for maximum conversion (**Table 3.5**, entry 16). On the other hand with 9 mg the reaction time decreased to 23min (**Table 3.5**, entry 9). Beyond 12 mg the reaction time and yield did not change (**Table 3.5**, entries 11 and 12).

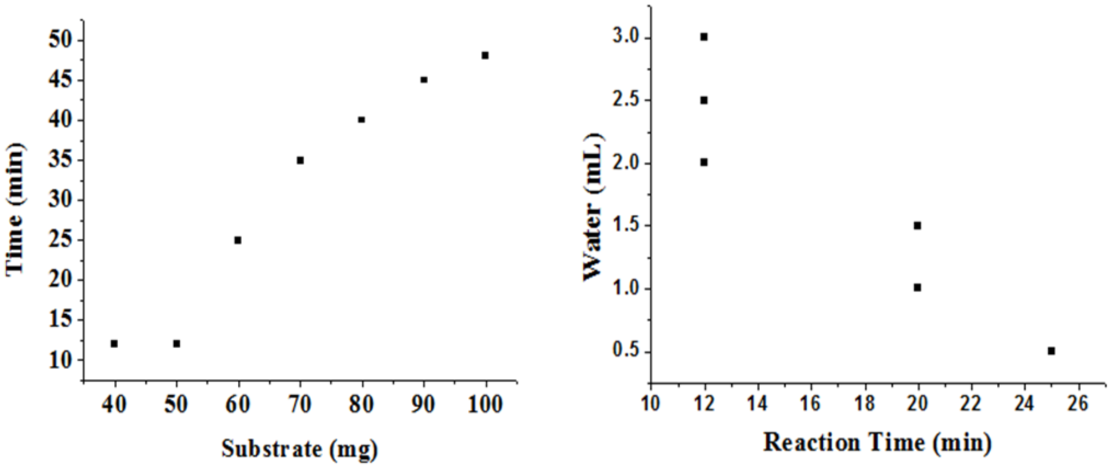

Figure 3.11 Reduction of PNA to PPDA at different concentration of substrate and water (under optimum conditions)

In order to assess the efficiency of the NPs further, the quantity of water and substrate were also optimized (**Figure 3.11**). **Figure 3.11** shows that, under optimum conditions (**Table 3.5**, entry-6) when the quantity of substrate was increased the reaction time decreased. Similarly, when quantity of solvent (water) was decreased the reaction time increased. After optimization of the reaction conditions (**Table 3.5** and **Figure 3.11**) the catalytic activity of magnetic IO@Ni core-shell NPs, with other nitro substrates was further explored (**Scheme 3.3**). The catalytic performance of the nanocatalyst, was not significantly influenced by the nature and position of the substituents on the aromatic nitro compounds. Electron-donating as well as -withdrawing groups such as –Cl, –Br, CH_3 and –OH did not have significant influence on the reaction (**Table 3.6**). Notably, electron transfer over IO@Ni core-shell nanocatalyst exhibits excellent activity and selectivity for the hydrogenation of a series of halogenated nitrobenzenes to the corresponding halogenated amines, without any dehalogenation (**Table 3.6**, entries 10, 11, 16-20 and 23). All the nitro arenes were reduced in excellent yields affording a single product, which minimizes the efforts to separate unreacted starting compounds. In all cases, the turnover number (TON) was as high as ~102 to 115 and turnover frequency (TOF) ~ 2 to 12 per site per min. (**Table 3.6**).

Further, this catalytic system works efficiently in aqueous system and therefore no hazardous solvent was required. This reaction has been investigated in the presence of other protic solvents such as methanol, ethanol, and ethylene glycol; however, none of them gave satisfactory results (data not given). In an aqueous system $NaBH_4$ gives sodium metaborate ($NaBO_2$)[36] which is the only waste generated during the reaction. However sodium metaborate can be recycled using magnesium hydride (MgH_2) or magnesium silicide (Mg_2Si) by annealing (350–750◦C) under high H_2 pressure (0.1–7 MPa) for 2–4 h.[36] This opens up new possibilities for eco-friendly synthesis of aromatic amines.

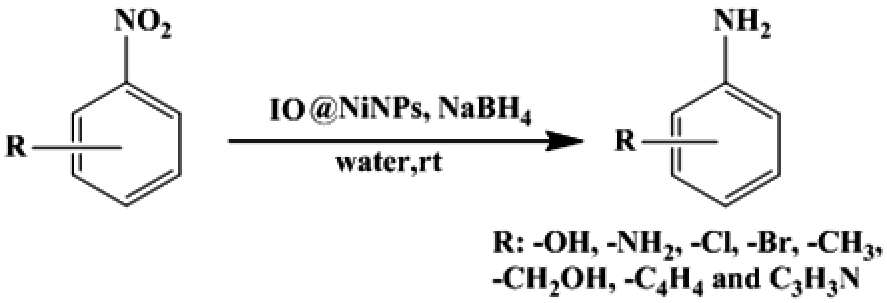

Scheme 3.3 General scheme for reduction of various Nitro aromatics

Table 3.6 Chemoselective Reduction of Nitroaromatics to Aromatic Amines at rt by IO@NiNPs.

S. No	Substrate	Product	Time (min±2)	Yield[a] (%±3)	TON(±2)/TOF (min^{-1})[b]
1	*o*-Nitrotoluene	*o*-Toulidine	24	89	106/4.45
2	*p*-Nitrotoluene	*p*-Toulidine	13	92	110/8.49
3	*m*-Nitrotoluene	*m*-Toulidine	16	94	112/7.05
4	*o*-Nitrophenol	*o*-Aminophenol	09	92	110/12.26
5	*p*-Nitrophenol	*p*-Aminophenol	10	90	108/10.8
6	*m*-Nitrophenol	*m*-Aminophenol	17	90	108/6.3
7	*p*-Nitrobenzyl alcohol	*p*-Aminobenzyl alcohol	13	89	106/8.15
8	*m*-Nitrobenzyl alcohol	*m*-Aminobenzyl alcohol	13	94	112/8.61
9	*o*-Nitrobenzyl alcohol	*o*-Aminobenzyl alcohol	15	95	114/7.6
10	4-Chloro-3-nitro aniline	4-Chlorobenzene-1,3-diamine	30	91	109.2/3.64
11	4-Chloro-2-nitro aniline	4-Chlorobenzene-1,2-diamine	40	90	108/2.7
12	Nitrobenzene	Aniline	25	95	114/4.56
13	*o*-Nitroaniline	*o*-Phenylenediamine	16	94	112.8/7.05
14	*m*-Nitroaniline	*m*-Phenylenediamine	14	94	112.8/8.05
15	*p*-Nitroaniline	*p*-Phenylenediamine	12	96	115/9.6
16	*o*-Chloronitobenzene	*p*-Chloroaniline	19	93	111.6/5.87
17	*m*-Chloronitobenzene	*m*-Chloroaniline	22	94	112.8/5.12
18	*p*- Bromonitobenzene	*p*- Bromoaniline	17	95	114/6.7

19	*o*-Bromonitobenzene	*o*-Bromoaniline	21	95	114/5.4
20	*m*-Bromonitobenzene	*m*-Bromoaniline	29	94	112/3.86
21	6-Nitroquinoline	Quinolin-6-amine	35	94	112/3.2
22	1-Nitronaphthalene	1-Naphthylamine	38	93	111.6/2.93
23	4-chloro-2-methyl-1-nitrobenzene	2-Amino-5-Chlorotoluene	50	88	105.6/2.11
24	3-Nitroquinoline	Quinolin-3-amine	40	92	110.4/2.76
25	1,3-dinitrobenzene	*m*-Phenylenediamine	30	89	106.8/3.56
26	1,2-dinitrobenzene	*o*-Phenylenediamine	28	85	102/3.64
27	1,4-dinitrobenzene	*p*-Phenylenediamine	28	92	110.4/3.94

Reaction conditions: All reactions were carried at rt, substrate-0.362 mmol, catalyst-12mg (0.45wt% or 1.06 mol% NiNPs of Substrate), $NaBH_4$-1.44 mmol and solvent 2mL (water), (a) Isolated yield after column chromatography (b) TON and TOF was calculated on basis of NiNPs

3.1.3.4 Recycling of IO@NiNPs

The IO@Ni core-shell NPs were recovered by external magnetic separation (**Figure 3.12A; a and b**) with negligible loss. Recycling experiments carried out under optimized conditions showed interesting results. It was observed that the NPs could be reused directly without further purification for 30 consecutive runs as can be seen in **Table 3.7** with very high total turnover number (TTN) 3456. Up to 16 cycles there was no loss in activity. After that, however, the reaction time increased with each successive recycling experiment reaching from 12 min to 140 min finally. This may be due to gradual loss of the catalytic activity of the nanocatalyst with number of runs which may be due to various reasons. One of the reasons may be surface modification due to deposition of matter during reaction.[37]

Table 3.7 Reduction of PNA to PPDA at rt (25-30°C using IO@NiNPs in optimum condition (Recycling experiments)

Cycle	Time(min±2)	Yield[a](±1%)	IY[b](±3%)	Cycle	Time(min)	Yield[a](±1%)	IY[b](±3%)
1	12	98	96	16	22	99	96
2	12	99	96	17	30	98	96
3	14	98	96	18	36	98	96
4	13	98	96	19	35	99	95
5	13	98	96	20	42	99	95
6	16	98	96	21	45	99	96
7	15	97	96	22	46	99	96
8	16	98	96	23	45	99	96
9	21	98	96	24	45	98	95
10	25	98	96	25	47	99	96
11	24	99	96	26	45	98	96
12	21	99	96	27	44	99	96
13	25	98	96	28	59	98	96
14	21	98	96	29	70	98	95
15	24	98	96	30	140	98	96

(a) GC yield, (b) Isolated yield

The HR-TEM images of the nanocatalyst recorded after 30th run displays an agglomeration of NPs due to deposited matter (**Figure 3.12B and C**). The image in **Figure 3.12D** shows that lattice fringes were damaged by deposited matter throughout the particle. The SAED pattern shown in **Figure 3.12E** corresponds to the reflections of IO@NiNPs still confirming the crystalline nature of the catalyst; but the catalytic activity reduces due to deposited matter. Nevertheless, the reaction does proceed to completion at the same temperature at the end of 30 cycles giving the same yield. Further the reused IO@NiNPs was also characterized by EDX and atomic absorption spectrophotometer (AAS) to confirm the leaching of nickel during reaction. EDX analysis reveals that the Ni content in IO@NiNPs which was 1.89% before the reaction showed a marginal decrease to 1.53% (**Figure 3.12F**) after the reusability study of 30 cycles. This confirmed that only negligible leaching of nickel occurred which was further supported by AAS results (**Table 3.8**). Ferrous and ferric ion leaching were also ensured by AAS (**Table 3.8**). High recyclability and stability of IO@NiNPs can be attributed to the presence of starch coating which makes the IO@NiNPs stable to water and air and maintains the metallic state of nickel in catalyst.[38] This eventually increases their utility and enhances recycling efficiency. Thus the metal surface, capping agent and $NaBH_4$ simultaneously make the IO@NiNPs system an effective catalyst.

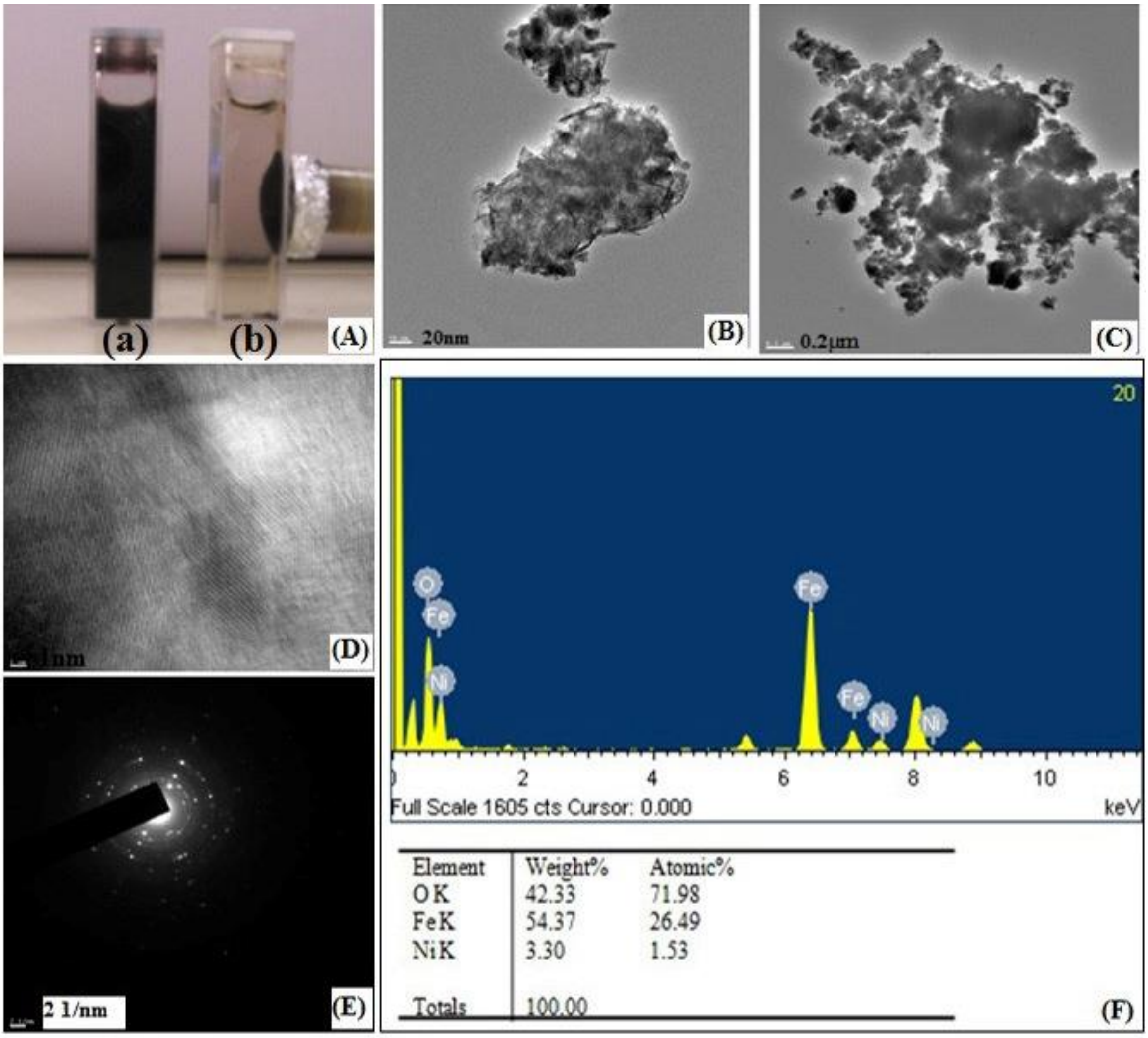

Element	Weight%	Atomic%
O K	42.33	71.98
FeK	54.37	26.49
NiK	3.30	1.53
Totals	100.00	

Figure 3.12 (A) Reaction mixture of PPDA (a) before and (b) after magnetic separation by simple magnet; HR-TEM of reused magnetic IO@NiNPs at different magnifications (B) 20 nm, (C) 0.2 μm, (D) (E) 1nm (lattice fringes) and (F) SAED pattern of IO@NiNPs

Table 3.8 Leaching study by AAS after each recycling experiment[a]

Cycle	Fe leaching (ppm)	Ni leaching (ppm)	Cycle	Fe leaching (ppm)	Ni leaching (ppm)	Cycle	Fe leaching (ppm)	Ni leaching (ppm)
1	0.067	0.028	11	0.052	0.034	21	0.022	0.020
2	0.026	0.036	12	0.089	0.058	22	0.012	0.023
3	0.105	0.020	13	0.045	0.045	23	0.078	0.024
4	0.102	0.021	14	0.100	0.045	24	0.012	0.025
5	0.052	0.025	15	0.101	0.025	25	0.015	0.025
6	0.022	0.028	16	0.023	0.052	26	0.010	0.012
7	0.101	0.025	17	0.028	0.012	27	0.045	0.023
8	0.082	0.024	18	0.014	0.010	28	0.013	0.029
9	0.025	0.023	19	0.045	0.019	29	0.014	0.022
10	0.007	0.024	20	0.111	0.018	30	0.012	0.021

a- All experiment were carried out under optimum condition

3.1.4 Conclusion

The present study demonstrated the feasibility of using a waste from iron ore beneficiation plants (IOTs) as one of the starting materials for the synthesis of IO@Ni core-shell MNPs and its possible applications in the catalysis. Core-shell IO@Ni nanoparticles were successfully synthesized by using wet chemical method without any organic solvent and surfactant. A highly efficient, viable heterogeneous IO@Ni core-shell MNPs catalyst was developed for hydrogenation reaction using environment friendly solvent water. Due to sturdy interaction between NiNPs and iron oxide, the catalyst could be reused by recycling 30 times, without any significant loss in catalytic activity and selectivity. The reaction was broadly applicable as diverse aromatic nitro compounds were successively converted to the corresponding amines in excellent yield (85–96%), high TON and TOF. Being robust and magnetically separable, this core-shell catalyst is a promising candidate for other important organic conversions and industrial applications.

3.1.5 References

1. (a) P. T. Anastas and J. C. Warner, *Green Chemistry Theory and Practice*, Oxford University Press, Oxford, 1998; (b) A. S. Matlack, *Introduction to Green Chemistry*, Marcel Dekker, New York, 2001;(c) J. H. Clark and D. J. Macquarrie, *Handbook of Green Chemistry and Technology*, Blackwell Publishing, Abingdon, 2002; (d) V. Polshettiwar and R. S. Varma, *Chem. Soc. Rev.*, 2008, **37**, 1546.
2. (a) V. Polshettiwar and R. S. Varma, *Aqueous Microwave Chemistry*, RSC Publishing, Cambridge, 2010; (b) V. Polshettiwar and R. S. Varma, *Acc. Chem. Res.*, 2008, **41**, 629; (c) R. B. N. Baig and R. S. Varma, *Chem. Commun.*, 2012, **48**, 5853; (d) R. B. N. Baig and R. S. Varma, *Chem. Soc. Rev.*, 2012, **41**, 1559.
3. (a) S. Wittmann, A. Shatz, R. N. Grass, W. J. Stark and O. Reiser, *Angew. Chem., Int. Ed.*, 2010, **49**, 1867; (b) M. Benaglia, Recoverable and Recyclable Catalysts, John Wiley & Sons, Chichester, 2009;(c) V. Polshettiwar and R. S. Varma, *Green Chem.*, 2010, **12**, 743.
4. (a) F. Alonso, P. Riente and M. Yus, *Acc. Chem. Res.*, 2011, **44**, 379; (b) F. Alonso and M. Yus, *Pure Appl. Chem.*, 2008, **80**, 1005; (c) N. Yan, C. Xiao and Y. Kou, *Coord. Chem. Rev.*, 2010, **254**, 1179; (d) S. Shylesh, V. Schnemann and W. R. Thiel, *Angew. Chem. Int. Ed.*, 2010, **49**, 3428; (e) V. Polshettiwar, R. Luque, A. Fihri, H. Zhu, M. Bouhrara and J-M. Basset, *Chem. Rev.*, 2011, **111**, 3036.
5. (a) R. B. N. Baig and R. S. Varma, *Chem. Commun.*, 2013, **49**, 752; (b) V. Polshettiwar and R. S. Varma, *Green Chem.*, 2010, **12**, 743–754
6. (a) T. Hirakawa and P. V. Kamat, *J. Am. Chem. Soc.*, 2005, **127**, 3928; (b) Y. J. Huang, X. C. Zhou, M. Yin, C. P. Liu and W. Xing, *Chem. Mater.*, 2010, **22**, 5122; (c) J. X. Wang, H. Inada, L. J. Wu, Y.M. Zhu, Y.M. Choi, P. Liu,W. P. Zhou and R. R. Adzic, *J. Am. Chem. Soc.*, 2009, 131, 17298; (d) K. Bakhmutsky, N. L. Wieder, M. Cargnello, B.Galloway, P. Fornasiero and R. J. Gorte, *Chem Sus Chem*, 2012, **5**, 140; (e) H. L. Jiang, T. Akita and Q. Xu, *Chem. Commun.*, 2011, **47**, 10999; (f) J. Bao, J. He, Y. Zhang, Y. Yoneyama and N. Tsubaki, *Angew. Chem., Int. Ed.*, 2008, **47**, 353; (g) H. L. Jiang, T. Akita, T. Ishida, M. Haruta and Q. Xu, *J. Am. Chem. Soc.*, 2011, **133**, 1304; (q) R. G. Chaudhuri and S. Paria, *Chem. Rev.*, 2012, **112**, 2373 and references cited therein.

7. M. B. Gawande, H. Guo, A. K. Rathi, P. S. Branco, Y. Chen, R. S. Varma and D-L. Peng, *RSC Adv.*, 2013, **3**, 1050 and references cited therein.
8. V. Polshettiwar, R. Luque, A. Fihri, H. Zhu, M. Bouhrara, and J-M. Basset, *Chem. Rev.*, 2011, **111**, 3036.
9. P. S. Haddad, T. M. Martins, L. D. Souza-Li, L. M. Li, K. Metze, R. L. Adam, M. Knobel and D. Zanchet, *Mater. Sci. Eng.*, 2008, **28**, 489–494.
10. S. Si, A. Kotal, T. K. Mandal, S. Giri, H. Nakamura and T. Kohara, *Chem. Mater.*, 2004, **16,** 3489.
11. A. Zablotskaya, I. Segal, E. Lukevics, M. Maiorov, D. Zablotsky, E. Blums, I. Shestakova and I. Domracheva, *J. Magn. Magn. Mater.*, 2009, **321**, 1428.
12. W. Cai and J. Wan, *J. Colloid Interface Sci.*, 2007, **30**, 366.
13. D. Maity and D. C. Agrawal, *J. Magn. Magn. Mater.*, 2007, **308**, 46.
14. S. K. Das, S. Kumar and P. Ramachandrarao, *Waste Manag.*, 2000, **20**, 725.
15. H. Yu, X. Xue and D. Huang, *Mater. Res. Bull.*, 2009, **44**, 2112.
16. C. Li, H. Sun, Z. Yi and L. Li, *J. Hazard. Mater.*, 2010, **174**, 78.
17. L. Zeng, X. Li and J. Liu, *Water Res.*, 2004, **38**, 1318.
18. S. Zhang, S. Xue, X. Liu, P. Duan, H. Yang, T. Jiang, D. Wang and R. Liu, *J. Min. Sci.*, 2006, **42**, 403.
19. S. K. Giri, N. N. Das, G. C. Pradhana, *Coll Surf A*, 2011, **389**, 43.
20. (a) A. M. Tafesh and J. Weiguny, *Chem. Rev.*, 1996, **96**, 2035; (b) Jr. R. J. Rahaim and Jr. R. E. Maleczka, *Org. Lett.*, 2005, **7**, 5087; (c) S. Chandrasekhar, S. J. Prakash and C. L. Rao, *J. Org. Chem.*, 2006, **71**, 2196; (d) Q. Shi, R. Lu, L. Lu, X. Fu and D. Zhao, *Adv. Synth. Catal.*, 2007, **349**, 1877.
21. (a) C. Yu, B. Liu and L. Hu, J. Org. Chem., 2001, 66, 919–924, and references therein; (b) A. K. Shil and P. Das, *Green Chem.*, 2013, DOI: 10.1039/C3GC41179F
22. A. Saha and B. Ranu, *J Org Chem*, 2008, **73**, 6867 and references therein
23. A. Corma and P. Serna, *Science*, 2006, **313**, 332.
24. (a) N. Sahiner, S. Butun and P. Ilgin, *Coll Surf A*, 2011, **386**,16; (b) M. B. Gawande, A. K. Rathi, P. S. Branco, I. D. Nogueira, A. Velhinho, J. J. Shrikhande, U. U. Indulkar, R. V. Jayaram, C. A. A. Ghumman, N. Bundaleski, and O. M. N. D. Teodoro, *Chem. Eur. J.*, 2012, **18**, 12628; (c) R. Dey, N. Mukherjee, S. Ahammed and B. C. Ranu, *Chem. Commun.*, 2012, **48**, 7982.

25. (a) P. S Rathore, J. Advani, S. Rathore and S. Thakore, *J Mol Catal A: Chem*, 2013, **377**, 129; (b) P. S Rathore, R. Patidar, S. Rathore and S. Thakore, *Catal Lett*, 2013, DOI 10.1007/s10562-013-1168-2
26. V. S. Madeira, 2010. Coal Mine Residues Recycling for the Fabrication of High Added Value Products. Ph.D. thesis. Federal University of Santa Catarina, Brazil (in Portuguese).
27. S. L. F. Andersen, R. G. Flores, V. S. Madeira, H. J. José and R. F. P. M. Moreira, *Ind. Eng. Chem. Res.*, 2012, **51**,767.
28. R. G. Flores, S. L. F. Andersen, L. K. K. Maia, H. J. José and R. F. P. M. Moreira, *J. Environ. Manage*., 2012, **111**, 53.
29. W. Kim, C-Y. Suh, S-W. Cho, K-M. Roh , H. Kwon, K. Song and I-J. Shon, *Talanta*, 2012, **94**, 348.
30. Y. Ren, R. Cingolani, R. Buonsanti, P. D. Cozzoli, V. Petkov, *J. Am. Chem. Soc.*, 2009, **131**, 14264.
31. N. Kimizuka, S. Sasaki and K. Tsukimura, *Jpn. J. Appl. Phys., Part 1*, 1997, **36**, 3609.
32. A. P. Grosvenor, M. C. Biesinger, R. St. C. Smart and N. S. McIntrye, *Surf. Sci.*, 2006, **600**, 1771.
33. D. Maiti, U. Manju, S. Velaga and P. S. Devi, *Cryst. Growth Des.*, 2013, **13**, 3637
34. (a) X. Huang, X. Liao and B. Shi, *Green Chem*, 2011, **13**, 2801; (b) P. Herve´s, M. Pe´ rez-Lorenzo, L. M. Liz-Marza´n, J. Dzubiella, Y. Lu and M. Ballauff, *Chem. Soc. Rev.*, 2012, **41**, 5577.
35. Z. Jiang, J. Xie, D. Jiang, X. Wei and M. Chen, *Cryst Eng Comm*, 2013, **15**, 560–569.
36. Y. Kojima and T. Haga, *Int J Hydrogen En*, 2003, **28**, 989.
37. (a) J. J. Spivey, G. W. Roberts, B. H. Davies, Catalyst Deactivation, Elsevier, Amsterdam, 2001; (b) F. Alonso, P. Riente, J. A. Sirvent, M. Yus, *Appl. Catal. A: Gen.*, 2010, **378**, 42.
38. (a) M. Valodkar, P. S. Rathore, R. N. Jadeja, M. Thounaojam, R. V. Devkar and S. Thakore, *J. Hazar. Mater.*, 2012, **201-202**, 244;(b) J. M. Yan, X. B. Zhang, S. Han, H. Shioyama and Q. Xu, *Inorg. Chem.*, 2009, **48**, 7389.

(Spectral Data)

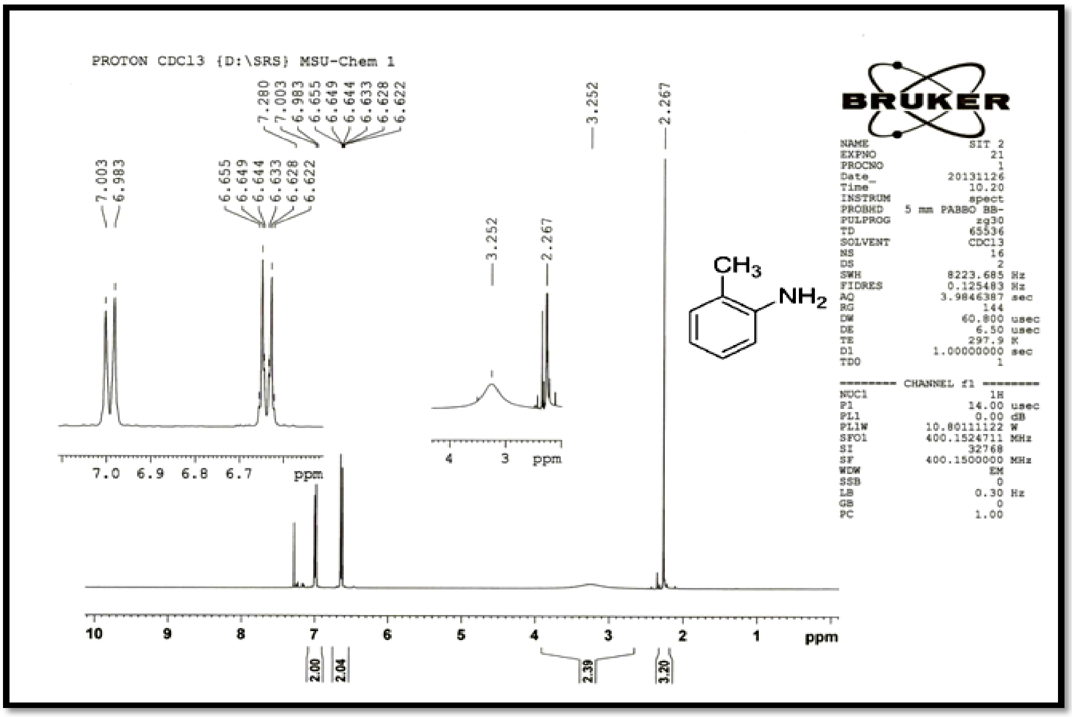

```
NAME            SIT 2
EXPNO              21
PROCNO              1
Date_        20131126
Time            10.20
INSTRUM         spect
PROBHD   5 mm PABBO BB-
PULPROG          zg30
TD              65536
SOLVENT         CDCl3
NS                 16
DS                  2
SWH          8223.685 Hz
FIDRES       0.125483 Hz
AQ          3.9846387 sec
RG                144
DW             60.800 usec
DE               6.50 usec
TE              297.9 K
D1         1.00000000 sec
TD0                 1

======== CHANNEL f1 ========
NUC1               1H
P1              14.00 usec
PL1              0.00 dB
PL1W      10.80111122 W
SFO1      400.1524711 MHz
SI              32768
SF        400.1500000 MHz
WDW                EM
SSB                 0
LB               0.30 Hz
GB                  0
PC               1.00
```

Figure S1 ^{1}HNMR spectra of *o*-Toulidine ($CDCl_3$, Table-3.6, Entry-1)

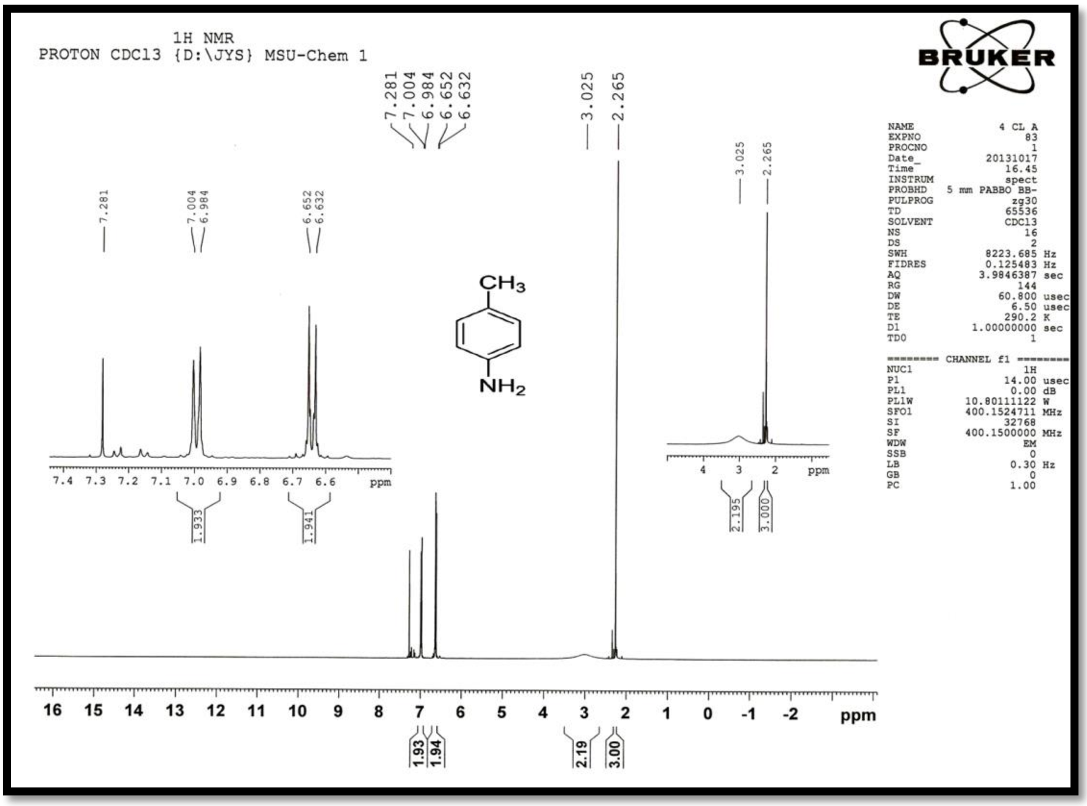

```
NAME            4 CL A
EXPNO              83
PROCNO              1
Date_        20131017
Time            16.45
INSTRUM         spect
PROBHD   5 mm PABBO BB-
PULPROG          zg30
TD              65536
SOLVENT         CDCl3
NS                 16
DS                  2
SWH          8223.685 Hz
FIDRES       0.125483 Hz
AQ          3.9846387 sec
RG                144
DW             60.800 usec
DE               6.50 usec
TE              290.2 K
D1         1.00000000 sec
TD0                 1

======== CHANNEL f1 ========
NUC1               1H
P1              14.00 usec
PL1              0.00 dB
PL1W      10.80111122 W
SFO1      400.1524711 MHz
SI              32768
SF        400.1500000 MHz
WDW                EM
SSB                 0
LB               0.30 Hz
GB                  0
PC               1.00
```

Figure S2 ^{1}HNMR spectra of *p*-Toulidine ($CDCl_3$, Table-3.6, Entry-2)

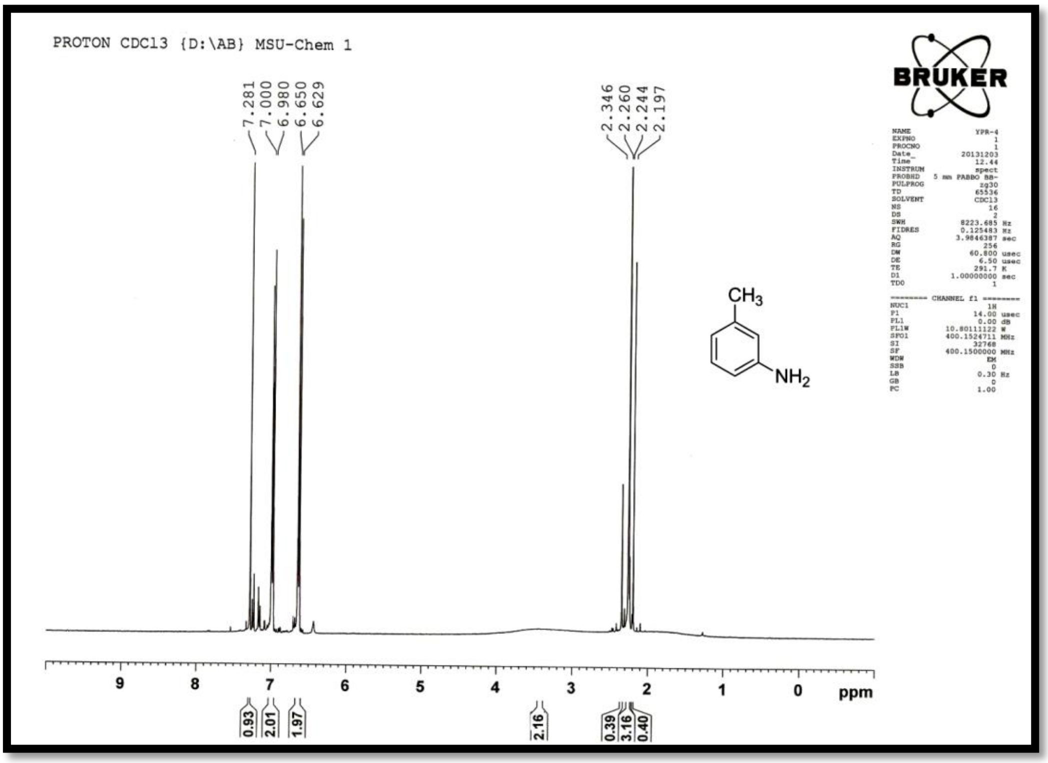

Figure S3 ^{1}HNMR spectra of *m*-Toulidine (CDCl$_{3,}$ Table-3.6, Entry-3)

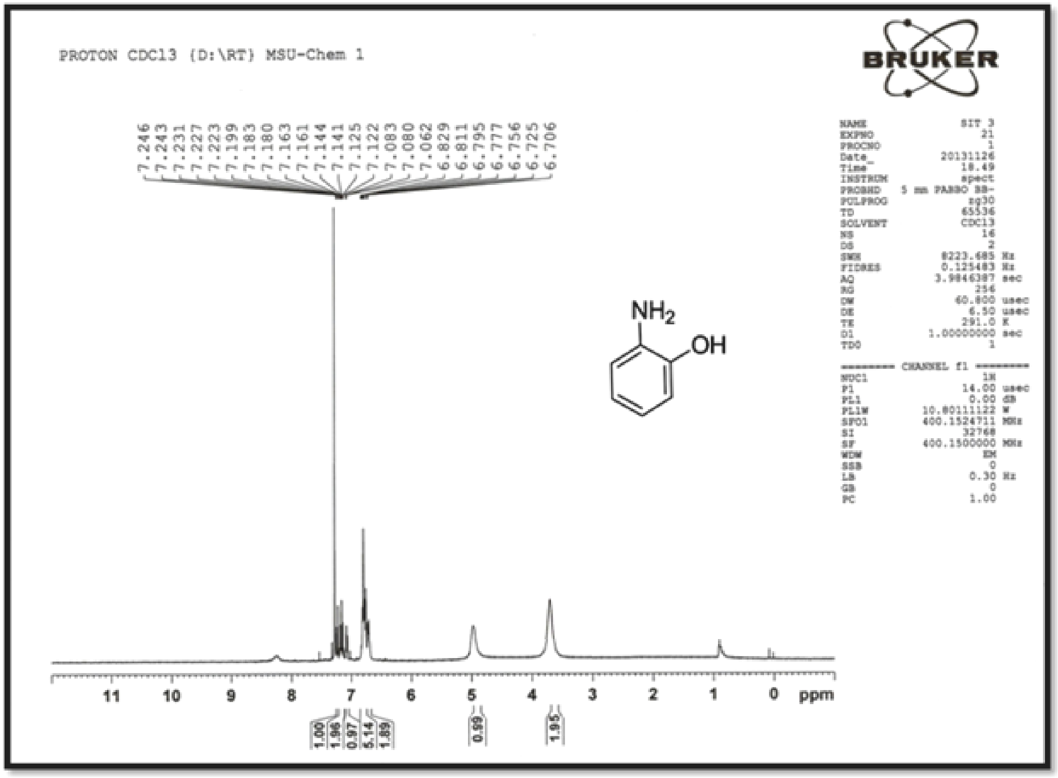

Figure S4 ^{1}HNMR spectra of *o*-Aminophenol (CDCl$_{3,}$ Table-3.6, Entry-4)

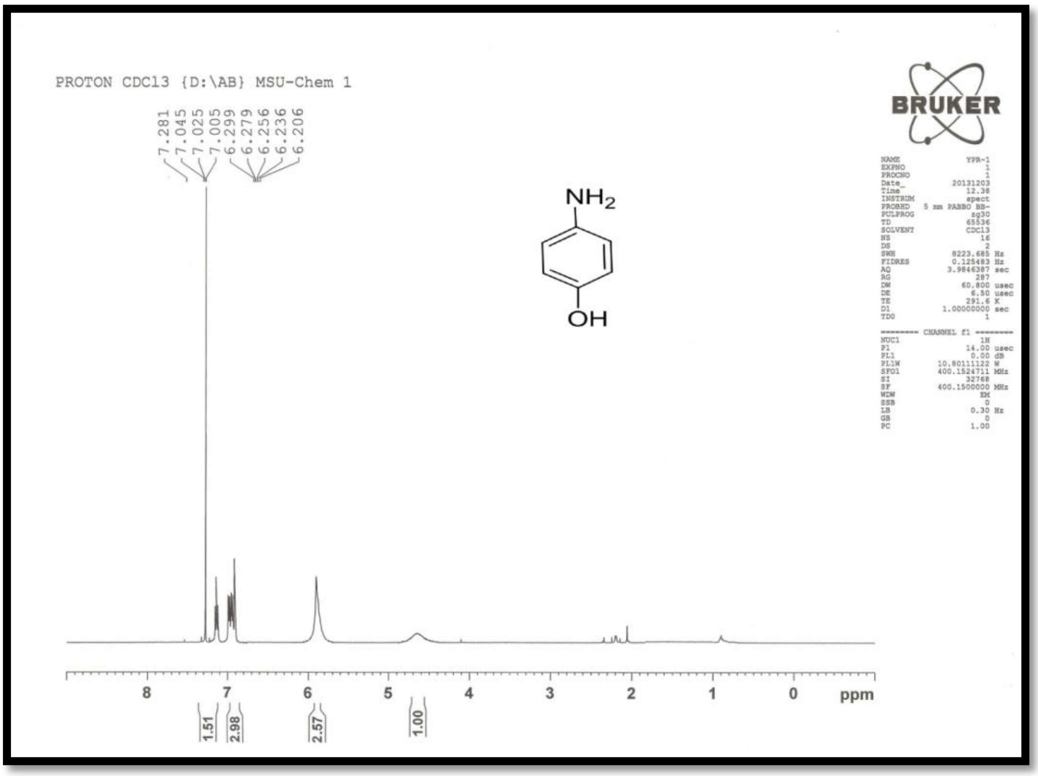

```
NAME           YPR-1
EXPNO              1
PROCNO             1
Date_       20131203
Time           12.38
INSTRUM        spect
PROBHD  5 mm PABBO BB-
PULPROG         zg30
TD             65536
SOLVENT        CDCl3
NS                16
DS                 2
SWH         8223.685 Hz
FIDRES      0.125483 Hz
AQ         3.9846387 sec
RG               287
DW            60.800 usec
DE              6.50 usec
TE             291.6 K
D1        1.00000000 sec
TD0                1

======== CHANNEL f1 ========
NUC1              1H
P1             14.00 usec
PL1             0.00 dB
PL1W     10.80111122 W
SFO1     400.1524711 MHz
SI             32768
SF       400.1500000 MHz
WDW               EM
SSB                0
LB              0.30 Hz
GB                 0
PC              1.00
```

Figure S5 ^{1}HNMR spectra of *p*-Aminophenol ($CDCl_3$, Table-3.6, Entry-5)

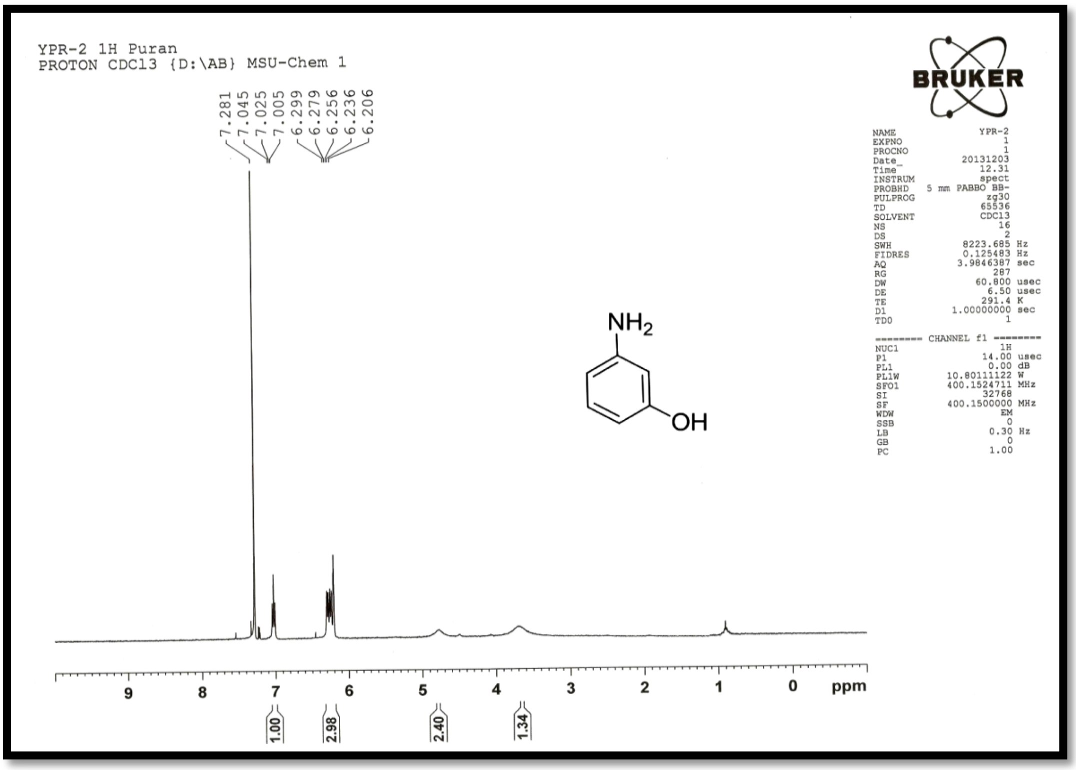

```
NAME           YPR-2
EXPNO              1
PROCNO             1
Date_       20131203
Time           12.31
INSTRUM        spect
PROBHD  5 mm PABBO BB-
PULPROG         zg30
TD             65536
SOLVENT        CDCl3
NS                16
DS                 2
SWH         8223.685 Hz
FIDRES      0.125483 Hz
AQ         3.9846387 sec
RG               287
DW            60.800 usec
DE              6.50 usec
TE             291.4 K
D1        1.00000000 sec
TD0                1

======== CHANNEL f1 ========
NUC1              1H
P1             14.00 usec
PL1             0.00 dB
PL1W     10.80111122 W
SFO1     400.1524711 MHz
SI             32768
SF       400.1500000 MHz
WDW               EM
SSB                0
LB              0.30 Hz
GB                 0
PC              1.00
```

Figure S6 ^{1}HNMR spectra of *m*-Aminophenol ($CDCl_3$, Table-3.6, Entry-6)

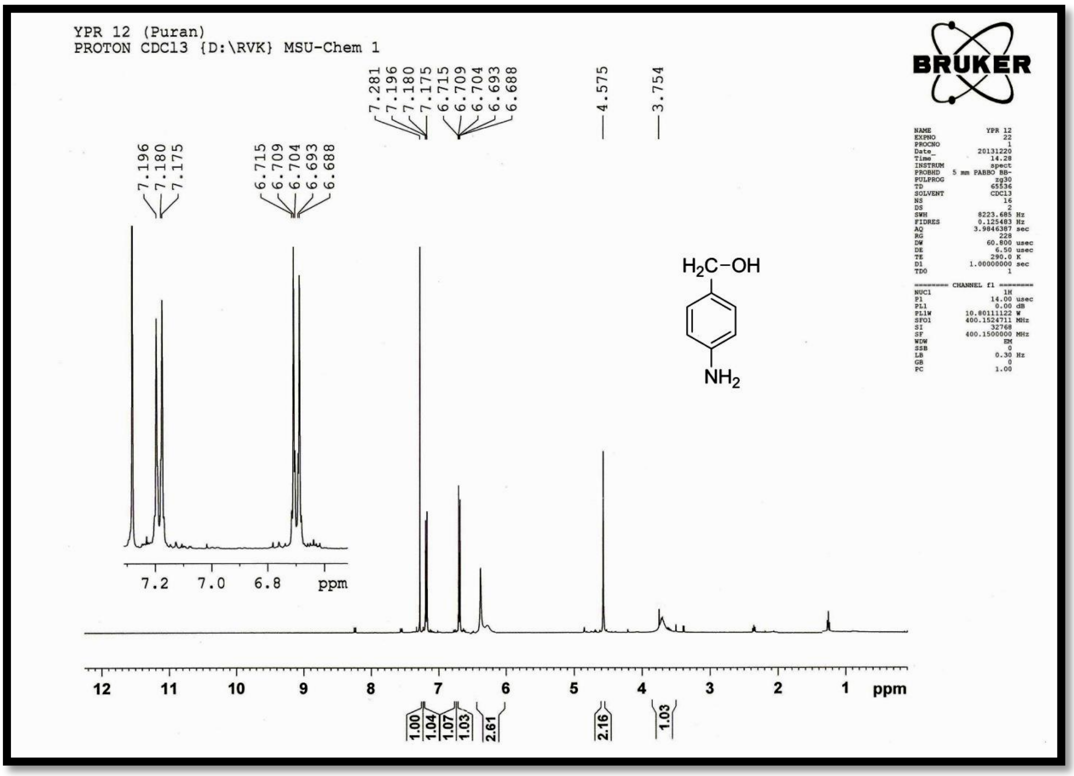

Figure S7 ^{1}HNMR spectra of *p*-Aminobenzyl alcohol (CDCl$_3$, Table-3.6, Entry-7)

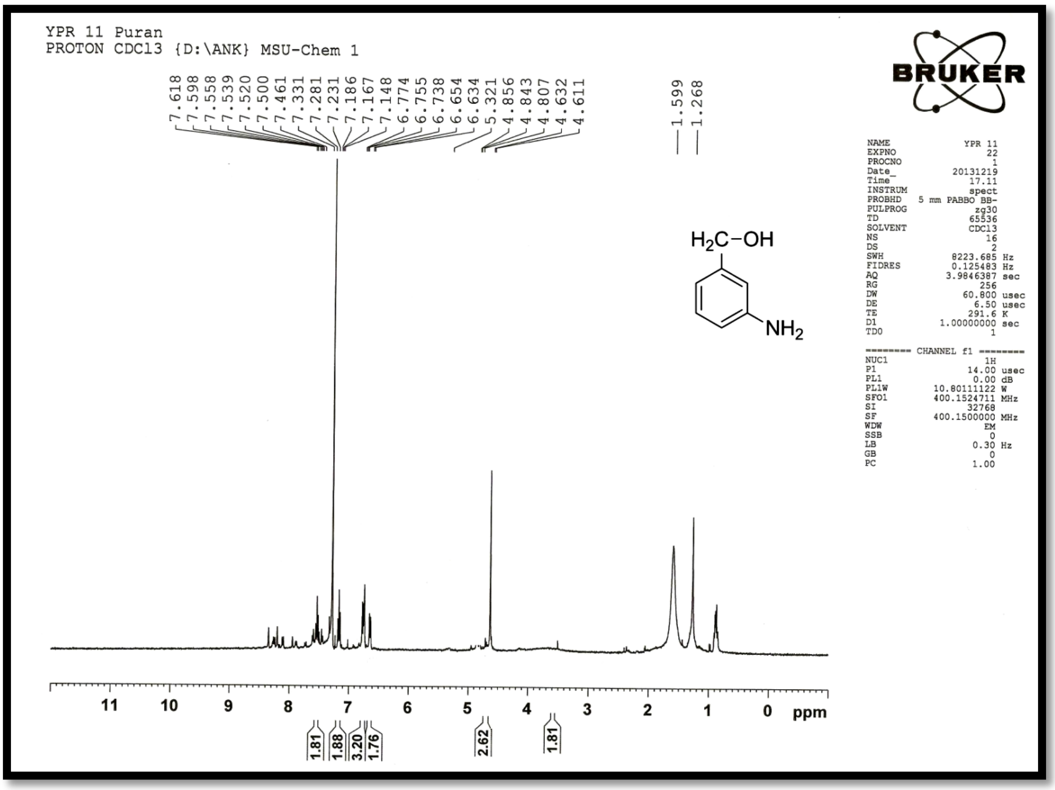

Figure S8 ^{1}HNMR spectra of *m*-Aminobenzyl alcohol (CDCl$_3$, Table-3.6, Entry-8)

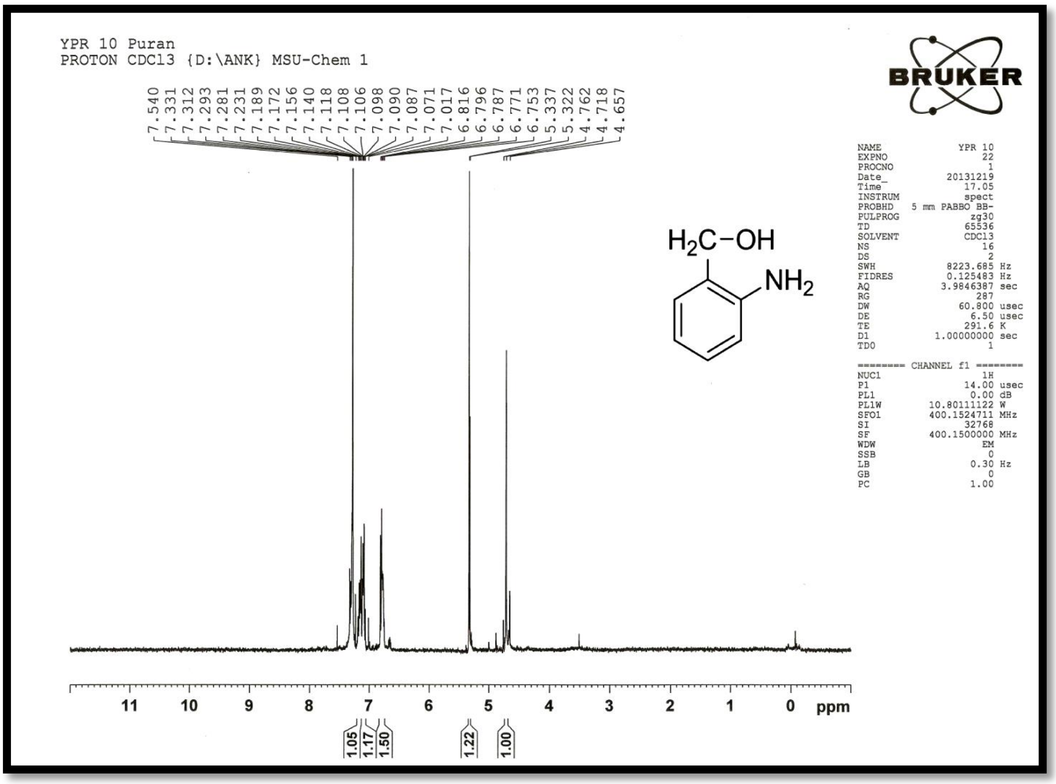

Figure S9 ^{1}HNMR spectra of *o*-Aminobenzyl alcohol ($CDCl_3$, Table-3.6, Entry-9)

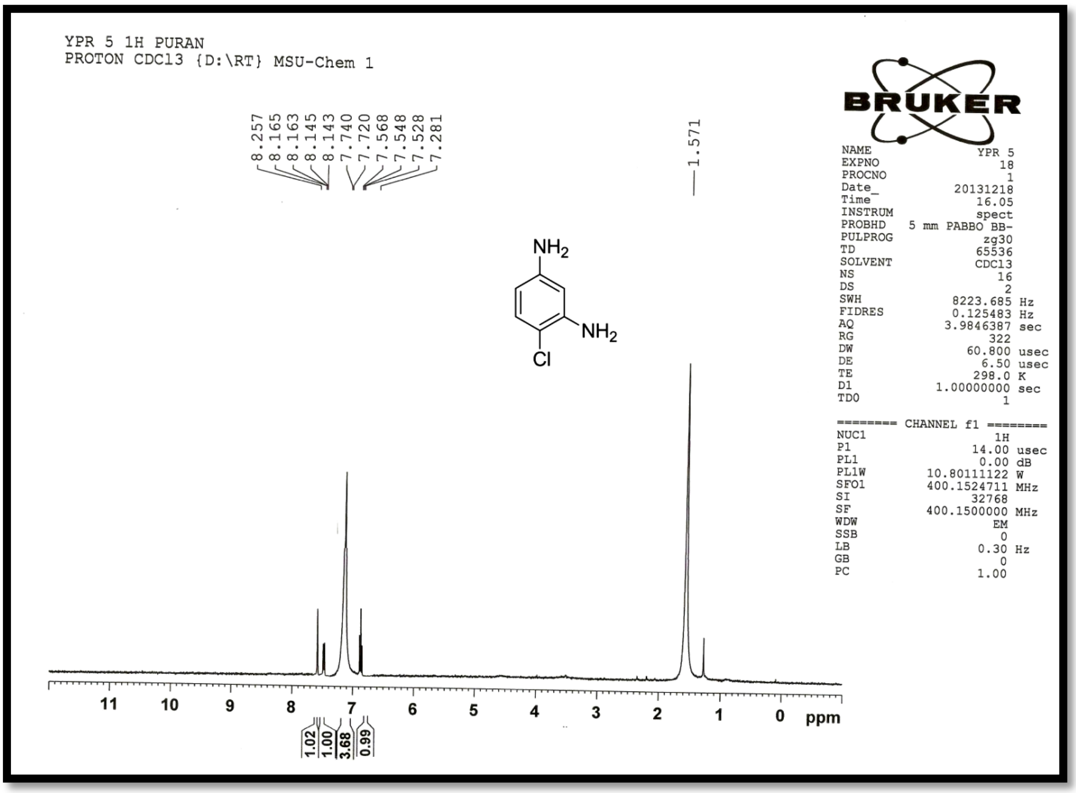

Figure S10 ^{1}HNMR spectra of 4-Chlorobenzene-1,3-diamine ($CDCl_3$, Table-3.6, Entry-10)

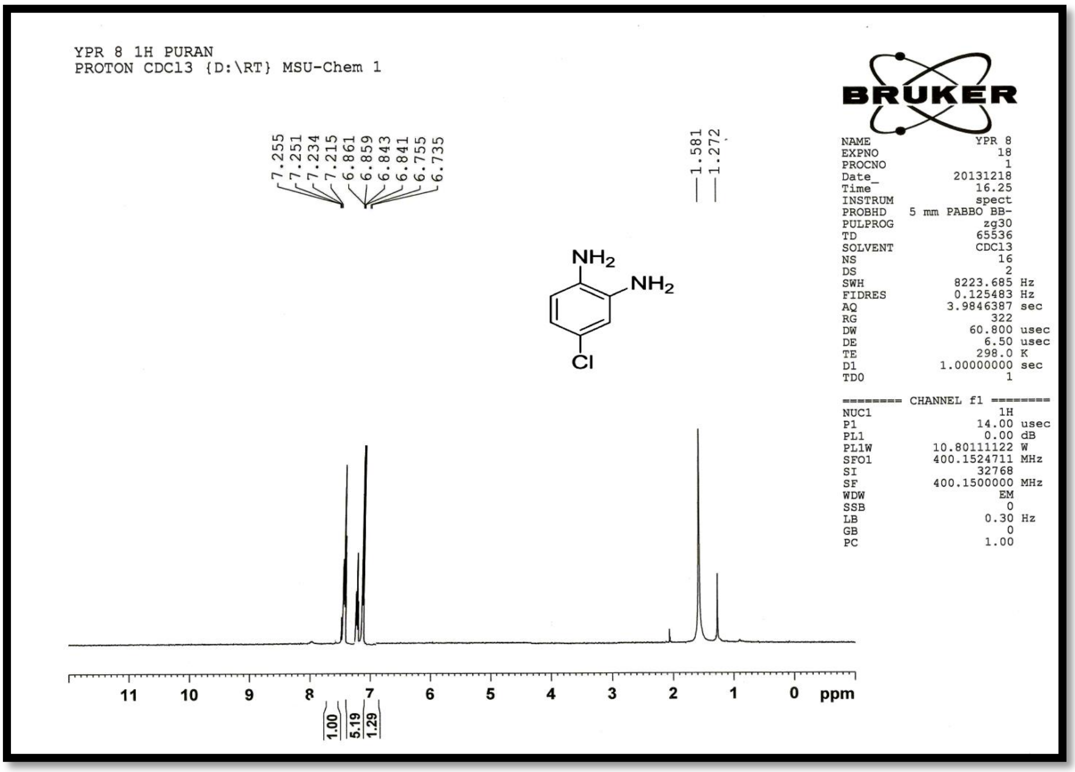

Figure S11 ^{1}HNMR spectra of 4-Chlorobenzene-1, 2-diamine (CDCl$_3$, Table-3.6, Entry-11)

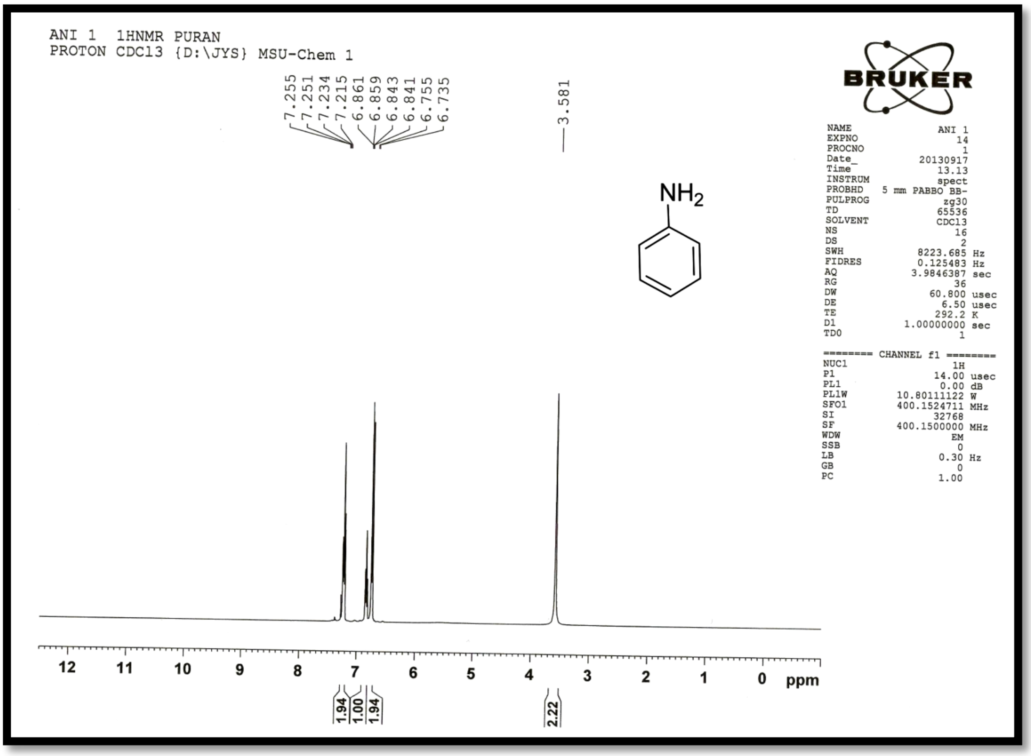

Figure S12 ^{1}HNMR spectra of Aniline (CDCl$_3$, Table-2, Entry-12)

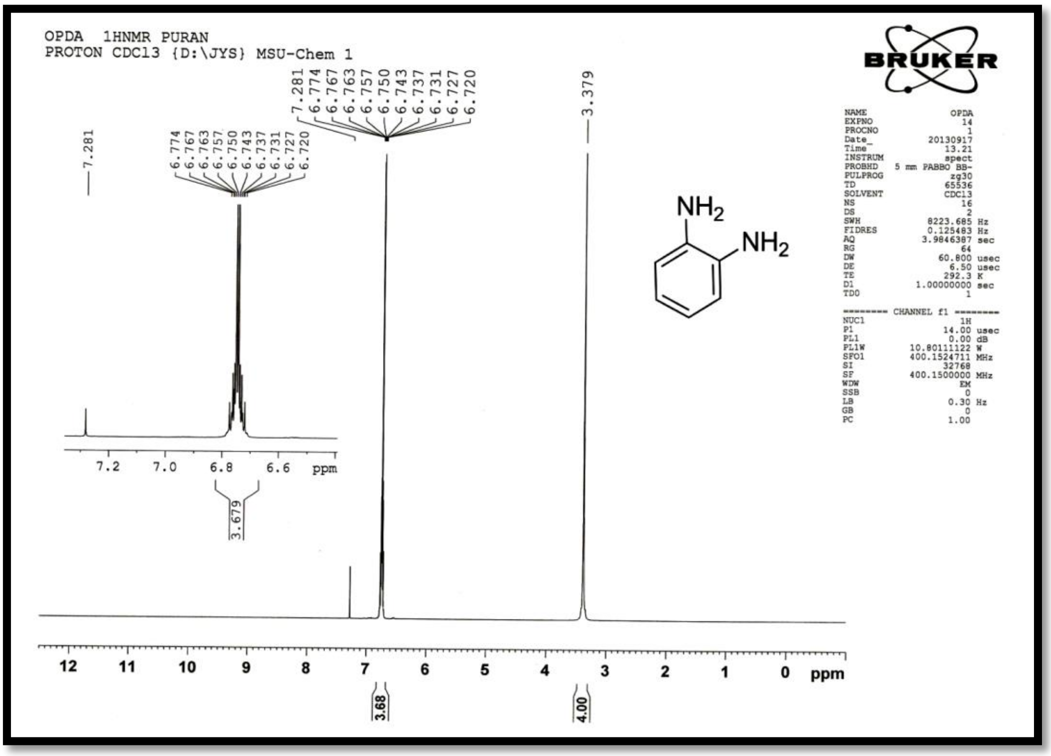

```
NAME            OPDA
EXPNO             14
PROCNO             1
Date_       20130917
Time           13.21
INSTRUM        spect
PROBHD   5 mm PABBO BB-
PULPROG         zg30
TD             65536
SOLVENT        CDCl3
NS                16
DS                 2
SWH         8223.685 Hz
FIDRES      0.125483 Hz
AQ         3.9846387 sec
RG                64
DW            60.800 usec
DE              6.50 usec
TE             292.3 K
D1        1.00000000 sec
TD0                1

======== CHANNEL f1 ========
NUC1              1H
P1             14.00 usec
PL1             0.00 dB
PL1W     10.80111122 W
SFO1     400.1524711 MHz
SI             32768
SF       400.1500000 MHz
WDW               EM
SSB                0
LB              0.30 Hz
GB                 0
PC              1.00
```

Figure S13 ^{1}HNMR spectra of *o*-Phenylenediamine ($CDCl_3$, Table-3.6, Entry-13 and similar spectra for Entry-26)

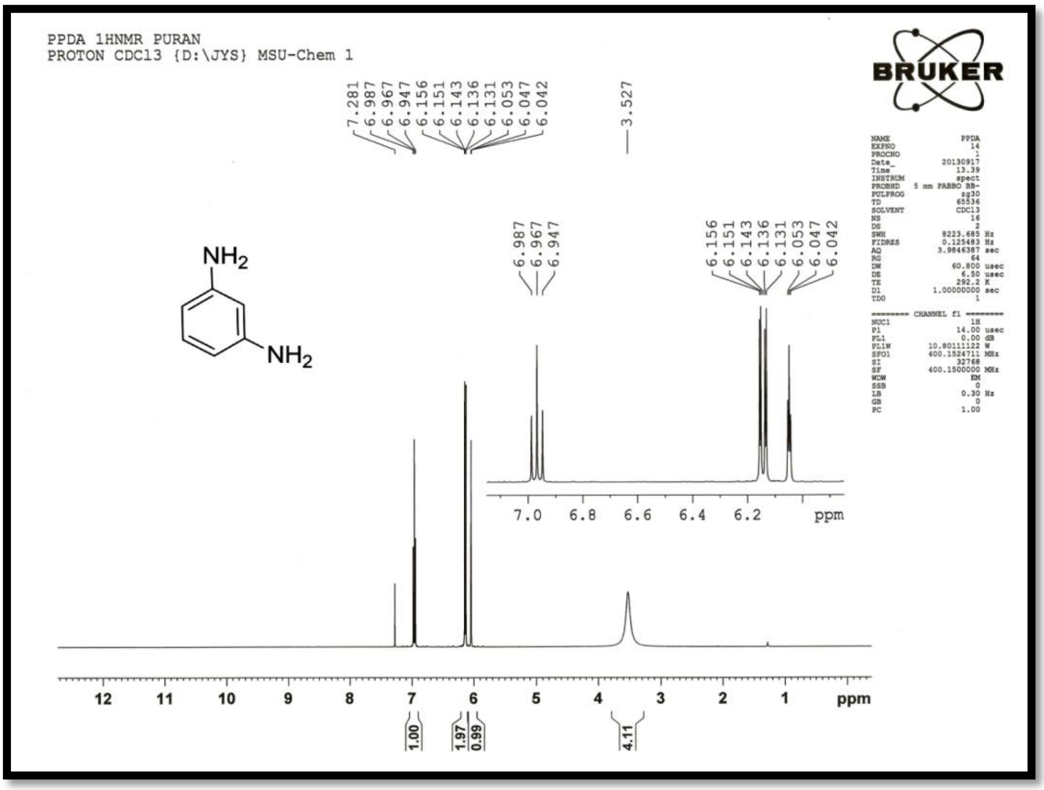

```
NAME            PPDA
EXPNO             14
PROCNO             1
Date_       20130917
Time           13.39
INSTRUM        spect
PROBHD   5 mm PABBO BB-
PULPROG         zg30
TD             65536
SOLVENT        CDCl3
NS                16
DS                 2
SWH         8223.685 Hz
FIDRES      0.125483 Hz
AQ         3.9846387 sec
RG                64
DW            60.800 usec
DE              6.50 usec
TE             292.2 K
D1        1.00000000 sec
TD0                1

======== CHANNEL f1 ========
NUC1              1H
P1             14.00 usec
PL1             0.00 dB
PL1W     10.80111122 W
SFO1     400.1524711 MHz
SI             32768
SF       400.1500000 MHz
WDW               EM
SSB                0
LB              0.30 Hz
GB                 0
PC              1.00
```

Figure S14 ^{1}HNMR spectra of *m*-Phenylenediamine ($CDCl_3$, Table-3.6, Entry-14 and similar spectra for entry-25)

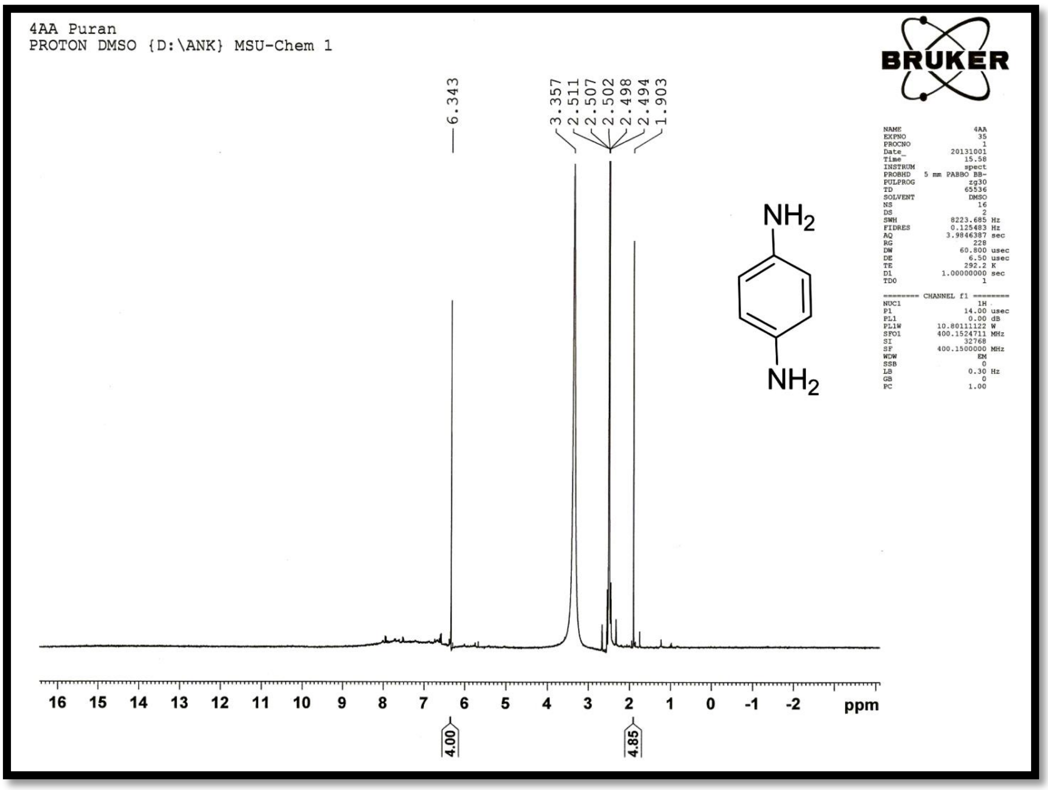

Figure S15 ^{1}HNMR spectra of *p*-Phenylenediamine (DMSO, Table-3.6, Entry-15 and similar spectra for entry-27)

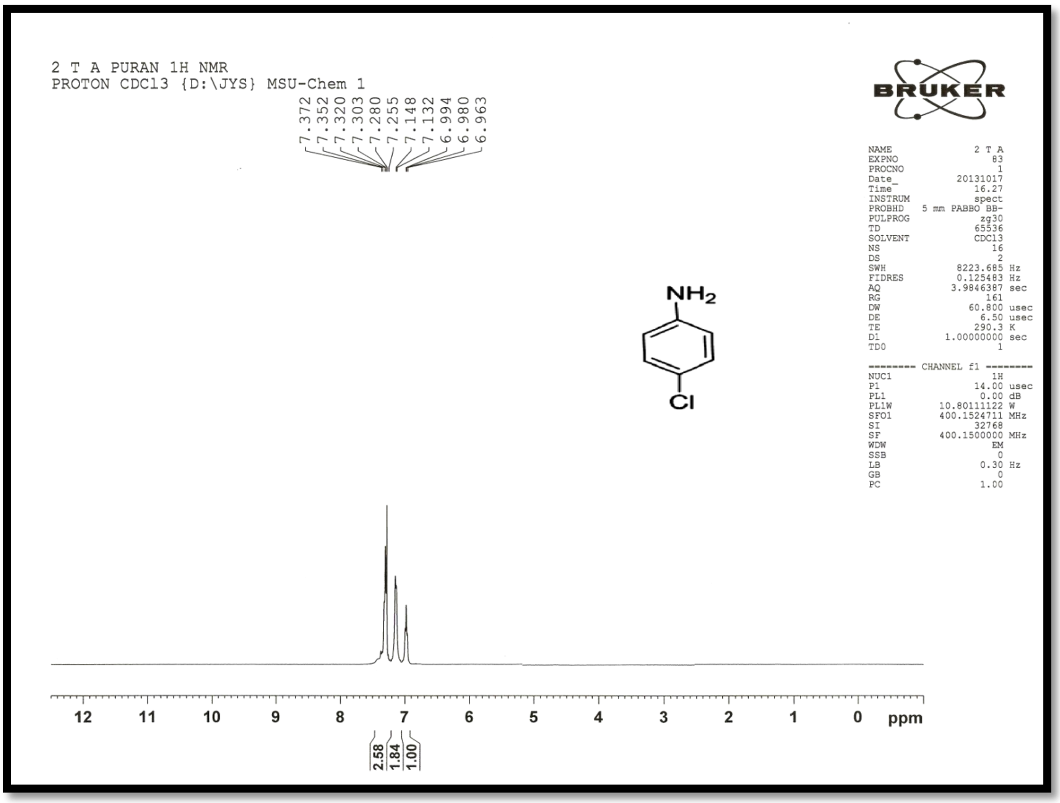

Figure S16 ^{1}HNMR spectra of *p*-Chloroaniline ($CDCl_3$, Table-3.6, Entry-16)

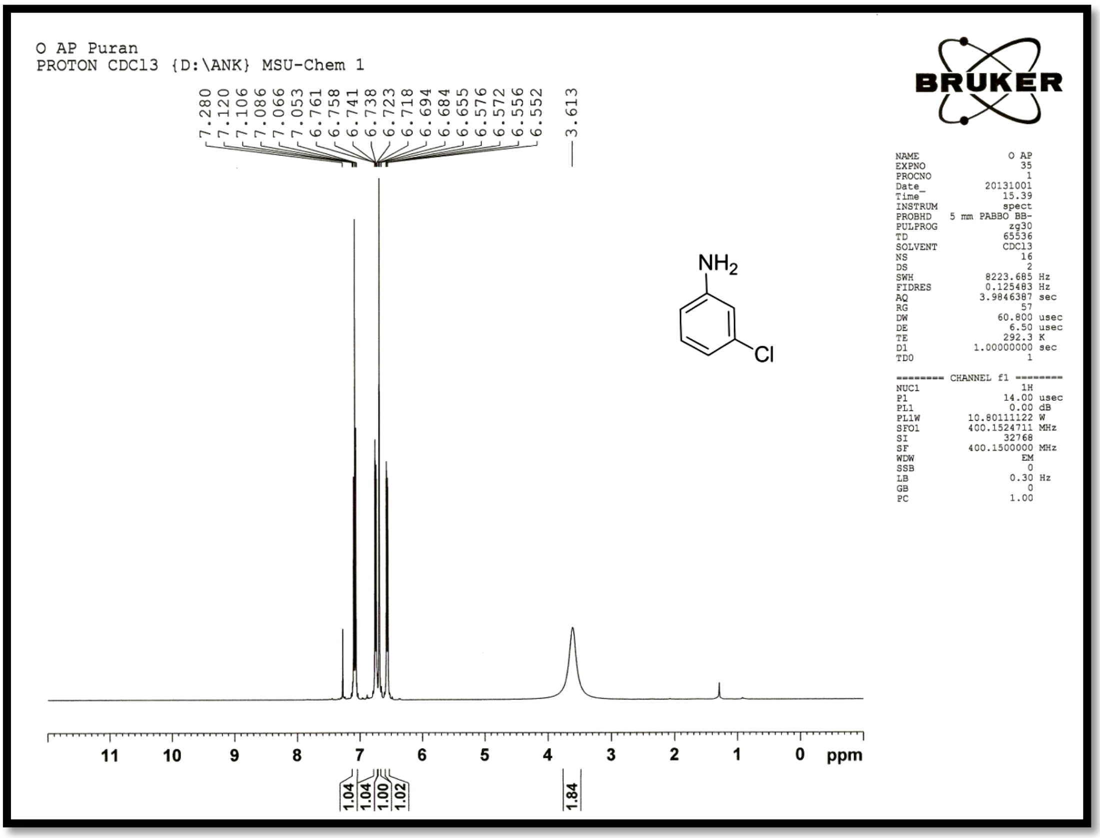

Figure S17 ^{1}HNMR spectra of *m*-Chloroaniline (CDCl$_3$, Table-3.6, Entry-17)

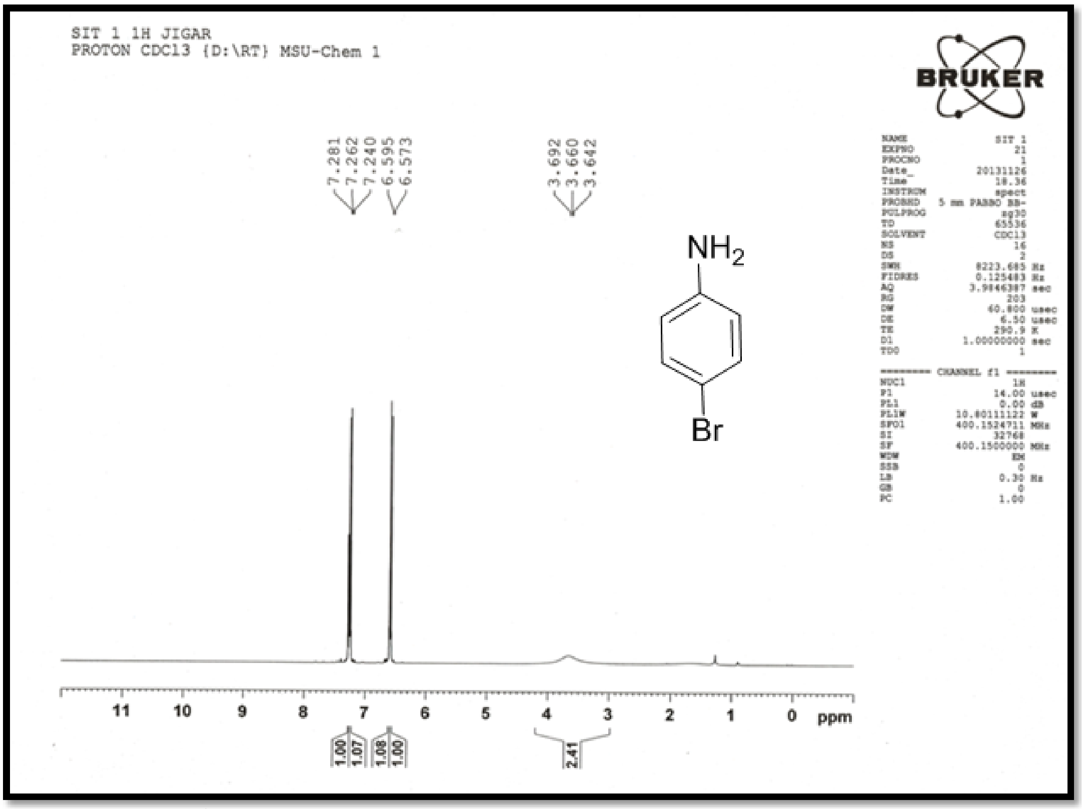

Figure S18 ^{1}HNMR spectra of *p*-Bromoaniline (CDCl$_3$, Table-3.6, Entry-18)

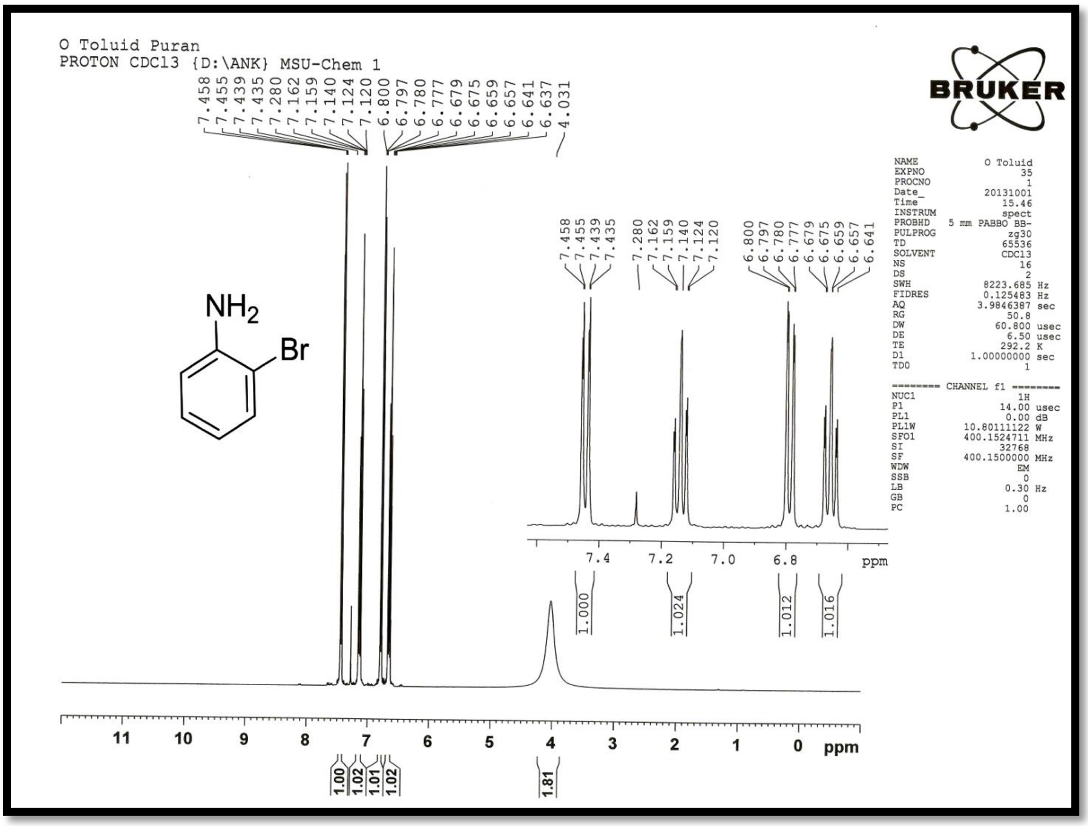

Figure S19 ^{1}HNMR spectra of *o*-Bromoaniline ($CDCl_3$, Table-3.6, Entry-19)

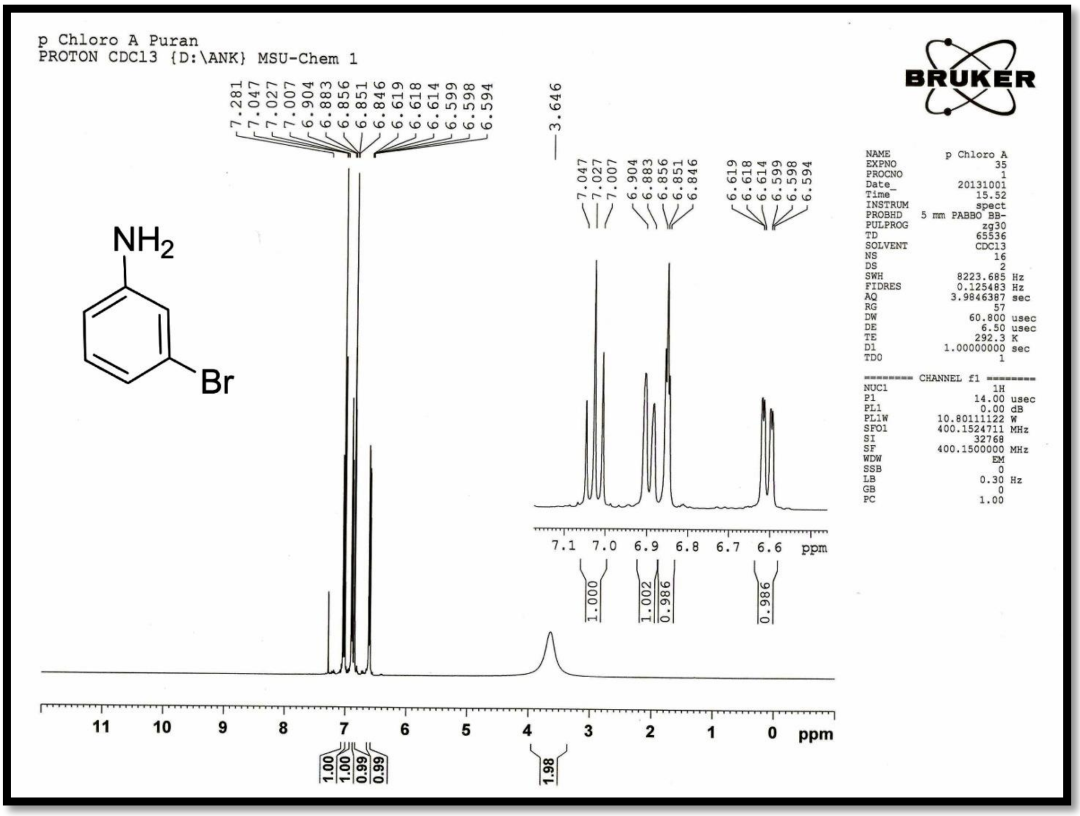

Figure S20 ^{1}HNMR spectra of *m*-Bromoaniline ($CDCl_3$, Table-3.6, Entry-20)

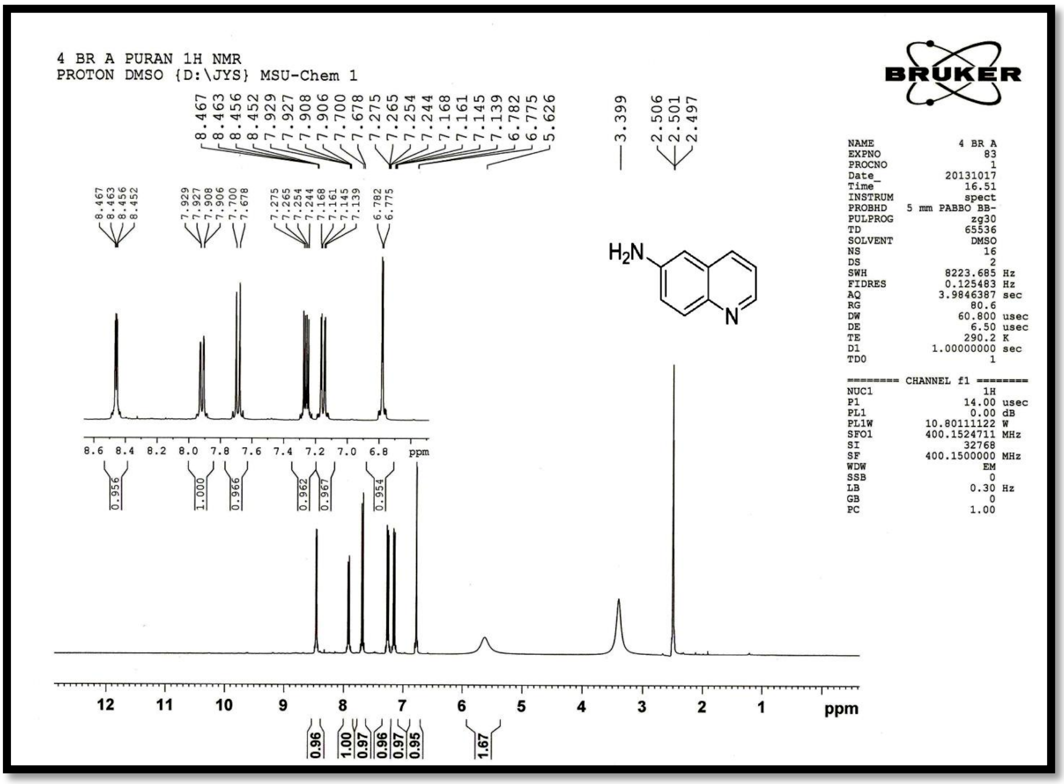

```
4 BR A PURAN 1H NMR
PROTON DMSO {D:\JYS} MSU-Chem 1
```

```
NAME                4 BR A
EXPNO                   83
PROCNO                   1
Date_             20131017
Time                 16.51
INSTRUM              spect
PROBHD   5 mm PABBO BB-
PULPROG               zg30
TD                   65536
SOLVENT               DMSO
NS                      16
DS                       2
SWH               8223.685 Hz
FIDRES            0.125483 Hz
AQ               3.9846387 sec
RG                    80.6
DW                  60.800 usec
DE                    6.50 usec
TE                   290.2 K
D1              1.00000000 sec
TD0                      1

======== CHANNEL f1 ========
NUC1                    1H
P1                   14.00 usec
PL1                   0.00 dB
PL1W           10.80111122 W
SFO1           400.1524711 MHz
SI                   32768
SF             400.1500000 MHz
WDW                     EM
SSB                      0
LB                    0.30 Hz
GB                       0
PC                    1.00
```

Figure S21 ^{1}HNMR spectra of Quinolin-6-amine (DMSO, Table-3.6, Entry-21)

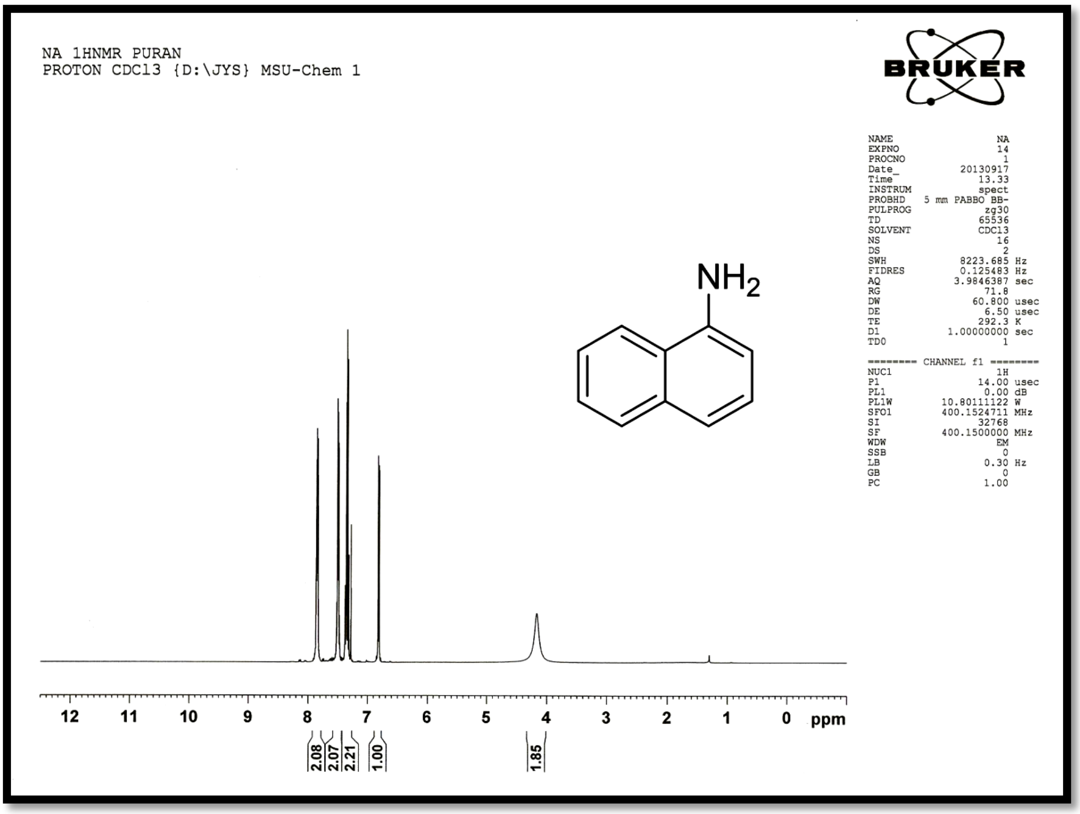

```
NA 1HNMR PURAN
PROTON CDCl3 {D:\JYS} MSU-Chem 1
```

```
NAME                    NA
EXPNO                   14
PROCNO                   1
Date_             20130917
Time                 13.33
INSTRUM              spect
PROBHD   5 mm PABBO BB-
PULPROG               zg30
TD                   65536
SOLVENT              CDCl3
NS                      16
DS                       2
SWH               8223.685 Hz
FIDRES            0.125483 Hz
AQ               3.9846387 sec
RG                    71.8
DW                  60.800 usec
DE                    6.50 usec
TE                   292.3 K
D1              1.00000000 sec
TD0                      1

======== CHANNEL f1 ========
NUC1                    1H
P1                   14.00 usec
PL1                   0.00 dB
PL1W           10.80111122 W
SFO1           400.1524711 MHz
SI                   32768
SF             400.1500000 MHz
WDW                     EM
SSB                      0
LB                    0.30 Hz
GB                       0
PC                    1.00
```

Figure S22 ^{1}HNMR spectra of 1-Naphthylamine ($CDCl_3$, Table-3.6, Entry-22)

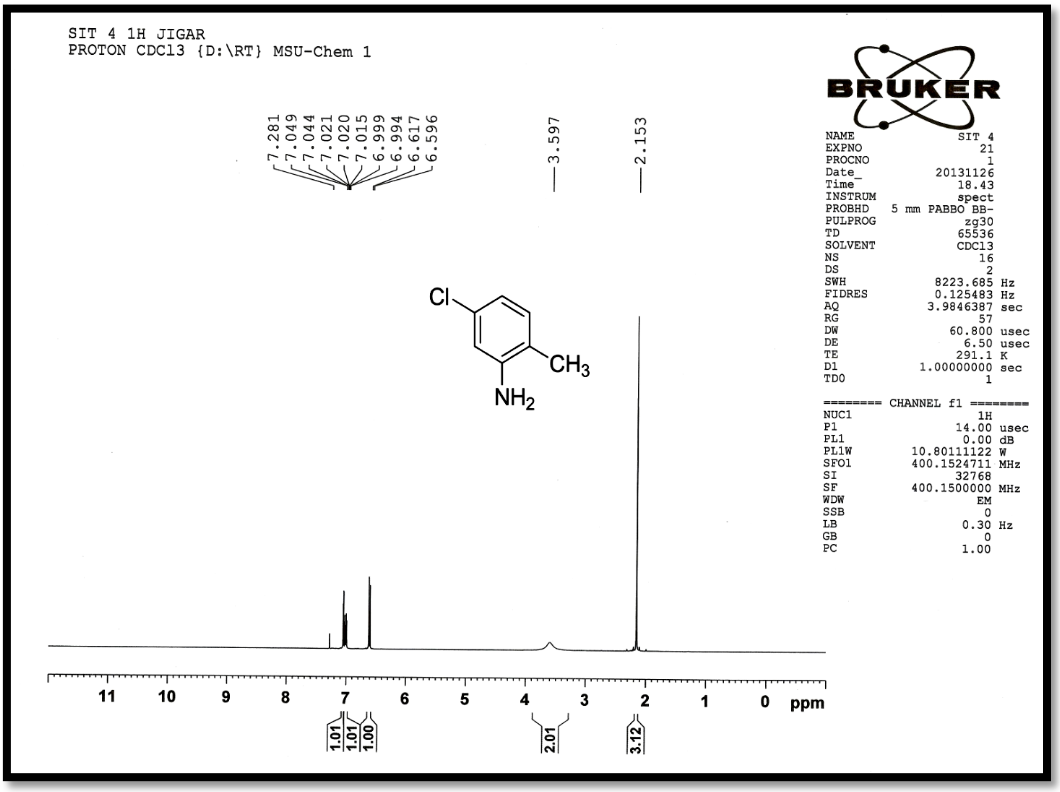

Figure S23 ^{1}HNMR spectra of 2-Amino-5-Chlorotoluene ($CDCl_3$, Table-3.6, Entry-23)

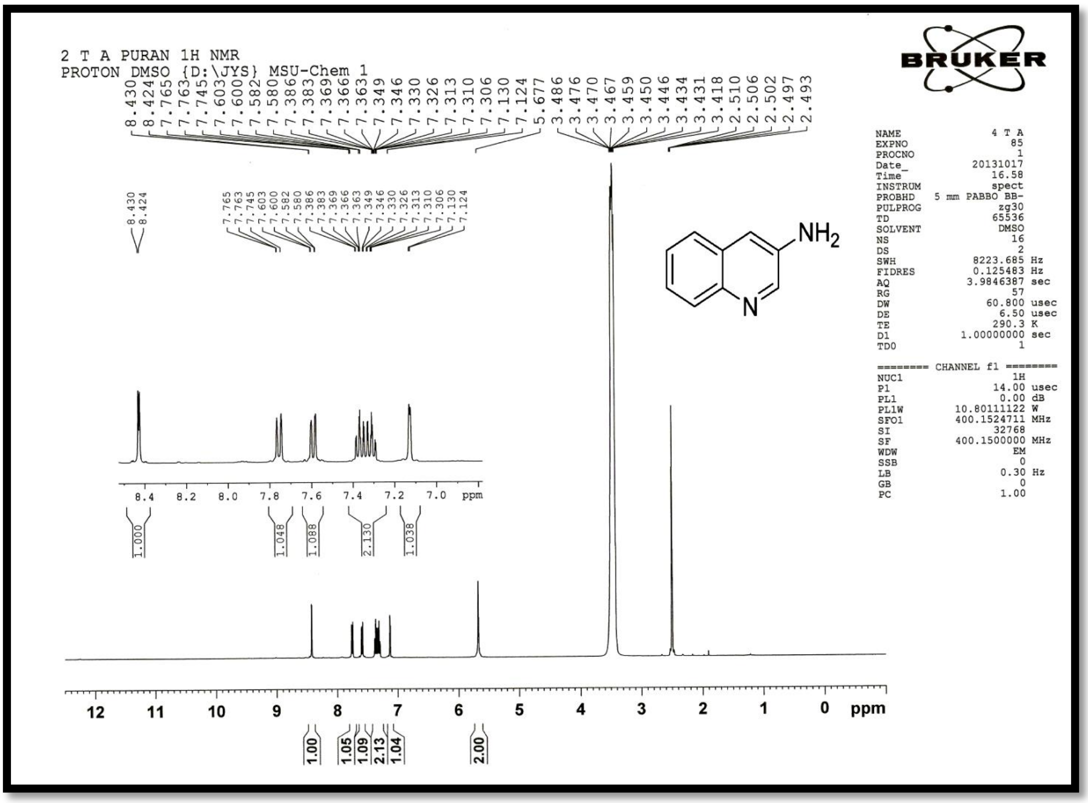

Figure S24 ^{1}HNMR spectra of Quinolin-3-amine (DMSO, Table-3.6, Entry-24)

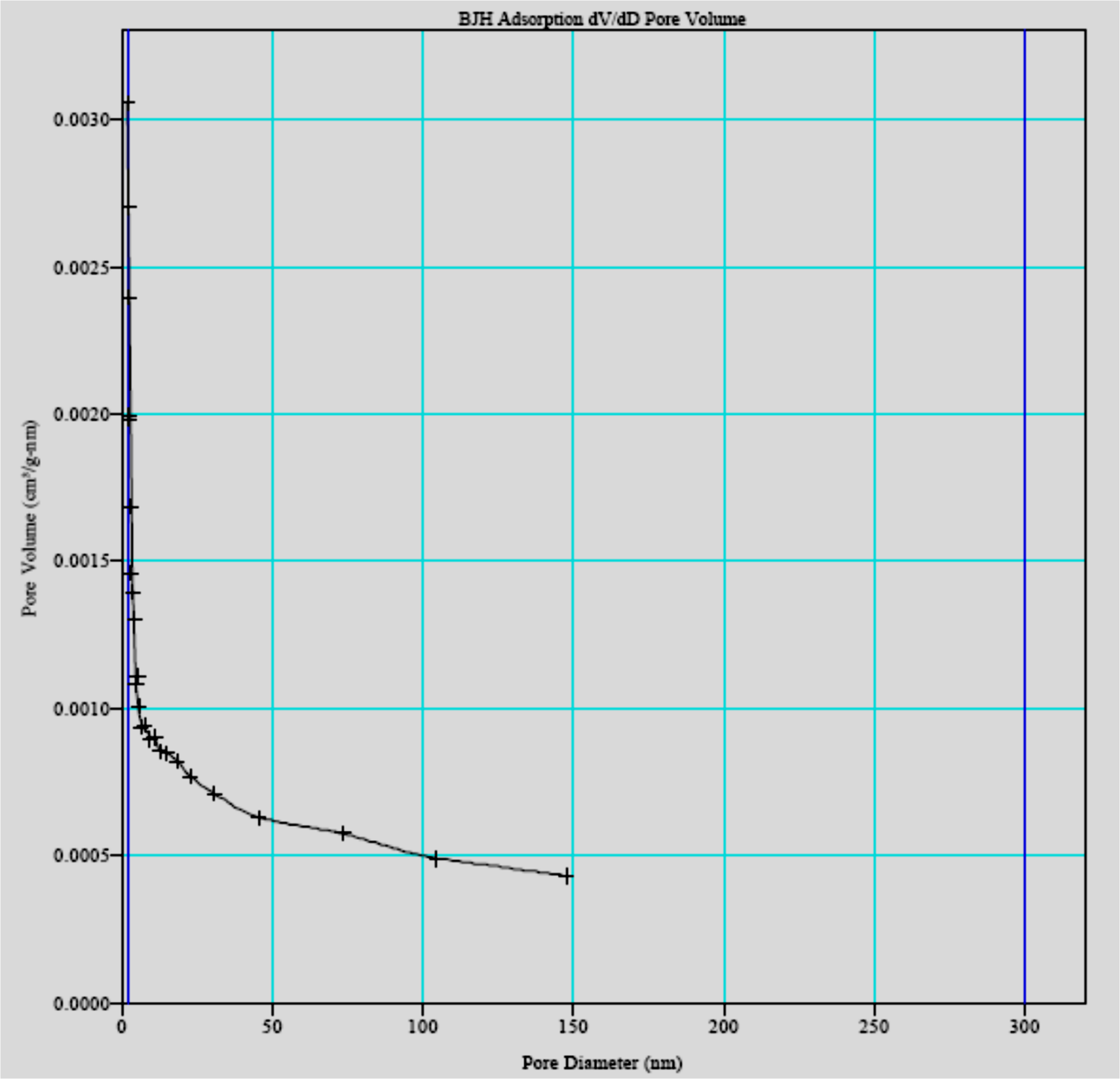

Figure S25 BJH Adsorption dV/dD Pore Volume for IO@NiNPs

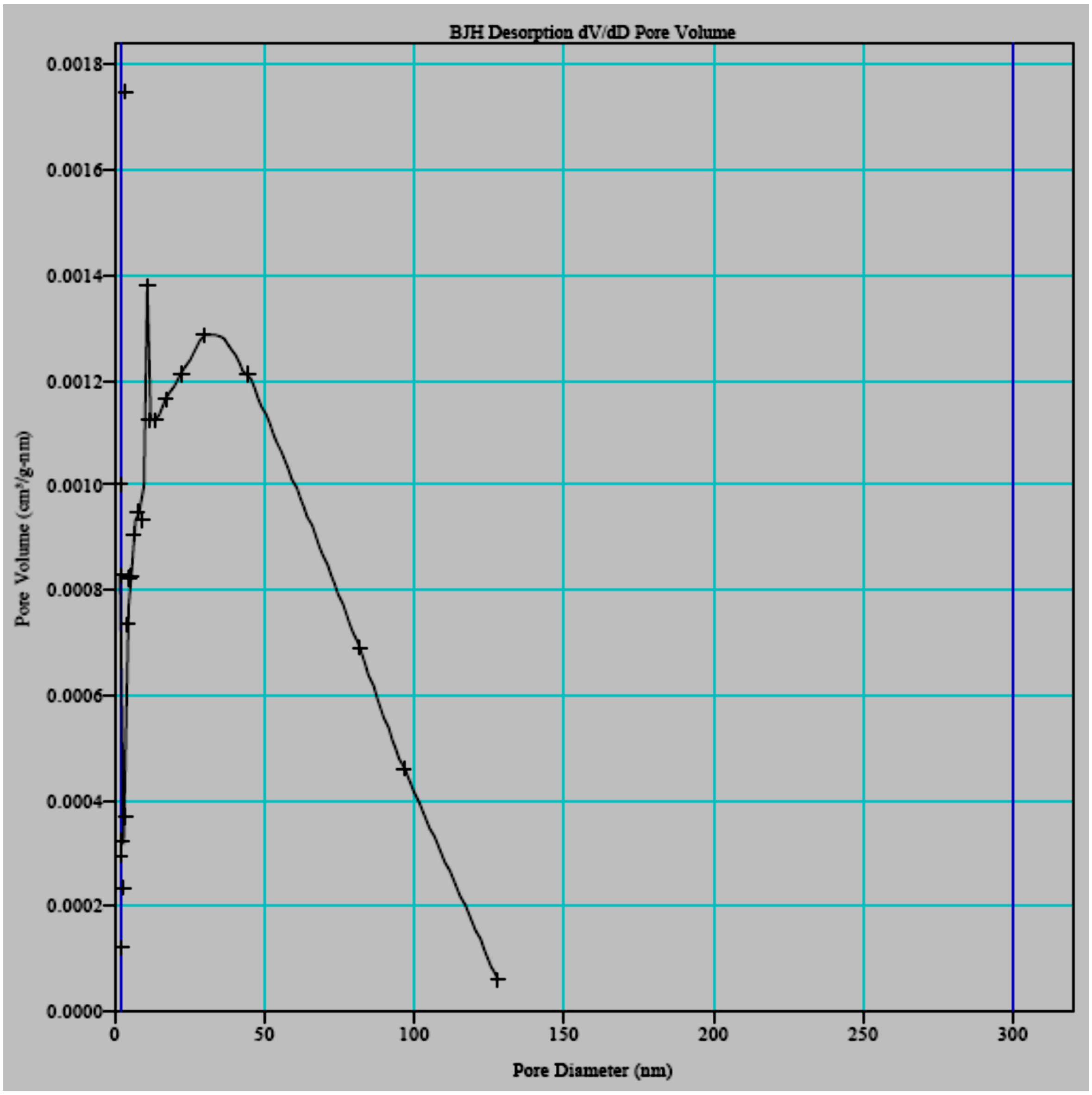

Figure S26 BJH Desorption dV/dD Pore Volume for IO@NiNPs

Chapter-3

Part-2

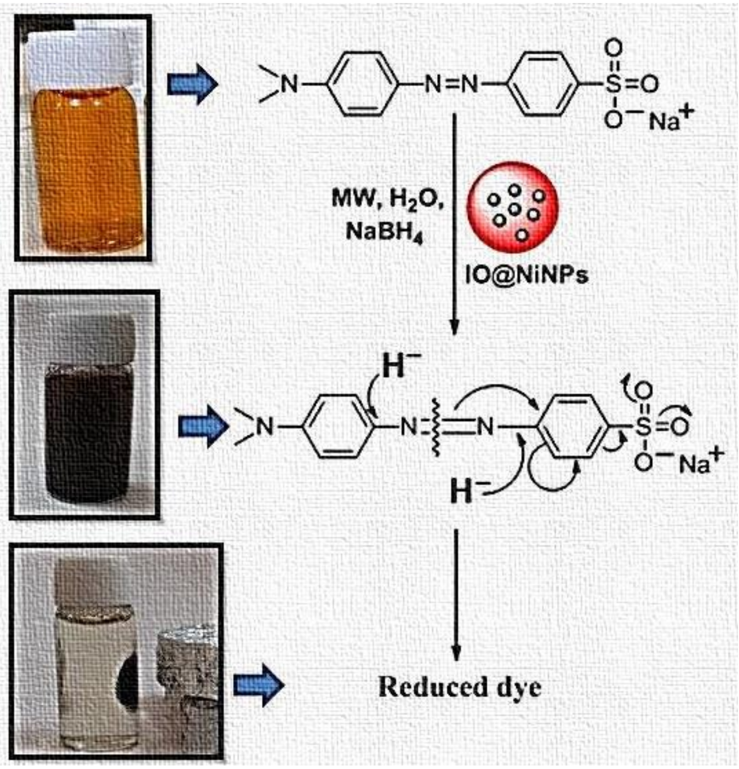

Efficient catalytic reduction of azo dyes using magnetically separable core/shell Iron oxide@Nickel nanoparticles

3.2.1 Introduction

The Earth's water resources are being increasingly contaminated due to the coloured dye effluents. Nowadays, the pollution of water resources by azo dyes from the textile industry has become a serious environmental pollution and health hazards, which is attracting greater attention.[1-3] The efficient reduction of dyes has become a challenging task for chemists.[4] Most of the dyes used throughout the textile industry are also azo dyes.[5,6] A wide range of different methodologies is being adopted to treat dye effluents, which include photocatalysis,[7] biological reduction,[8] physico-chemical methods (adsorption tactics),[9] and Fenton-like reactions.[10] The systematic reduction of azo dyes are said to be achieved using photocatalysis, where the most employed photocatalytic material, $TiO_{2,}$ is active only in the ultraviolet range. Lots of efforts have been focused towards developing visible light-active photocatalysts. Yet, their practical applications are limited since the quantum yield is not satisfactory.[11, 12] Biological treatment is time consuming with poor efficiency.[13] Among physico-chemical methods, adsorption of dyes on activated carbon[14] or magnetic nanoparticles (MNPs)[15] is the most common. Some iron oxides and their composite nanostructures have proved effective materials for dye removal by adsorption.[16-21] Although, this method is claimed to be a relatively cheap; however, it only results in the transfer of pollutants from waste water to solid wastes (secondary pollution). The regeneration is generally not so effective and causes high operational cost.[14] In the case of Fenton like reactions, the subsequent treatment of ferrous slurry and the requirement of H_2O_2 led to complexity. Therefore new treatment methods are required for the removal of toxic dyes, or converting them to harmless products in water.

Extensive research has been carried out to explore metal nanoparticles (NPs), especially as they exhibit enhanced catalytic activity due to their large surface to volume ratio.[22] Here we assess the potential of magnetic iron oxide synthesized from iron ore tailings (IOTs) as a template for synthesis of magnetically separable nickel nanoparticle (NiNPs).

In literature, a few procedures involving the expensive metal NPs such as Pd,[23] Ag,[24, 25] as well as Au NPs[25, 26] have been demonstrated for the reduction of azo dyes. Our ultimate goal in this work was to obtain a suitable low cost, easily recoverable material to act as a catalyst in the reduction of azo dyes.

In the earlier chapters, we have investigated the use of NiNPs as catalysts for transesterification as well as for azo dye reduction[27, 28]

In previous chapter we reported synthesis and catalytic application of IO@Ni core-shell nanoparticles for reduction of nitroaromatics.[28b] In this chapter, we report higher loading of nickel (≈ 9%) on iron oxide and it was used as nanocatalyst for the microwave (MW) assisted azo dye reduction. The IO@NiNPs exhibit greater activity and recyclability than starch capped nickel nanoparticles, which were used in our previous study.[28] Initially methyl orange (MO) was used as the model system to simplify the analysis and to accelerate the screening speed. Consequently the optimized conditions were used for the reduction of various azo dyes as well as for a mixture of dyes. Liquid chromatogram-mass spectrometer (LCMS) and UV-*vis* spectrophotometer were used as evidences to demonstrate reduction or reduction of dyes.

3.2.2 Experimental

3.2.2.1 Materials

Azo dyes, $NaBH_4$, $Ni(CH_3COO)_2.4H_2O$, liquid ammonia, and starch were purchased from Merck Mumbai, India. All the solutions were prepared using double-distilled and demineralized water. Iron ore tailings, collected from iron industries (Silverline Exporters Private Limited, Gujarat, India), and were screened for their iron contents and one sample with relatively high iron content (~36.04%) was used as one of the starting materials.

3.2.2.2 Synthesis of Iron oxide@Nickel Nanoparticles (IO@NiNPs) with 10% loading of Nickel.

A mixture of iron oxide was synthesized from the waste iron ore tailings (IOTs) via acid leaching and precipitation through a sequential precipitation method, following a reported procedure.[29] Further details on the synthesis of iron oxide are discussed elsewhere.[29-31] These results indicate that IOTs could be used as a source material for the production of iron oxide, with comparable quality to those produced using analytical-grade reagents.

IO@Ni core@shell NPs were synthesized by reduction of Ni^{+2} ions in the presence of iron oxide. To deposit NiNPs, 100 mg of iron oxide was dispersed in 10 mL of deionized water and sonicated for 30 min. Nickel Nanoparticles were synthesized on magnetic core through a wet chemical reduction process by an earlier reported method with minor modifications.[28] $Ni(CH_3COO)_2.4H_2O$ and soluble starch were used as metal salt precursor and stabilizing agent respectively. $NaBH_4$ (10%, W/V) was used as reducing agent and liquid ammonia as complexing agent. Nickel acetate solution (10 mL of 0.1 M) was added to 10 mL of starch solution (1%, W/V) and stirred on a magnetic stirrer at RT. The pH of the solution was adjusted to 10 with liquid ammonia (3 mL) and reduction was carried out with 1 mL of $NaBH_4$ solution. For further stirring for 10 min The IO were gradually coated by NiNPs when the color of the solution changed from red to black. The resultant IO@NiNPs were collected by external magnet and washed with deionized water several times to remove unreacted materials. Finally NPs were washed with acetone, and dried at 60 °C under vacuum.

3.2.2.3 Catalytic reduction of azo dyes

Experiments were carried out by using four different kinds of azo dyes. The dyes used were Methyl Orange (MO), Orange II (OR-II), Methyl Red (MR) and Erichrome Black-T (EBT). For each microwave (MW) assisted reduction experiment 12 mg of IO@NiNPs (0.01 M of NiNPs) was taken into 50 mL stoppered borosilicate Erlenmeyer flasks together with 5 mL of an aqueous solution with 0.075mM of azo dyes and 0.2 mL $NaBH_4$ (30 mM). Analogous experiments were performed with only IO@NiNPs, $NaBH_4$ and MW irradiation. The reduction of each dye was measured by its absorbance at λ_{max} using UV–vis spectrophotometer. Reduction of a mixture of dyes was also attempted in a similar manner.

After completion of the reaction, the catalyst was separated magnetically. The product was isolated by extraction in chloroform for LCMS. All experiments have been repeated five times and the reproducibility was confirmed. The recyclability of the NPs was also surveyed. The NPs were recovered by magnet and washed with water, followed by methanol. They were dried at 60 ºC under vacuum and used for the next cycle.

3.2.2.4 Characterizations methods

The chemical analyses for major constituents in IOT, acid insoluble residue and aqueous suspension of IO@NiNPs were carried out by conventional wet chemical analysis while AAS (AA 6300: Shimadzu, Japan) or ICP-OES (Perkin Elmer, 4300) was used to analyze the constituents present in traces. Surface area and porosity of the nanocatalyst were measured by a volumetric adsorption system (Micromeritics Instrument Corporation, USA, model ASAP 2010) using N_2 adsorption/desorption isotherms at 77 K up to 1 bar. Prior to the measurements, the samples were activated (degassed) by heating at the rate of 1 K/min upto 383 K under vaccum. The temperature as well as vacuum was maintained for 7 hours prior to the measurements. The surface area was calculated by Brunauer-Emmet-Teller (BET) method while the porosity by Barrett-Joyner-Halenda (BJH) method. The powered X-ray diffraction (XRD) patterns was recorded with a PanAlytical (model; Empyrean) ‘X’PERT-PRO XRPD of Cu Kα radiation (λ= 0.15406 nm) on advance X-ray power diffractometer. Samples were prepared by pressing dried powder and patterns were collected with a scanning rate of 2°/min and 2θ ranging from 0 to 80°. High-Resolution Transmission Electron Microscopy (HR-TEM) was carried out using Jeol (Jem-2100) electron microscope operated at an acceleration voltage of 200 kV. For this purpose, dry powered sample was dispersed in methanol and ultrasonication treatment was given for 30 min. After that sample was deposited onto a carbon-coated grid at room temperature and it was allowed to air-drying (about 6 hours). Selected area electron diffraction patterns (SAED) were also investigated from the electron micrographs. FT-IR spectra were recorded as KBr pellet on the Perkin Elmer RX1 model in the range of 4000-400 cm^{-1}. Magnetic measurements were done by a vibrating sample magnetometer (EG&G Model 155 VSM) at room temperature in the range +20,000 to −20,000 G. IO@NiNPs catalyzed azo dyes reduction was monitored on PerkinElmer Lambda 35 UV–vis spectrophotometer by corresponding $\lambda_{\text{-max}}$. For reduction of azo dyes microwave (MW) oven operated in the 100% power of 1350W and frequency 2,450 MHz.

3.2.2.5 LCMS Analysis

The determination of the dye concentration and the identification of their respective byproducts were performed by an LCMS system. A Shimadzu 8030 series LCMS system was performed with a binary pump, 1100 UV-vis diode array detector, an auto sample, and a column thermostat. The LCMS system was equipped with an Enable C18G (S/N: VL06-150) column (150 mm × 4.6 mm i.d., 5μm) and coupled online to an LC/MSD Trap XCT ion-trap mass spectrometer (Shimadzu 8030). The mass spectrometer was equipped with an ESI source and operated in positive polarity. The ESI conditions were as follows: capillary voltage 3.5 kV; end plate offset -500 V; capillary exit 100 V; nebulizer pressure 40 psi; drying gas flow 10 L min^{-1}; temperature 350 °C. For the all dyes analysis, the solvents used as mobile phase where only methanol, flow rate was 0.8 mL min^{-1}, 10 μL of sample solution was injected, and the mass range was from 100 to 500 *m*/*z*.

3.2.3 Results and Discussions

3.2.3.1 Synthesis and characterizations of IO@NiNPs

The primarily constitute of IOTs are magnetite, hematite and goethite as the main iron bearing phases which is evident from X-ray diffraction (XRD) patterns (**Chapter 3**, **part 1**, **Figure 3.1**). XRD of as synthesized Iron oxide corresponds to crystalline phases. It is clear from the pattern that sample is composed of mixed phases. It is also observed that pattern is dominated by maghemite (γ-Fe_2O_3) and magnetite (Fe_3O_4) phases (**Chapter 3**, **part 1**, **Table 3.1 to 3.4**).

Template synthesis method was used for synthesis of magnetic separable core/shell nanoparticles. This approach utilizes pre-formed iron oxide of the first metal and subsequently directing the deposition of the Ni metal onto a surface site. In the present study nanosized nickel was deposited on iron oxide under sonication and using starch as capping agent. Starch capping was proved by FT-IR (**Chapter 3**, **part-1**, **Figure 3.3**).

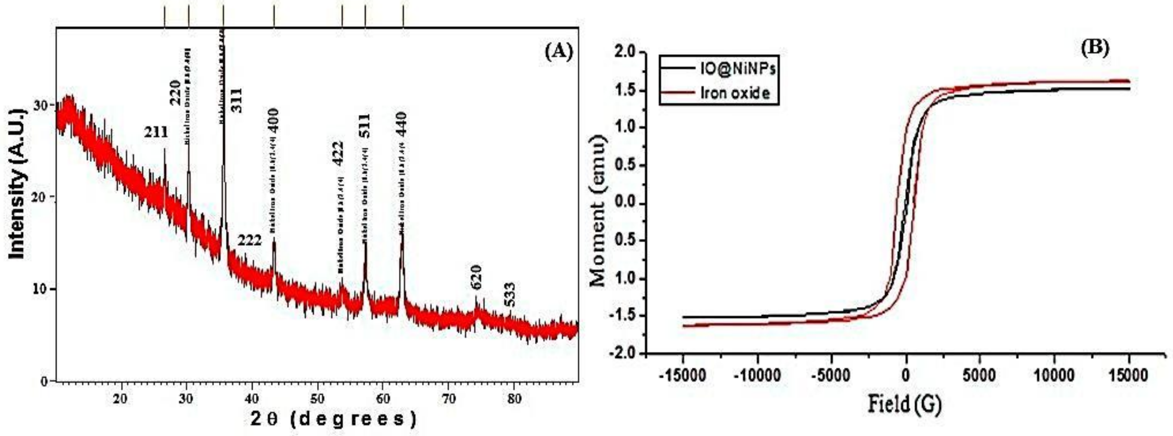

Figure 3.13 XRD pattern of (A) IO@NiNPs and (B) Magnetic hysteresis curve of as-prepared IO and IO@NiNPs

Figure 3.13A shows the XRD pattern of IO@NiNPs. The signals of Ni were not detected in the XRD spectrum of IO@NiNPs although the position and relative intensity of diffraction peaks are reasonably close to the reported pattern.[32] The XRD pattern shows that the MNPs are well-crystalline and exhibit diffraction peaks corresponding to (111), (220), (311), (400), (511) and (440) planes of the cubic crystal system. The XRD pattern indicates mixed phases of iron oxides with nickel.

The weight percentage of Ni was determined to be 9.10 % by AAS analysis and confirms the ratio 9.10:90.90 (Ni:Iron oxide). The magnetic measurements have been carried out at room temperature, and the data are shown in **Figure 3.13B**, on the as-prepared iron oxide and IO@NiNPs. From the recorded M−H loop, it is clear that both the as-prepared samples are ferromagnetic at room temperature. The magnetization of the as-prepared iron oxide was 1.5267 emu, and it decreased to a value of 1.4257 emu after coating of NiNPs. The coercivity values of the IO and IO@NiNPs were 71.64 and 60.46 G, respectively. The low magnetization value exhibited by the IO@NiNPs compared to the iron oxide one could be due to the presence of impurities/defects in the IO@NiNPs. Since the size of nanoparticles synthesized by us lies in the range of 10−60 nm, they are still ferromagnetic. The Brunauer-Emmet-Teller (BET) surface area of a magnetic IO@NiNPs sample was determined to be 16.63 m²/g. Which were indicating that, the MNPs possess the high surface area. The pore size of the MNPs was determined to be 26.37 nm by the Barrett-Joyner-Halenda (BJH) isotherms.

The High-Resolution Transmission Electron Microscopy (HR-TEM) images of IO@NiNPs show somewhat spherical morphology with some cubic partials with an average size range of 10–60 nm (**Figure 3.14A and B**). The selected area electron diffraction (SAED) pattern shown in **Figure 3.14C** corresponds to the higher order reflections of IO@NiNPs.[33] The high resolution images in **Figure 3.14D** and **E** show that nickel is deposited on the iron oxide surface. The **Figure 3.14F** shows well developed lattice fringes and the fringes extend throughout the particle confirming the monocrystalline nature of the individual particles. The distance between adjacent lattice fringes measured as 0.247 nm in **Figure 3.14F** corresponds to the 311 reflections. The HR-TEM image (**Figure 3.14**) reveals the characteristics of core-shell nanoparticles.

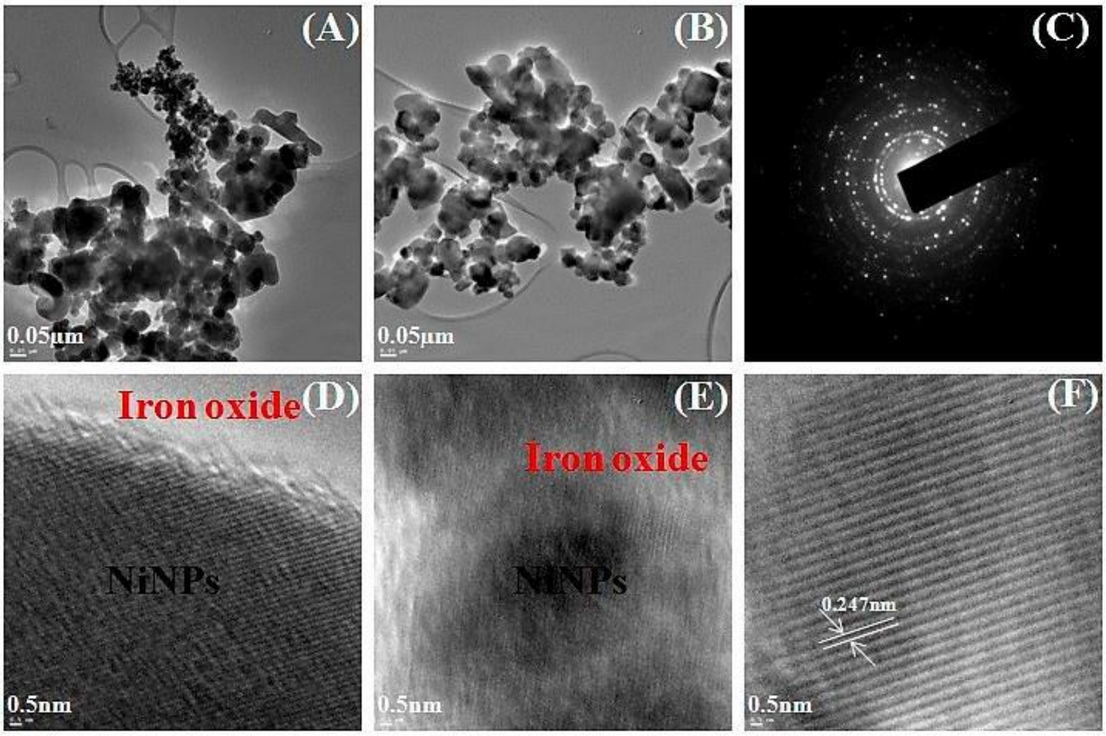

Figure 3.14 HR-TEM images of of IO@NiNPs (A) and (B) showing particle size distribution; (C) SAED pattern of IO@NiNPs and (D), (E) and (F) are resolved lattice fringes respectively.

3.2.3.2 Catalytic reduction of azo dyes

The efficacy of IO@Ni nanocatalyst towards the reduction of different organic azo dye molecules using $NaBH_4$ as a reducing agent was investigated. For Initial screening reduction of methyl orange (MO) was investigated under various reaction conditions (**Table 3.9**). The reduction reaction was carried out in the microwave (MW) irradiation and the reaction was monitored with the help of a UV-Visible spectrometer. MO was found to exhibit absorption maxima of 465 nm. Hence, the catalytic reduction of this dye was monitored by observing the change in absorbance of this peak (**Figure 3.15**).

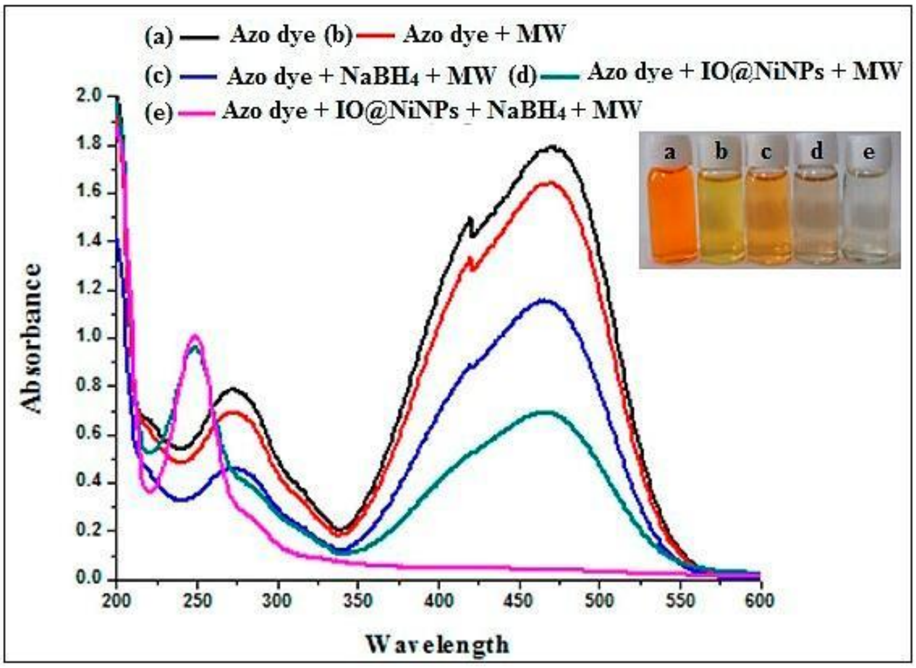

Figure 3.15 UV–Vis spectra related to experiments on reduction of MO dye under different conditions. Inset shows related digital photograph

The reduction studies were carried out in MW with different concentrations of $NaBH_4$ and IO@NiNPs in order to optimize the suitable conditions for maximum catalytic activity in **Table 3.9**. $NaBH_4$ or IO@NiNPs individually was not capable of inducing a reduction of MO in lesser quantity (**Table 3.9**, entries 1 and 2). However, the nanocatalyst alone was capable of reducing azo dye, when used in excess amount with the extend reaction time (**Table 3.9**, entries-3, 4, 5 and 6). The maximum catalytic reduction could be attained in the presence of 0.2 mL of $NaBH_4$ (30 mmol strength) and 12 mg of IO@NiNPs (**Table 3.9**, entry-8). Hence, the same concentration of $NaBH_4$ and the nanocatalyst was maintained for further investigation. On decreasing the quantity of $NaBH_4$ from 0.4 mL to 0.2 mL reaction time did not change (**Table 3.9**, entry 7 and 8). Furthermore, experiments were performed using a different mole ratio of $NaBH_4$ in standard reaction, whereas using 0.1 mL of $NaBH_4$ resulted in an increase in the reaction time (entry-9) and hence an adequate quantity of $NaBH_4$ was used in optimum reaction condition.

Variation in quantity of IO@NiNPs (**Table 3.9**, entries 10 to 13) under optimum reaction conditions showed that even 1 mg was sufficient for catalyzing the reaction under MW irradiation. But, the reaction time was increased to 1h for maximum conversion (**Table 3.9**, entry 13)., On the other hand, with 10, 8 and 4 mg of NPs, the reaction time increased to 2.4, 6 and 9 min. respectively (**Table 3.9**, entries-10, 11 and 12). Beyond 12 mg the reaction time did not change.

UV–vis spectra of Methyl orange dye in **Figure 3.15** shows that before the addition of IO@NiNPs, there was the maximum absorption band centred at 465 nm, which could be assigned to the conjugated system formed by the –N=N– bonds of MO. The colour of the dye is attributed to this maximum absorption band, which could be used to monitor the reduction reaction. $NaBH_4$ alone could not induce complete reduction of the dye in MW. But when irradiated in the presence of NPs, $NaBH_4$ led to complete reduction of the dye. The absorption band at 483 nm decreased and gradually disappeared. This could be ascribed to the loss of conjugation due to reduction of –N=N– bonds owing to electron transfer through the surface of NPs.

The enhanced reduction observed with our nanocatalysts can be attributed to the following reasons; (1) high surface area of the MNPs can adsorb azo dyes to facilitate the electron transfer between the dye and $NaBH_4$ before rapid diffusion pulls them apart,[34] (2) $NaBH_4$ as well as water are expected to act as the hydride source. (3) IO@Ni catalyst is expected to activate the azo nitrogen bond and to bind with the sulphur and oxygen atoms of the dyes as well, resulting in the weakening of the azo double bond via conjugation. (4) The hydrophilic interactions of -OH groups of starch with the azo dyes are expected to assist in bringing the dye molecules in close proximity of the catalytic sites.

Table 3.9 Optimization of reaction conditions for methyl orange (MO) reduction

Sr. No.	**Catalyst (mg)**	**$NaBH_4$ (mL)**	**Time (h\min /sec)**	**Reduction[b]**
1	None	None	2 h	None
2	,,	0.2	2 h	,,
3	40	None	5 min	Complete
4	20	,,	10 min	,,
5	15	,,	25 min	,,
6	12	,,	30 min	,,
7	,,	0.4	30 sec	,,
8[a]	**,,**	**0.2**	**,,**	**,,**
9	,,	0.1	3 min	,,
10	10	0.2	2.4 min	,,
11	8	,,	6 min	,,
12	4	,,	9 min	,,
13	1	,,	1 h	,,

Reaction condition: Methyl orange (0.075 mM), $NaBH_4$ (30 mM) and MW irradiation.

a- Optimized reaction condition b- Reaction monitored by UV-*vis* Spectroscopy (OD is ≤ 0.01).

The plausible mechanism for the reduction of MO has been presented in **Scheme 3.4**. The reduction was supported by LCMS analysis. The molecular ion peak of the dye was missing in the spectra. Instead a number of peaks of various fragments were obtained, which further supported the reduction of the dye.

The fact that nanocatalyst alone was capable of catalysing the reaction at higher concentration was interesting and means that the use of $NaBH_4$ could be eliminated. It is reported in the literature[35] metal nanoparticles, being more reactive than bulk and will coordinate better with H_2O. Due to such coordination hydrogen in water, which is normally electrophilic in nature will now attain weak hydride character. This mild hydride may be ideal as a target specific reducing agent towards an electron deficient azo compound.

After optimization of the reaction conditions (**Table 3.9**), the catalytic activity of magnetic IO@Ni core-shell NPs, were further explored with other azo dyes. Orange-II (OR-II), Methyl red (MR), Erichrome black-T (EBT) and mixture of given azo dyes were used for testing the catalytic activity of our nanocatalyst. The reduction reaction was carried out in a similar manner and the reaction was monitored with the help of a UV-Visible spectrometer (**Figure 3.16**). MO, OR-II, MR, EBT and mixture of dyes (MD) were found to exhibit absorption maxima of 465, 483, 427, 540 and 456 nm, respectively, and hence the catalytic reduction of these dyes was monitored by observing the change in the absorbance of these peaks (**Table 3.10**). Similar to the methyl orange after reduction of other azo dyes we did not find any molecular ion peak in LCMS analysis.

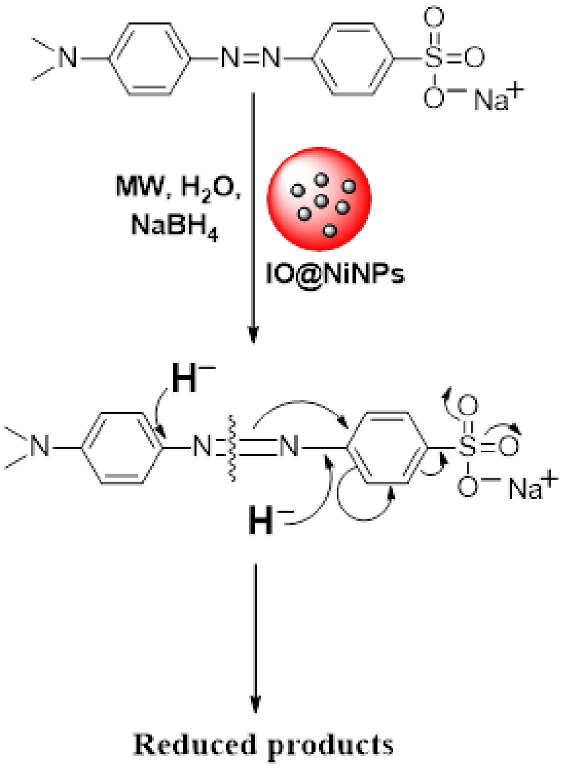

Scheme 3.4 Schematic representation of IO@NiNPs catalysed methyl orange reduction by water and $NaBH_4$.

Table 3.10 Name, corresponding λ_{max} (nm), reduction time and structure of dyes

Name of dye	λ_{max} (nm)	Reduction Time (sec.)	Structure of dye
Orange-II (OR-II)	483	30	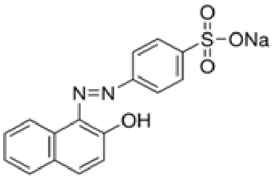
Methyl orange (MO)	465	30	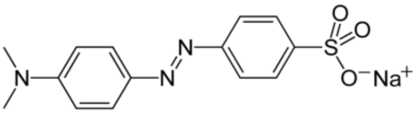
Methyl red (MR)	427	50	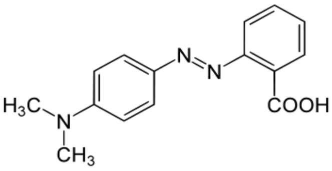
Erichrome black-T (EBT)	540	40	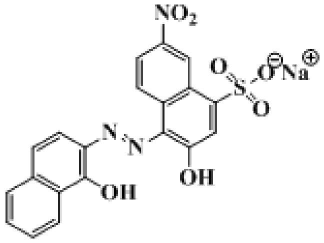
Mixture of dyes (MD)	456	40	-

Reaction conditions: IO@NiNPs- 12mg (0.01 M of NiNPs), aqueous solution of azo dyes- 5 mL (0.075 mM) and $NaBH_4$-0.2 mL (30 mM) and MW.

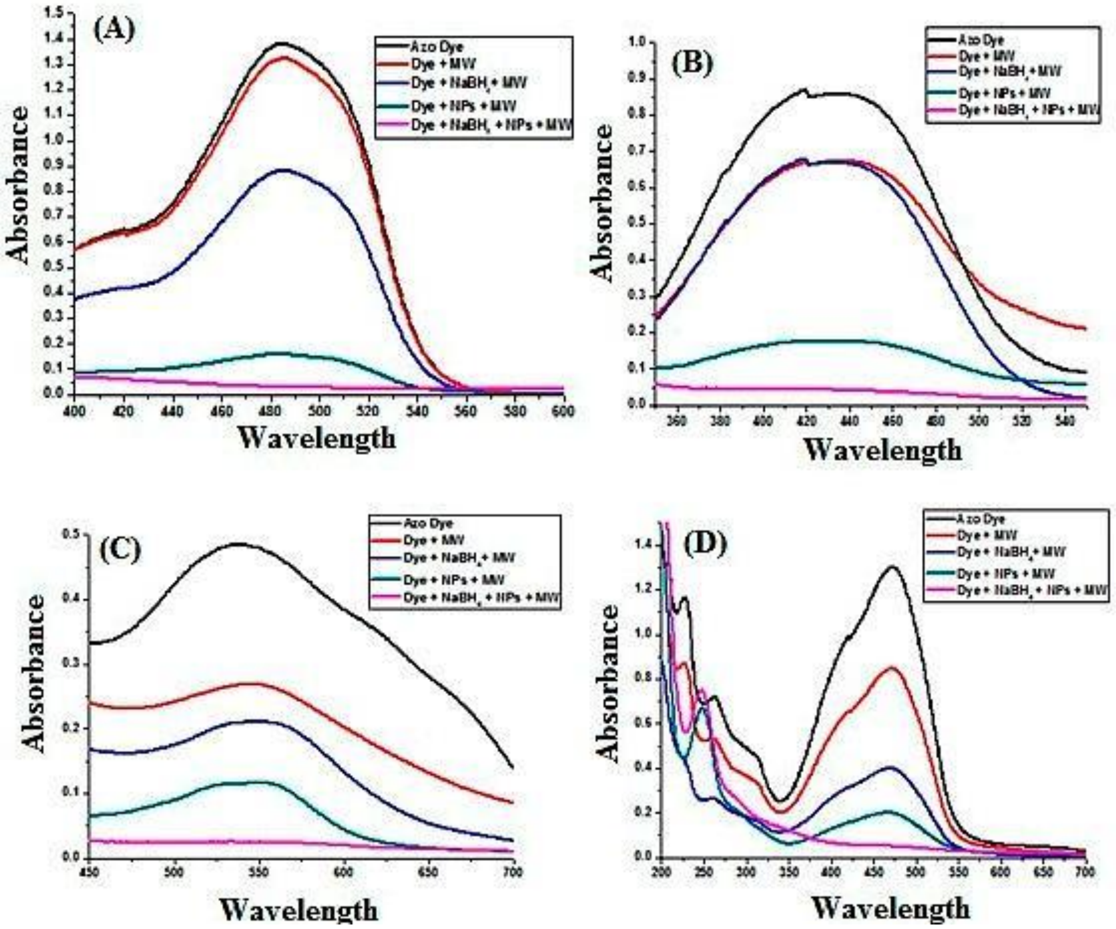

Figure 3.16 UV–Vis spectra related to experiments on reduction of (A) OR-II (B) MR (C) EBT and (D) MD dye respectively under different conditions.

The reduction was attempted in the presence of other mild reducing agents such as ascorbic acid, glucose, tri-sodium citrate. However, none of them gave satisfactory results (data not given). In order to prove that our catalyst reduces the dye rather than adsorption, FTIR spectra were recorded before and after the reaction with methyl orange (**Figure 3.17**). No significant peaks corresponding to dyes could be detected which rules out the possibility of dye adsorption under the present conditions.

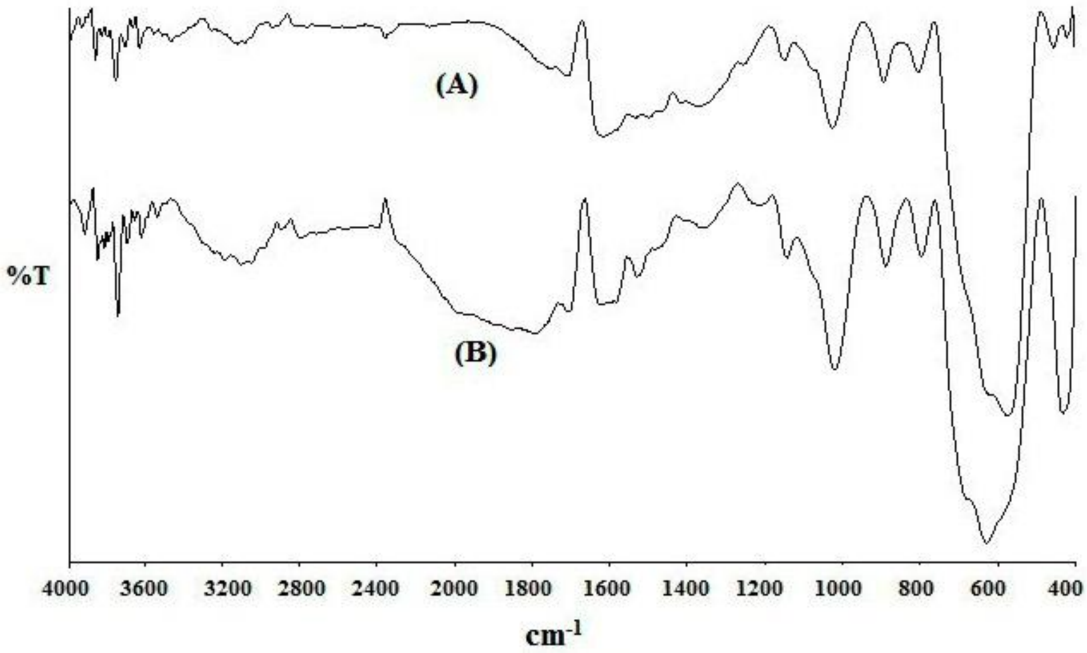

Figure 3.17 FT-IR spectra of IO@NiNPs (A) after and (B) before reduction of Methyl Orange (MO) after 1st run

3.2.3.3 Recycling of IO@NiNPs

The IO@Ni core-shell NPs were recovered by separation using an external magnet (**Figure-3.18A; a and b**) with negligible loss. Recycling experiments carried out under optimized conditions of MO showed interesting results.

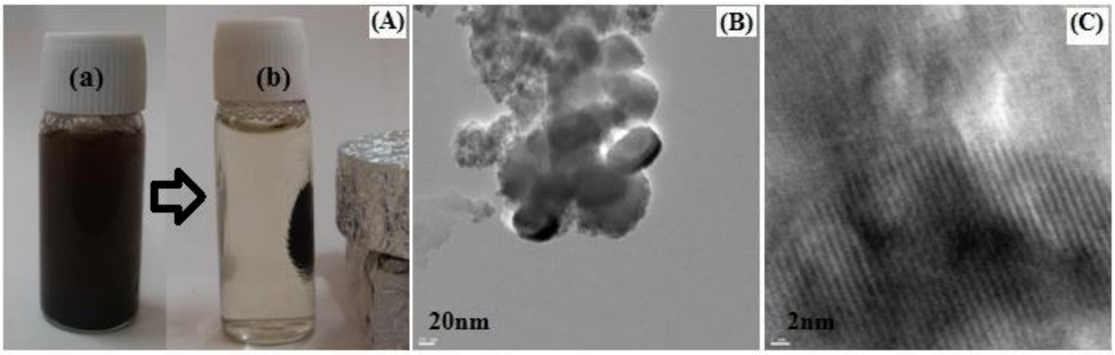

Figure 3.18 (A) Reaction mixture of MO dye (a) before and (b) after magnetic separation by simple magnet; HR-TEM of reused magnetic IO@NiNPs at different magnifications (B) 20 nm and (C) 2 nm (lattice fringes).

Table 3.11 Recycling experiments of reduction of the MO azo dye by IO@NiNPs in MW

Cycle	1	2	3	4	5	6	7
Time (Sec.)	30	30	32	50	70	120	600

It was observed that the NPs could be reused directly without further purification for 7 consecutive runs as can be seen in **Table 3.11**. Up to 3 cycles there was no loss in activity. After that, however, the reaction time increased with each successive recycling experiment reaching from 30 sec to 10 min finally. This may be due to gradual loss of the catalytic activity of the nanocatalyst with the number of runs which may be due to various reasons. One of the reasons may be surface modification due to deposition of matter during the reaction.[36,37] The HR-TEM images of the nanocatalyst recorded after the 7th run displays an agglomeration of MNPs due to deposited matter (**Figure 3.18B**). The image in **Figure 3.18C** shows that lattice fringes were damaged by deposited matter throughout the particle. Nevertheless, the reaction does proceed to completion at the same temperature at the end of 7th cycles giving the same result. Further the reused nanocatalyst was also characterized by atomic absorption spectrophotometer (AAS). Negligible leaching of nickel as ions was revealed which confirmed the stability of the catalyst. High recyclability and stability of IO@NiNPs can be attributed to the presence of starch coating which makes the NPs stable in water and air and maintains their metallic state.[38, 39] This eventually increases their utility and enhances recycling efficiency. Thus the metal surface, capping agent and $NaBH_4$ simultaneously make the IO@NiNPs system an effective catalyst.

3.2.4 Conclusion

The feasibility of using IO@Ni core-shell nanocatalyst and its possible application in the azo dye reduction has been demonstrated. The nanocatalyst proved to be highly efficient for azo dye reduction using environment friendly microwave irradiation. The IO@NiNPs catalyst could be reused for seven cycles, without any significant loss in catalytic activity. The catalyst was broadly applied to diverse azo dyes as well as for a mixture of dyes.

3.2.5 References

1. P. G. Rieger, H. M. Meir, M. Gerle, U. Vogt, T. Groth and H. J. Knackmuss, *J. Biotechnol*., 2002, **94 ,** 101.
2. C. Hu, X. X. Hu, L. S. Wang, J. H. Qu and A. M. Wang, *Environ. Sci. Technol.*, 2006, **40**, 7903.
3. M. Janus and A. W. Morawski, *Appl. Catal. B*, 2007, **75**, 118.
4. H. Zhang, D. Chen, L. V. Xiaojun, Y. Wang, H. Chang and J. Li, *Environ. Sci. Technol.*, 2010, **44**, 1107.
5. T. D. Nguyen, N. H. Phan, M. H. Do and K. T. Ngo, *J. Hazard. Mater*., 2011, **185**, 653.
6. R. Maas and S. Chaudhari, *Process Biochem*, 2005, **40**, 699.
7. J. Lee, H. S. Shim, M. Lee, J. K. Song and D. Lee, *J. Phys. Chem. Lett*., 2011, **2**, 2840.
8. F. J. Cervantes, A. G. Espinosa, M. A. Moreno-Reynosa and J. R. Rangel-Mendez, Environ. Sci. Technol., 2010, **44,** 1747.
9. J. Pengfei, J. Zhang, F. Chen and M. Anpo, *Appl. Catal. B*, 2009, **85**, 148.
10. J. Fernandez, J. Bandara, A. Lopez, P. Buffat and J. Kiwi, *Langmuir,* 1999, **15**, 185.
11. M. Parida and B. Nanda, *Dalton Trans*., 2011, **40**, 7348.
12. J. Zhang, Z. Xiong and X. S. Zhao, *J. Mater. Chem.*, 2011, **21**, 3634.
13. D. Brown, H. R. Hitz and L. Schefer, *Chemosphere*, 1981, **10**, 245.
14. G. M. Walker and L. R. Weatherley, *Water Research*, 1999, **33,** 1895.
15. L. Wang, J. Li, Z. Wang, L. Zhao and Q. Jianga, *Dalton Trans.*, 2013, **42**, 2572.
16. C. Wang, C. Feng, Y. J. Gao, X. X. Ma, Q. H. Wu and Z. Wang, *Chem. Eng. J*., 2011, **173**, 92.
17. H. M. Sun, L. Y. Cao and L. H. Lu, *Nano Res*., 2011, **4,** 550.
18. L. H. Ai, C. Y. Zhang and Z. L. Chen, *J. Hazard. Mater*., 2011, **192**, 1515.
19. G. S. Zhang, J. H. Qu, H. J. Liu, A. T. Cooper and R. C. Wu, *Chemosphere*, 2007, **68**, 1058.
20. X. M. Liang and L. J. Zhao, RSC Adv., 2012, **2**, 5485.
21. L. X. Wang, J. C. Li, Y. Q. Wang, L. J. Zhao and Q. Jiang, *Chem. Eng. J* , 2012, **181–182**, 72.

22. N. Yan, C. Xiao and Y. Kou, *Chem. Rev.*, 2010, **254**, 1179.

23. L. Xu, X-C. Wu and J-J Zhu, *Nanotechnology* , 2008, **19,** 305603.

24. V. S. Lebedeva, A. G. Vitukhnovskya, A. Yoshidac, N. Kometanic and Y. Yonezawac, *Coll Surf A*, 2008, **326**, 204.

25. R. Rajesh, S. S. Kumar and R. Venkatesan, *New J. Chem.*, 2014, **38**, 1551.

26. T. S Rezende, G. R. S. Andrade, L. S .Barreto, N. B. CostaJr, I. F. Gimenez and L. E. Almeida, *Mater Lett*, 2010, **64**, 882.

27. P. S Rathore, J. Advani, S. Rathore and S. Thakore, *J Mol Catal A: Chemi*, 2013, **377**, 129.

28. (a) P. S Rathore, R. Patidar, S. Rathore and S. Thakore, *Catal Lett*, 2013, **144**, 439; (b) P. S. Rathore, J. Advani, T. Shripathi and S. Thakore, *Catal. Sci. Technol.*, 2015, **5**, 286

29. V. S. Madeira,. Coal Mine Residues Recycling for the Fabrication of High Added Value Products. Ph.D. thesis. Federal University of Santa Catarina, Brazil, Portuguese, 2010.

30. S. L. F. Andersen, R. G. Flores, V. S. Madeira, H. J. José and R. F. P. M. Moreira, *Ind. Eng. Chem. Res.*, 2012, **51**, 767.

31. R. G. Flores, S. L. F. Andersen, L. K. K. Maia, H. J. José and R. F. P. M. Moreira, *J. Environ. Manage.*, 2012, **111**, 53.

32. M. B. Gawande, A. K. Rathi, P. S. Branco, I. D. Nogueira, A. Velhinho, J. J. Shrikhande, U. U. Indulkar, R. V. Jayaram, C. A. A. Ghumman, N. Bundaleski and O. M. N. D. Teodoro, *Chem. Eur. J.*, 2012, **18**, 12628.

33. D. Maiti, U. Manju, S. Velaga and P. S. Devi, *Cryst. Growth Des.*, 2013, **13**, 3637.

34. L. Wang, J. Li, Z. Wang, L. Zhao and Q. Jiang, *Dalton Trans.*, 2013, **42,** 2572.

35. R. Dey, N. Mukherjee, S. Ahammed and B. C. Ranu, *Chem. Commun.*, 2012, **48**, 7982.

36. J. J. Spivey, G. W. Roberts and B. H. Davies, Catalyst Deactivation, Elsevier, Amsterdam, 2001

37. F. Alonso, P. Riente, J. A. Sirvent and M. Yus, *Appl. Catal. A: Gen.*, 2010, **378**, 42.

38. M. Valodkar, P. S. Rathore, R. N. Jadeja, M. Thounaojam, R. V. Devkar and S. Thakore, *J. Hazar. Mater.*, 2012, **201-202**, 244.

39. J. M. Yan, X. B. Zhang, S. Han, H. Shioyama and Q. Xu, *Inorg. Chem.*, 2009, **48**, 7389.

(Spectral Data)

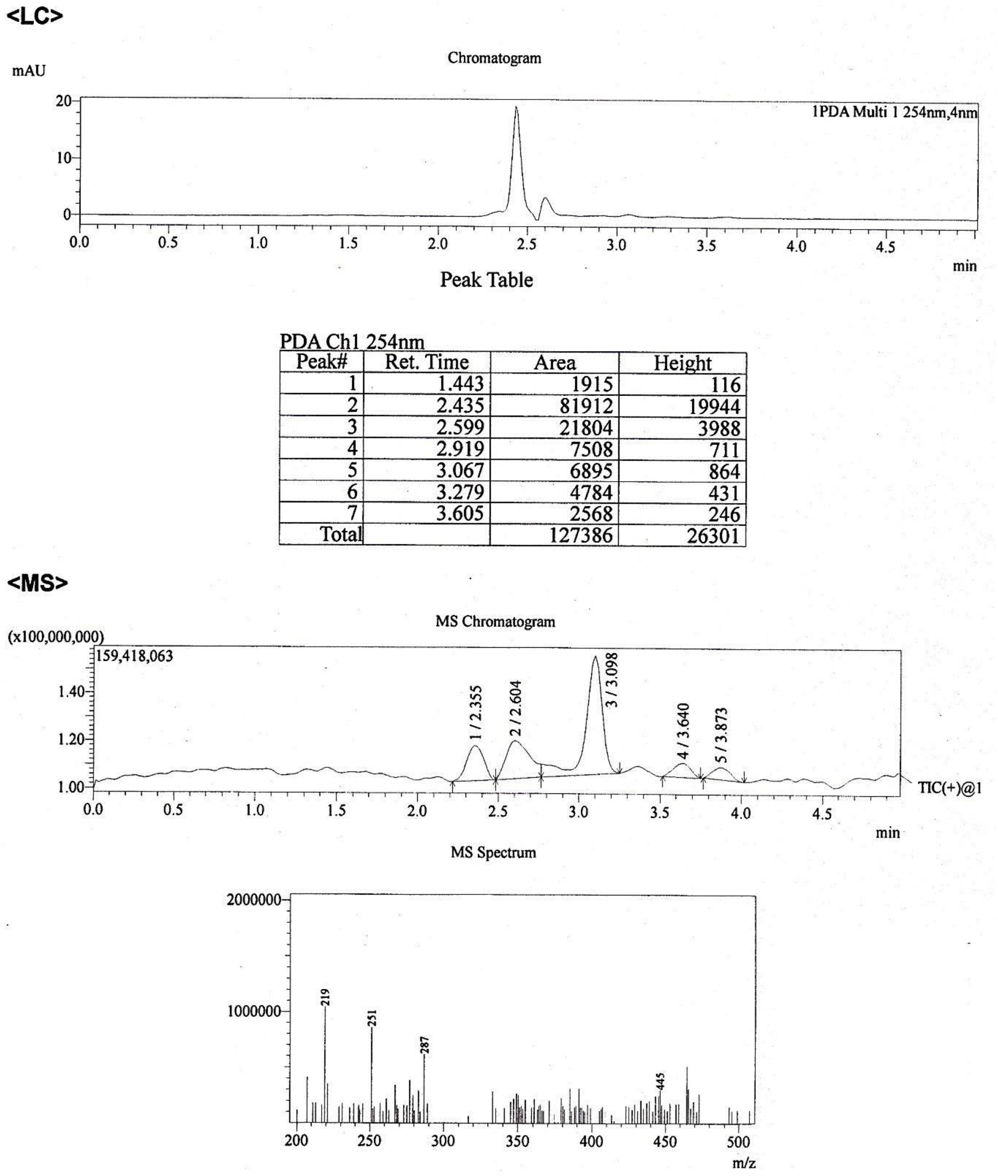

<LC>

Peak Table

PDA Ch1 254nm

Peak#	Ret. Time	Area	Height
1	1.443	1915	116
2	2.435	81912	19944
3	2.599	21804	3988
4	2.919	7508	711
5	3.067	6895	864
6	3.279	4784	431
7	3.605	2568	246
Total		127386	26301

<MS>

Figure S1 LCMS analysis of MR

<LC>

Chromatogram

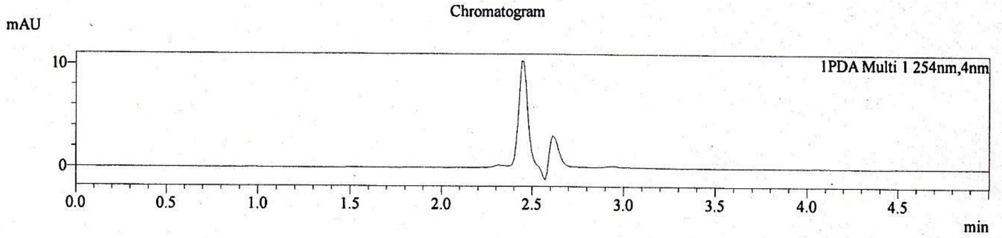

Peak Table

PDA Ch1 254nm

Peak#	Ret. Time	Area	Height
1	2.317	4340	676
2	2.448	45129	11136
3	2.616	24932	4173
4	2.939	3752	428
Total		78153	16414

<MS>

MS Chromatogram

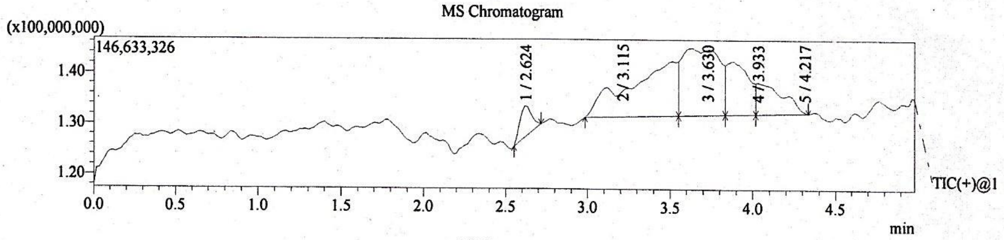

MS Spectrum

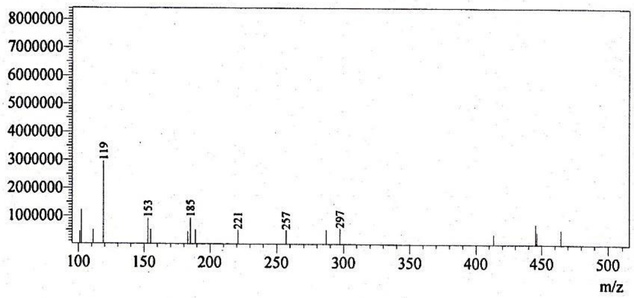

Figure S2 LCMS analysis of OR-II

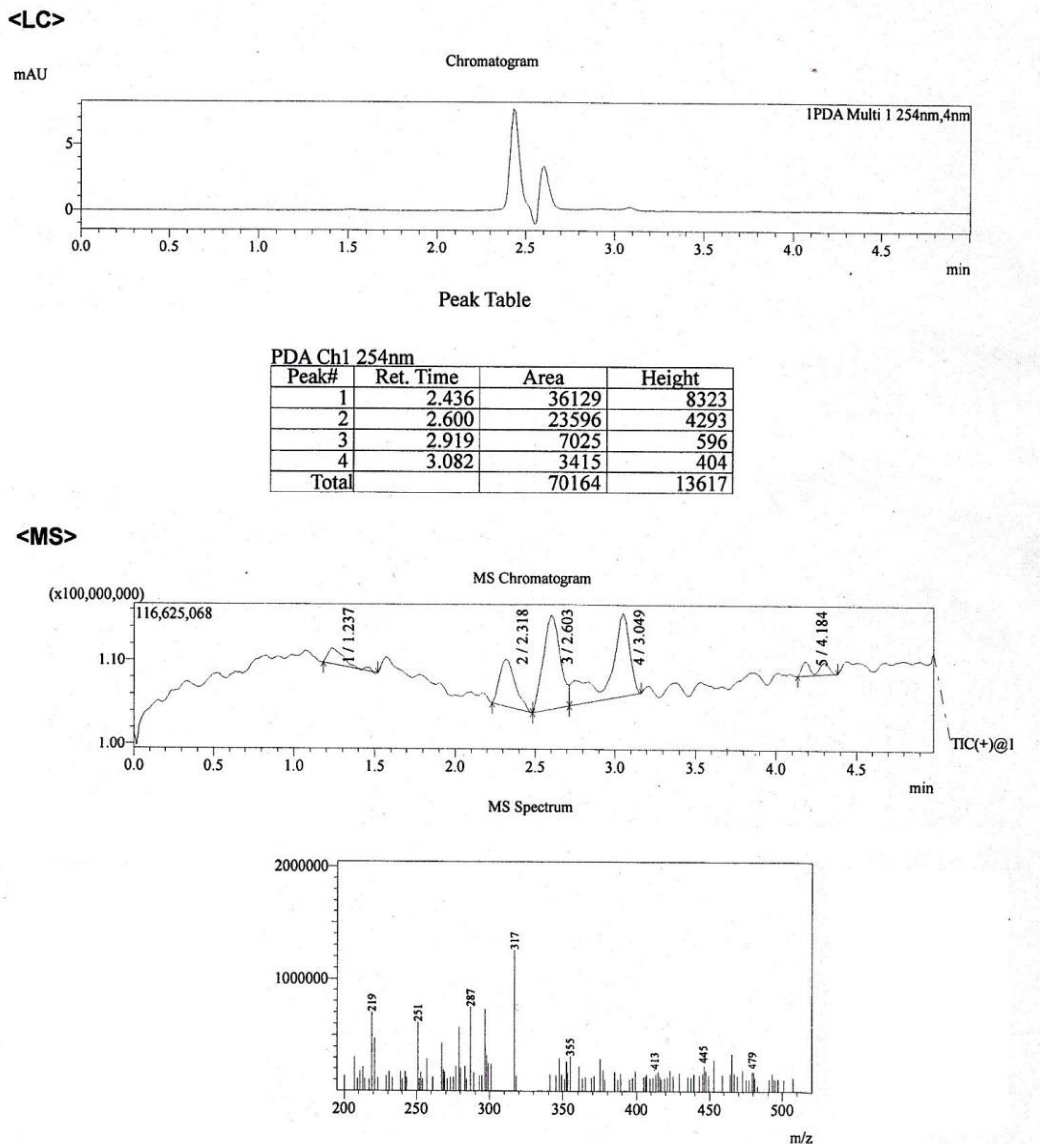

Peak Table

PDA Ch1 254nm

Peak#	Ret. Time	Area	Height
1	2.436	36129	8323
2	2.600	23596	4293
3	2.919	7025	596
4	3.082	3415	404
Total		70164	13617

Figure S3 LCMS analysis of MO

<LC>

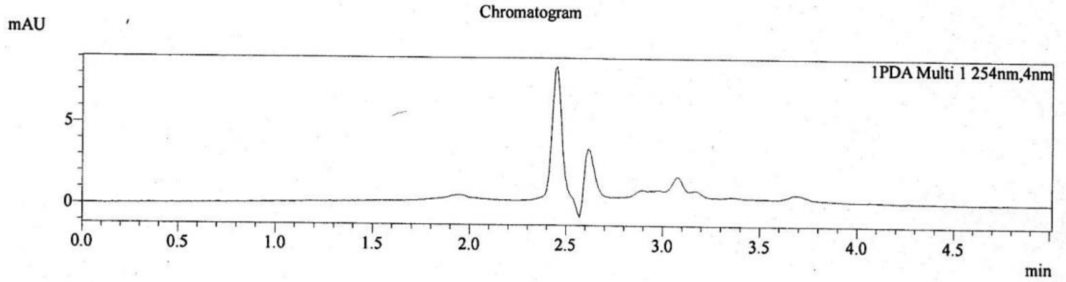

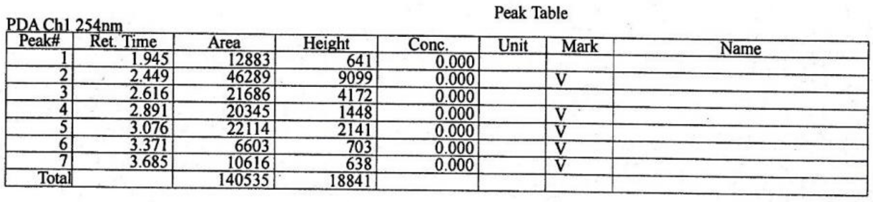
Peak Table

PDA Ch1 254nm

Peak#	Ret. Time	Area	Height	Conc.	Unit	Mark	Name
1	1.945	12883	641	0.000			
2	2.449	46289	9099	0.000		V	
3	2.616	21686	4172	0.000			
4	2.891	20345	1448	0.000		V	
5	3.076	22114	2141	0.000		V	
6	3.371	6603	703	0.000		V	
7	3.685	10616	638	0.000		V	
Total		140535	18841				

<MS>

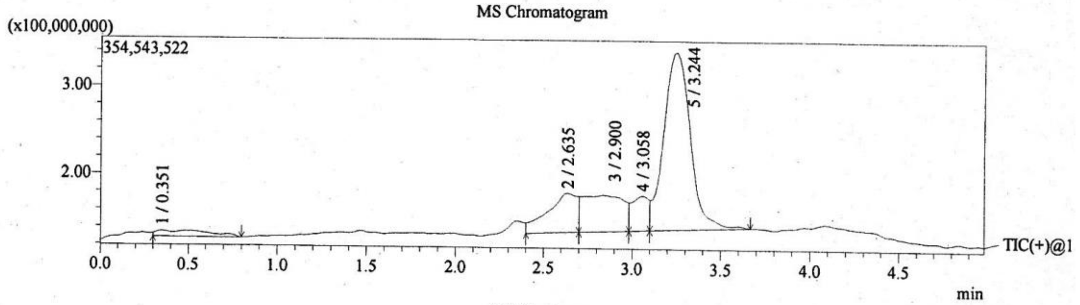

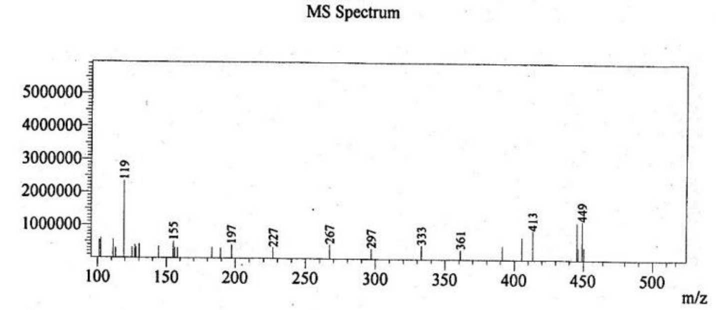

Figure S4 LCMS analysis of EBT

<LC>

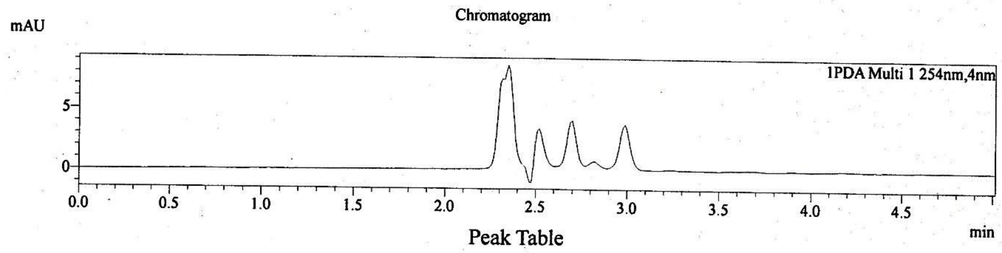

Peak Table

PDA Ch1 254nm

Peak#	Ret. Time	Area	Height
1	2.319	54868	7945
2	2.515	20346	4400
3	2.695	24665	4915
4	2.818	8665	1510
5	2.986	26336	4427
6	3.232	8627	555
7	3.661	2950	198
Total		146458	23949

<MS>

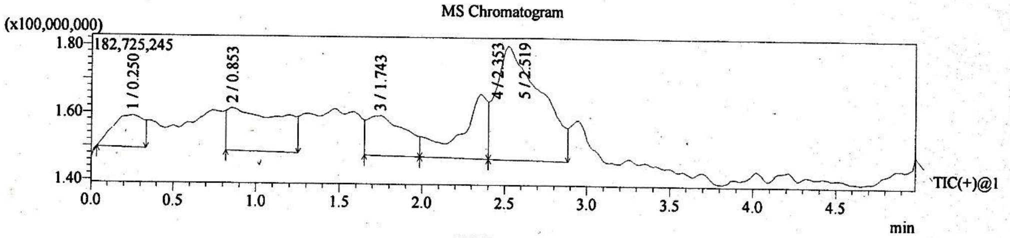

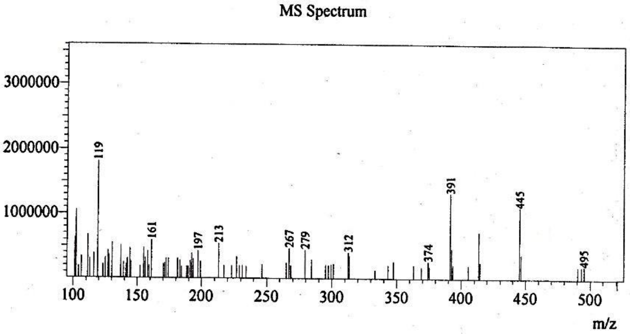

Figure S5 LCMS analysis of MD